

Graphene molecular junctions

Inauguraldissertation

zur
Erlangung der Würde eines Doktors der Philosophie
vorgelegt der
Philosophisch-Naturwissenschaftlichen Fakultät
der Universität Basel

von

Maria El Abbassi
aus Morocco

Basel, 2020

Genehmigt von der Philosophisch-Naturwissenschaftlichen Fakultät
auf Antrag von
Prof. Dr. Michel Calame
Prof. Dr. Colin Lambert

Basel, den 26. June 2018

Prof. Dr. Martin Spiess
Dekan

Contents

1	Introduction	1
I	Graphene electrode material	5
2	Experimental	7
2.1	Introduction	8
2.2	CVD growth and transfer	8
2.2.1	CVD growth	8
2.2.2	Transfer process	9
2.3	Raman measurements	10
2.3.1	Raman spectroscopy of graphene	10
2.3.2	Characterization of the as-transferred samples	11
2.4	Sample fabrication	12
2.5	Electrical characterization	13
2.6	Conclusion & outlook	15
G	Appendix	16
G.1	Sample layout	16
3	Electrical Breakdown of graphene: Substrate and environment effect	21
3.1	Introduction	22
3.2	Principle of the measurement	22
3.3	Substrate and Atmosphere effect on the EB process	24
3.4	Heat study	25
3.5	Effect of the thermal transport parameters on the estimated junction temperature and the activation energies	27
3.6	Conclusion	28
3.7	Outlook	29
II	Graphene tunnel junctions	33
4	Characterisation of the graphene tunnel junctions	35
4.1	Introduction	36
4.2	Raman spectroscopy	36
4.3	Estimation of the gap size by Simmons fitting	37
4.4	Simulation of the effect of the gate on tunneling junctions using the Simmons model	38

4.5	Gate dependence	39
4.6	Temperature dependence	40
4.7	Conclusion	41
4.8	Outlook: Measurements under a magnetic field	41
5	Graphene SiO_2 switches	45
5.1	Introduction	46
5.2	Electrical characterization of the switch	47
5.2.1	Electroformation of the Graphene- SiO_2 switch	48
5.2.2	Frequency dependence of the switching behavior	48
5.3	Timescales determination	50
5.3.1	Dead time	50
5.3.2	Endurance properties and set-reset transitions	53
5.3.3	Physical process	54
5.4	Conclusion	55
5.5	Outlook	55
III	Molecular junctions	63
6	Different strategies for anchoring molecules to graphene electrodes	65
6.1	Introduction	66
6.2	$\pi - \pi$ interaction	66
6.2.1	Covalent binding to the substrate combined with $\pi - \pi$ interaction to the electrode	67
6.2.2	Graphene Nanoribbons	68
6.3	Conclusion	69
7	Silanization as a robust way to contact molecules	73
7.1	Molecular structures and deposition	74
7.2	Measurements	75
7.3	DFT calculations	76
7.4	Cluster analysis	78
7.5	Discussion	79
7.6	Conclusion	80
G	Appendix	81
G.1	Theory and modeling	81
G.2	Clustering method and data analysis	85
8	Reproducible mechanically and electronically stable graphene molecular junctions	91
8.1	Junction geometry	92
8.2	Stability and intersample reproducibility at 20 K	93
8.3	Electronical stability of the junction at different temperatures	93
8.4	Discussion	96
8.5	Conclusion	96
F	Appendix	99

E1	Synthesis and characterization of the target molecule	99
E2	Transport through the junctions with different geometries	100
E3	Characterisation of an empty gap at different temperatures	102
E4	Fitting of the energies involved at different temperatures	102
E5	Electronic transport at different temperatures	105
E6	Fluctuations at different temperature	107
E7	Device 1: IV curves at different temperatures	108
9	Graphene Nanoribbons	113
9.1	Introduction	114
9.2	Synthesis and Transfer of the GNRs	114
9.3	Raman characterisation	115
9.4	Room temperature measurements	116
9.5	Low temperature measurements	116
9.6	Conclusion	118
	Conclusion	123
	Acknowledgement	125
	Curriculum Vitae	130
	Publication list	131



Introduction

Understanding charge and heat transport at the atomic and molecular level is important for both fundamental research and future electronic applications. Control of electron and phonon transport through a single molecule or atom will open the way to new physics and potentially electronic circuits operable at room temperature. Internal degrees of freedom of molecules (electronic, spin, vibrational, and rotational) were predicted to be ideal units to make quantum computers. For example, numerical simulations have shown that the molecular vibrations of the acetylene molecule are promising candidates for molecular vibrational qubits [1]. Further, a tunable molecular spin qubit with a coherence time in the millisecond regime has been measured experimentally [2].

To integrate molecular functions into devices, control of the molecule electrode interface is crucial, as this interaction heavily influences the molecular properties [3–5], and hence the device performance. However, achieving electronic and mechanical stability combined with reproducibility is not trivial and remains a bottleneck for the application of such devices. Electronic stability can for example be achieved by covalently binding the molecule to the electrodes. However, in the case of such strong electronic coupling, structural and electronic fluctuations in the system can lead to significant changes in the transport characteristics of the junction [6, 7], and hence unreliable device performance. $\pi - \pi$ stacking, on the other hand, has been predicted to be less sensitive to the electrode geometry [6]. However, due to the weak nature of the binding, this approach can result in unstable molecular junctions, in particular at room temperature. As device performances are critically determined by the molecular-electrode interaction [8,9], one of the key aspects in solving previously mentioned issues is the choice of electrode material, as it determines the possible binding processes [10]. Graphene, by its unique properties, is an ideal candidate to address these problems. First, due to its nature, different binding strategies (covalent, $\pi - \pi$ stacking, etc.) can be investigated

1 and exploited. Furthermore, it offers a flat and gateable platform with a high structural stability, even at room temperature [11–14].

The use of graphene as electrode material has been demonstrated experimentally [15–17], and relies on the formation of nanogaps using the electroburning process [15–17]. However, for the realization of reliable graphene-based junctions, several issues still need to be addressed. First, graphene-nanogaps, with low resistance, have been reported to exhibit signatures similar to those of molecules, with gate-dependent resonance features, such as Coulomb blockade [18, 19], quantum interference [12] and Fabry-Perrot resonances [20]. Secondly, to connect molecules to the graphene, $\pi - \pi$ stacking is believed to be the most suitable strategy [6] that offers advantages such as a high thermoelectric efficiency. However, due to the weak nature of this binding approach, molecules with planar anchors can slide on the surface of the graphene, resulting in mechanically unstable junctions [21]. Recently, Jia et al. [14] reported on mechanically stable junctions by employing a covalent binding of the molecule to the graphene electrodes. However, transport through strongly coupled molecules is expected to be heavily influenced by the electrode geometry, leading to a large variability in the electrical transport behavior [6]. Third, the chemical termination and crystallographic structure of the graphene nanogaps have not yet been characterized in detail. With an uncontrolled edge termination, achieving direct covalent binding between the molecules and the graphene remains challenging [22], as edge termination and shape can significantly affect the transport properties [23]. Fourth, the silicon dioxide of the substrate has been reported to yield feature-rich charge-transport characteristics, with the switching of the oxide being the main mechanism. Finally, junction-to-junction variability is high for the above-mentioned methods of anchoring to graphene [22, 24] and device statistics is poor.

In this dissertation, a detailed study of graphene-based molecular junctions is performed, describing the characterization of such devices in chronologic order, from the graphene growth and transfer to the contacting strategies of the molecules, and the charge transport measurements. The outline of this dissertation is as follows: In Chapter 2, the graphene sample preparation and characterization are presented. Chapter 3 gives details of the Electrical Breakdown (EB) process to produce nanogaps in the graphene junctions, of which a detailed characterization is presented in Chapter 4. Chapter 5, reports on the observation of a switching behavior in the SiO_2 within the gap region. Chapter 6 describes the different possibilities of anchoring molecules between the graphene electrodes with an example in Chapter 7 of a covalent bond to the oxide to contact the molecules and a vector-based analysis technique to understand the measurements. In Chapter 8, we report on the characterization of a mechanically and electronically stable molecular junction, combining covalent binding to the substrate with strong $\pi - \pi$ stacking. Chapter 9 presents the latest progress in contacting 5 atoms wide graphene nanoribbons. Finally, we conclude this manuscript with a brief highlight of the main results of this phd thesis.

Bibliography

- [1] Joseph M. Zadrozny, Jens Niklas, Oleg G. Poluektov, and Danna E. Freedman. Millisecond coherence time in a tunable molecular electronic spin qubit. *ACS central science*, 1(9):488–492, 2015.
- [2] K. Mishima, K. Tokumo, and K. Yamashita. Quantum computing using molecular electronic and vibrational states. *Chemical Physics*, 343(1):61–75, 2008.
- [3] Visions for a molecular future. *Nature nanotechnology*, 8(6):385–389, 2013.
- [4] Jochen Ulrich, Donna Esrail, William Pontius, Latha Venkataraman, David Millar, and Linda H. Doerrer. Variability of conductance in molecular junctions. *The journal of physical chemistry. B*, 110(6):2462–2466, 2006.
- [5] R. Frisenda and H. S. J. van der Zant. Transition from strong to weak electronic coupling in a single-molecule junction. *Phys. Rev. Lett.*, 117:126804, Sep 2016.
- [6] Hatef Sadeghi, Sara Sangtarash, and Colin Lambert. Robust molecular anchoring to graphene electrodes. *Nano Letters*, 17(8):4611–4618, 2017.
- [7] NJ Tao. Electron transport in molecular junctions. *Nature nanotechnology*, 1(3):173–181, 2006.
- [8] F. Prins, T. Hayashi, B. J. A. de van Vos Steenwijk, B. Gao, E. A. Osorio, K. Muraki, and H. S. J. van der Zant. Room-temperature stability of pt nanogaps formed by self-breaking. *Applied Physics Letters*, 94(12):123108, 2009.
- [9] Ferry Prins, Ahson J. Shaikh, Jan H. van Esch, Rienk Eelkema, and Herre S. J. van der Zant. Platinum-nanogaps for single-molecule electronics: room-temperature stability. *Physical chemistry chemical physics : PCCP*, 13(32):14297–14301, 2011.
- [10] D. Cahen and G. Hodes. Molecules and electronic materials. *Advanced Materials*, 14(11):789, 2002.
- [11] Ferry Prins, Amelia Barreiro, Justus W Ruitenberg, Johannes S Seldenthuis, Núria Aliaga-Alcalde, Lieven MK Vandersypen, and Herre SJ van der Zant. Room-temperature gating of molecular junctions using few-layer graphene nanogap electrodes. *Nano letters*, 11(11):4607–4611, 2011.
- [12] Hatef Sadeghi, Jan A Mol, Chit Siong Lau, G Andrew D Briggs, Jamie Warner, and Colin J Lambert. Conductance enlargement in picoscale electroburnt graphene nanojunctions. *Proceedings of the National Academy of Sciences*, 112(9):2658–2663, 2015.

- [13] Cornelia Nef, László Pósa, Péter Makk, Wangyang Fu, András Halbritter, Christian Schönenberger, and Michel Calame. High-yield fabrication of nm-size gaps in monolayer cvd graphene. *Nanoscale*, 6(13):7249–7254, 2014.
- [14] Chuancheng Jia, Agostino Migliore, Na Xin, Shaoyun Huang, Jinying Wang, Qi Yang, Shuopei Wang, Hongliang Chen, Duoming Wang, Boyong Feng, Zhirong Liu, Guangyu Zhang, Da-Hui Qu, He Tian, Mark A. Ratner, H. Q. Xu, Abraham Nitzan, and Xuefeng Guo. Covalently bonded single-molecule junctions with stable and reversible photoswitched conductivity. *Science*, 352(6292):1443–1445, 2016.
- [15] Ferry Prins, Amelia Barreiro, Justus W. Ruitenber, Johannes S. Seldenthuis, Núria Aliaga-Alcalde, Lieven M. K. Vandersypen, and Herre S. J. van der Zant. Room-temperature gating of molecular junctions using few-layer graphene nanogap electrodes. *Nano letters*, 11(11):4607–4611, 2011.
- [16] Jan A. Mol, Chit Siong Lau, Wilfred J. M. Lewis, Hatef Sadeghi, Cecile Roche, Arjen Cnossen, Jamie H. Warner, Colin J. Lambert, Harry L. Anderson, and G. Andrew D. Briggs. Graphene-porphyrin single-molecule transistors. *Nanoscale*, 7(31):13181–13185, 2015.
- [17] C. S. Lau, J. A. Mol, J. H. Warner, and G. A. D. Briggs. Nanoscale control of graphene electrodes. *Physical chemistry chemical physics : PCCP*, 16(38):20398–20401, 2014.
- [18] Chit Siong Lau, Hatef Sadeghi, Gregory Rogers, Sara Sangtarash, Panagiotis Dallas, Kyriakos Porfyrakis, Jamie Warner, Colin J Lambert, G Andrew D Briggs, and Jan A Mol. Redox-dependent Franck–Condon blockade and avalanche transport in a graphene–fullerene single-molecule transistor. *Nano letters*, 16(1):170–176, 2015.
- [19] Amelia Barreiro, Herre SJ van der Zant, and Lieven MK Vandersypen. Quantum dots at room temperature carved out from few-layer graphene. *Nano letters*, 12(12):6096–6100, 2012.
- [20] Pascal Gehring, Hatef Sadeghi, Sara Sangtarash, Chit Siong Lau, Junjie Liu, Arzhang Ardavan, Jamie H Warner, Colin J Lambert, G Andrew D Briggs, and Jan A Mol. Quantum interference in graphene nanoconstrictions. *Nano letters*, 16(7):4210–4216, 2016.
- [21] Suzhi Li, Qunyang Li, Robert W Carpick, Peter Gumbsch, Xin Z Liu, Xiangdong Ding, Jun Sun, and Ju Li. The evolving quality of frictional contact with graphene. *Nature*, 539(7630):541–545, 2016.
- [22] Qizhi Xu, Giovanni Scuri, Carly Mathewson, Philip Kim, Colin Nuckolls, and Delphine Bouilly. Single electron transistor with single aromatic ring molecule covalently connected to graphene nanogaps. *Nano letters*, 17(9):5335–5341, 2017.
- [23] Hatef Sadeghi, Sara Sangtarash, and Colin Lambert. Robust molecular anchoring to graphene electrodes. *Nano Letters*, 17(8):4611–4618, 2017.
- [24] Jan A Mol, Chit Siong Lau, Wilfred JM Lewis, Hatef Sadeghi, Cecile Roche, Arjen Cnossen, Jamie H Warner, Colin J Lambert, Harry L Anderson, and G Andrew D Briggs. Graphene-porphyrin single-molecule transistors. *Nanoscale*, 7(31):13181–13185, 2015.

Part I

Graphene electrode material

2 Experimental

To upscale the fabrication of graphene-based molecular junctions, large-scale production of graphene structures is necessary. For that purpose, we use Chemical Vapor Deposition (CVD) graphene combined with nano-lithography techniques to produce our samples. However, inhomogeneity of the graphene film and the presence of dopants influence the graphene electronic properties. Therefore, for achieving controllable and reproducible measurements, the quality of graphene films is primordial. In this Chapter, we investigate the quality and cleanliness of the CVD graphene after wet transfer and e-beam fabrication using Raman characterization and electrical measurements.

2.1. Introduction

Graphene, a covalent planar carbon-based material, is a very promising material for achieving controlled coupling to molecules [1]. However, the 2-dimensional nature of this material implies the electronic properties to be very sensitive to several parameters like the crystalline structure, the edge properties or the doping level [2, 3].

Chemical vapor deposition (CVD) is the most used technique to produce large scale graphene. However, the production cycle of graphene has several critical parameters such as the growth conditions (pressure, temperature and carbon flux), the transfer techniques and the substrate preparation procedure. Indeed, different growth or transfer parameters can lead to a significant difference in the intrinsic properties of the graphene film [4].

For this purpose, we performed a comparative study between CVD graphene with large crystals (single domain, SD) and uniformly grown graphene films (multi domain, MD) to systematically assess their quality. To study the local variations in the graphene film, we rely on large-area Raman mapping, allowing us to determine the quality of the graphene films with regard to doping, number of layers and strain. Finally, the electronic properties of the graphene are assessed after device fabrication using charge transport measurements.

2.2. CVD growth and transfer

2.2.1. CVD growth

CVD graphene was grown on a polycrystalline copper foil using a low pressure CVD technique in a hot wall CVD reactor at a temperature of 1000°C . The growth process consists of three main steps: annealing of the copper foil, the growth itself, and finally cooling down of the system.

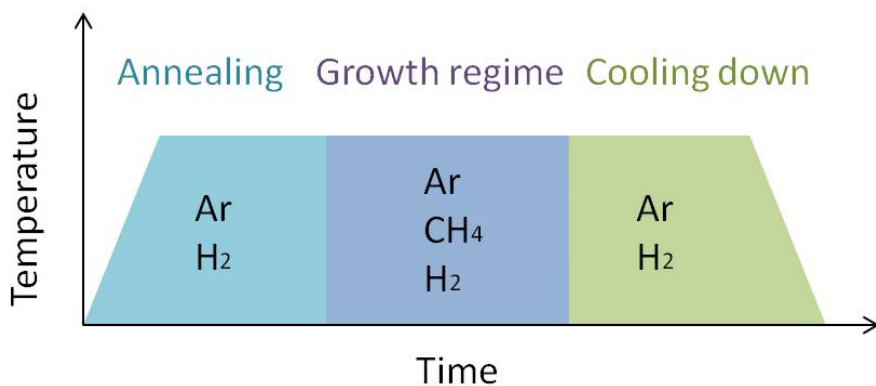


Figure 2.1: Schematic of the different steps of the CVD growth. The process consists of three main regimes: annealing of the Cu foil, the growth, and the cooling down of the system.

Prior to the film growth, the copper foil undergoes a high temperature pre-treatment and annealing at 1000°C under an argon (Ar) and hydrogen (H_2) gas flow (Fig. 2.1). In this step, the pressure of H_2 and annealing time are important parameters that strongly influence

the quality of the graphene during growth. Close to the Cu melting point, the Cu surface is cleaned by reducing the oxide at the surface. Moreover, the roughness of the Cu surface is believed to be changed by the evaporation of few atoms of Cu. It is also now commonly accepted that active H radicals will bind to the Cu surface to be later released during the growth regime and act as a catalyst for the reaction. For these reasons, the growth rate depends strongly on the annealing time and the presence of H_2 during this step [5–7].

To initiate the growth, methane (CH_4) is introduced into the CVD chamber next to the H_2 and Ar flow. During the growth phase, the methane molecules are dissociated at the surface of the copper foil by interacting with the H at the surface. The growth of the graphene then starts from the nucleation centers of which the density strongly depends on the flow of CH_4 . This same flow of methane, together with hydrogen flow, also affects the edge structure, passivation and morphology of the grown films [5–7].

In our case, we focused on the effect of the methane flow during growth and could identify two main regimes. The first one consists of a low carbon supply to form single graphene grains at reduced nucleation density [8]. For this process, the methane flow rate was kept at 0.04 sccm. The growth of SD graphene was achieved by using a low carbon flow rate and stopping the CVD growth prior to the formation of a uniform single graphene layer, which typically occurs after 6 hours. The second regime consists of the growth of MD graphene samples with a uniform coverage of single layer graphene. This was obtained by using a higher carbon flow rate. Furthermore, the growth process was stopped after the coalescence of individual graphene domains (15 minutes).

Finally, the quality of the graphene film is also affected by the cooldown process. Depending on the cooling rate and/or the presence of methane, different reactions can occur. Many studies have shown that the graphene grain size, density and morphology are affected by the cooldown parameters [9, 10]. For instance, the presence of H_2 during the cooldown can etch weakly bound C-atoms which may be present on the copper surface. In our case, we systematically cooled down to room temperature under argon and hydrogen atmosphere.

2.2.2. Transfer process

After growth, the film is transferred onto a SiO_2/Si substrates (with thicknesses of 285nm and $300\mu m$, respectively) using a wet etching technique [11]. The transfer process consists of 5 main steps:

- First, the top side of the copper foil is covered with 400 nm thick 50K PMMA (4000 rpm, 40 seconds) and baked at $180^\circ C$ for 3 minutes.
- The graphene layer on the back side of the copper foil is etched using an oxygen plasma (30W, 250 mbar, 16 sccm Ar, 8 sccm O_2) for 1 minute to facilitate the copper etching.
- The PMMA/graphene/copper foil is transferred to a solution of ammonium persulfate (0.1 M) to etch the copper overnight.
- The PMMA/graphene is rinsed in DI water and transferred onto the substrate.
- The PMMA is then dissolved in $50^\circ C$ acetone for 10 minutes and rinsed in iso-propyl alcohol (IPA) and blown dry with N_2 gas.

Optical images of SD and MD graphene transferred on SiO_2/Si substrate are shown in Fig. 2.2.a), b). Figure 2.2.c) shows a high density of individual graphene grains for a growth

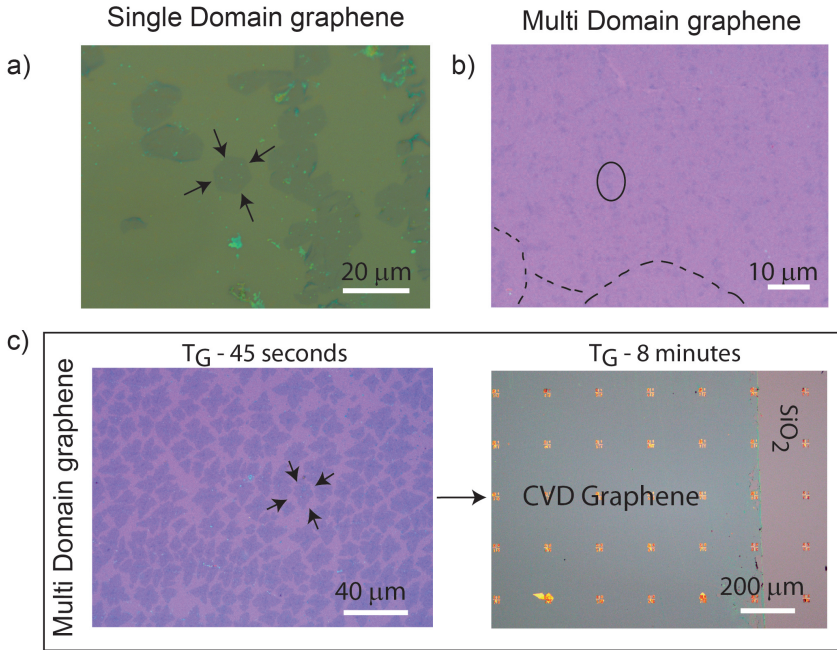


Figure 2.2: Optical image of graphene after transfer (a) Optical image of SD graphene on SiO_2 . An individual graphene grain is indicated using black arrows. (b) Optical image of MD graphene on SiO_2 substrate. A bi-layer graphene flake is marked by circle and wrinkles are marked by dotted lines. (c) Optical images of MD graphene transferred on SiO_2 substrate at growth time T_G of 45 seconds and 8 minutes.

time of $T_G \approx 45$ s, and for $T_G \approx 8$ min, where the SD graphene grains start to coalesce, thus forming a uniform sheet of MD graphene.

2.3. Raman measurements

2.3.1. Raman spectroscopy of graphene

Raman spectroscopy is one the most effective non-invasive tool to characterize doping, strain, edges, number of layers, stacking of layers and defects in graphene [12]. The G and 2D peaks are the two prominent Raman peaks which can be observed around 1585 cm^{-1} and 2674 cm^{-1} for exfoliated graphene flakes on Si/ SiO_2 substrate [12, 13]. The G and 2D peak positions and their full-width-half maximum (FWHM) are related to doping and strain. Defects in graphene can be characterized by studying the shape and amplitude of the D peak within the graphene flake. This peak, which occurs around 1345 cm^{-1} , is the result of defect assisted inter-valley scattering processes [14–16]. Disorder in graphene (bond disorder, defects) can also be assessed from the intensity ratio of the D and G peaks [17].

Studying regional variations in the graphene film is of utmost importance to elucidate the true quality of the graphene film. Hence, we rely on large-area Raman mapping instead of single Raman spectra from different regions for characterizing parameters such as doping,

the thickness of the graphene film and strain [17, 18].

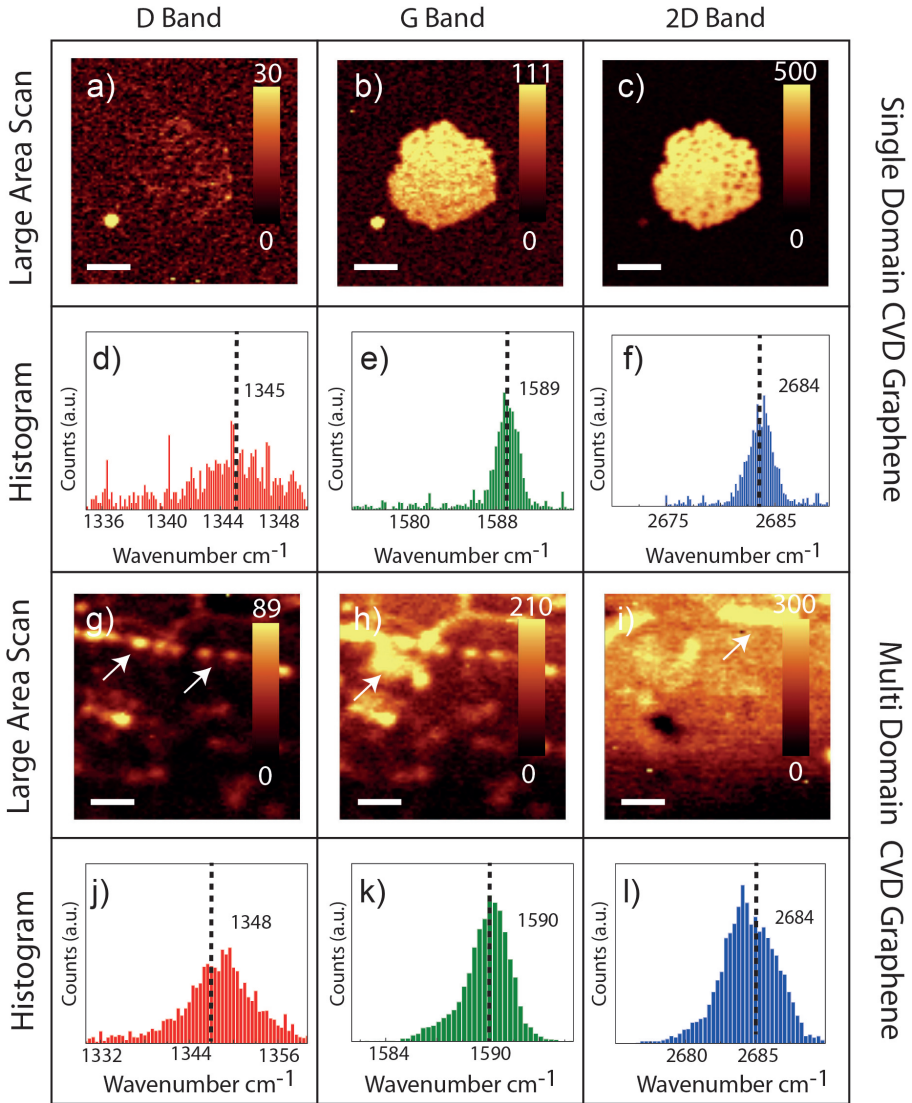


Figure 2.3: Raman characterization of the graphene samples after transfer Large-area Raman scans of D, G and 2D bands (a–c, g–i) and peak position histograms of SD (d–f) and MD (j–l) graphene. The average peak positions are marked with black dotted lines for D, G and 2D bands. Features in the large-area scans are marked using white arrows. Scale bars: 4 μm (SD) and 42 μm (MD).

2.3.2. Characterization of the as-transferred samples

We performed large-area confocal Raman spectroscopy ($\lambda_{\text{laser}} \sim 532 \text{ nm}$, $P_{\text{laser}} \sim 2 \text{ mW}$) of SD and MD graphene right after transfer to determine the quality of CVD graphene. In

Fig. 2.3(a),c) and (g)–(i) we show large-area Raman intensity maps for the D, G and 2D bands and their corresponding peak position histograms (Fig. 2.3.(d)–(f), (j)–(l)) for SD and MD graphene samples, respectively). We observe nearly hexagonal graphene grains for SD graphene growth conditions (see Fig. 2.2 (a)). The G peak position can be used to estimate the charge carrier concentration in the graphene sheet, which can be tuned by electrically modulating graphene's Fermi level by applying a voltage on the back-gate. It has been observed that the G peak position shifts to larger wavenumbers for both electron and hole doping [19,20]. The average peak position of the G and 2D bands for the SD sample are 1589 cm^{-1} and 2684 cm^{-1} , respectively. They are up-shifted by 4 cm^{-1} and 10 cm^{-1} compared to the values observed for freshly exfoliated graphene samples on Si/SiO_2 substrate. In Fig. 2.3(g)–(i) and (j)–(l) we show large-area scans and peak position histograms for MD graphene. The average G and the 2D peak positions are located at 1590 cm^{-1} and 2684 cm^{-1} [18]. When compared to SD graphene, we observe an upshift of 1 cm^{-1} for the G band, which points towards a slightly higher p-doping for the MD sample. We note that the type of doping can be verified by the direction of the Dirac peak shift in a gate characteristic, as will be shown later in this chapter (see Fig. 2.5 (b), where $V_{\text{Diracpeak}} > 0\text{ V}$ points towards p-doping).

We also observe more features in the D and G band large-area scans of MD graphene. The bright lines in the D and G band scans can result from wrinkles and folds in the copper foil, which may occur during the graphene transfer. Moreover, a similar upshift in wavenumbers is observed in both CVD graphene types (as compared to a freshly exfoliated graphene sample) is of similar magnitude, suggesting that it originates from the transfer process, rather than from the growth, as the growth conditions for SD and MD graphene types are very different. The observed upshift of the G and 2D peak position is attributed to the high p-doping induced by the exposure to water and PMMA leftovers during the transfer process, which is absent in a freshly exfoliated graphene flake. It is known that high p-doping (n-doping) of graphene can result in stiffening (softening) of the G peak phonons and cause an upshift (downshift) in wavenumbers. Moreover, the polymeric residues and wrinkles from the transfer result in a pronounced D peak.

2.4. Sample fabrication

The fabrication process consists of two main steps as represented in Fig. 2.4:

- **Graphene patterning:** E-beam lithography is performed on the graphene covered with ZEP resist (400nm). After development, reactive-ion etching (RIE) of graphene is performed.
- **Metallic contacts evaporation:** Contacts are defined using e-beam lithography on the graphene structures, followed by evaporation of 5nm of Ti that acts as an adhesion layer and 45 nm of Au.

To remove part of the contamination due to the polymer assisted transfer and fabrication, annealing of the devices under Ar or N_2 gas can be performed. In our case, this is not critical due to the current annealing that occurs during the breaking process.

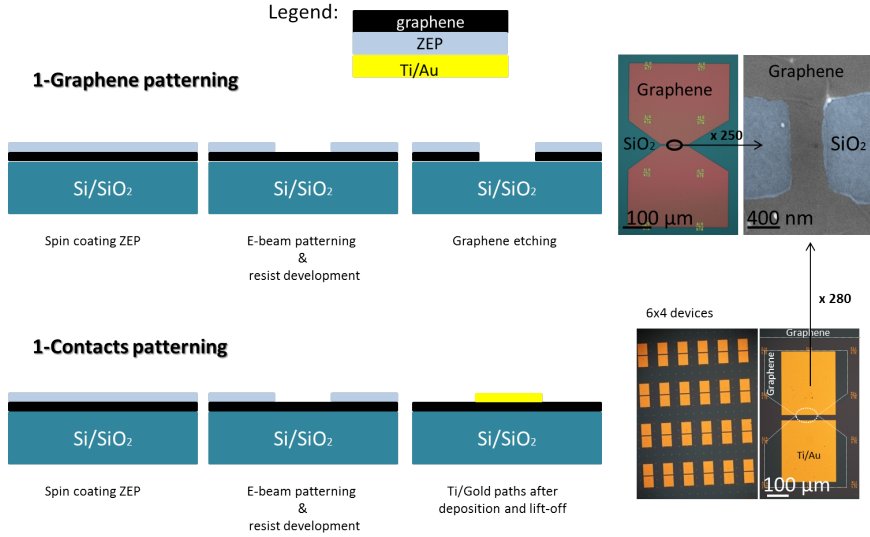


Figure 2.4: Schematic of the fabrication steps. The first step consists in patterning the graphene constrictions and, followed by metal deposition of Au contacts.

2.5. Electrical characterization

In order to compare the electrical transport characteristics, the sheet resistance R is shown in Fig. 2.5 as a function of the charge carrier density n_e for both SD and MD graphene. The SD sample was fabricated on a single graphene grain, while no pre-selection of the graphene region was made in case of MD graphene. After fabrication, the samples underwent thermal annealing in forming gas (Ar/H₂) at 300 °C for 3 hours to reduce the amount of polymer residues on the graphene film [19]. After thermal annealing, electrical characterization was performed in vacuum condition (10⁻⁴ mbar) in order to avoid p-doping due to exposure to ambient conditions.

The transport characteristics of both SD and MD graphene show only little p-doping, with the Dirac peak close to V_g equal to 0 V. We also observe an asymmetric R vs n_e characteristic for both the SD and MD devices, which is attributed to doping of the metal-graphene interface at the source and drain contacts [20]. The mobility μ_{FET} of SD and MD graphene differ significantly, from $\mu_{FET} = 6000 \text{ cm}^2/\text{Vs}$ for SD to $\mu_{FET} = 1200 \text{ cm}^2/\text{Vs}$ for MD, i.e. a five times higher mobility in SD graphene.

While SD graphene devices were fabricated on a single graphene domain, the MD devices consist of several graphene domains which can lead to a reduction in μ_{FET} due to scattering at the grain boundaries. Keeping this in mind, the device characteristics of MD graphene may be further improved by preselecting the region of MD graphene to be used for device fabrication, such that the sample is fabricated within a single grain of MD graphene. Higher field effect mobility also results from lower charge scattering which is in line with the smaller sheet resistance R observed in SD graphene. As a comparison, ultraclean, single crystalline graphene (exfoliated, and encapsulated in hexagonal boron nitride (hBN)) exhibits μ_{FET} of up to $10 \times 10^6 \text{ cm}^2/\text{Vs}$, observed in micron scaled samples [21, 22].

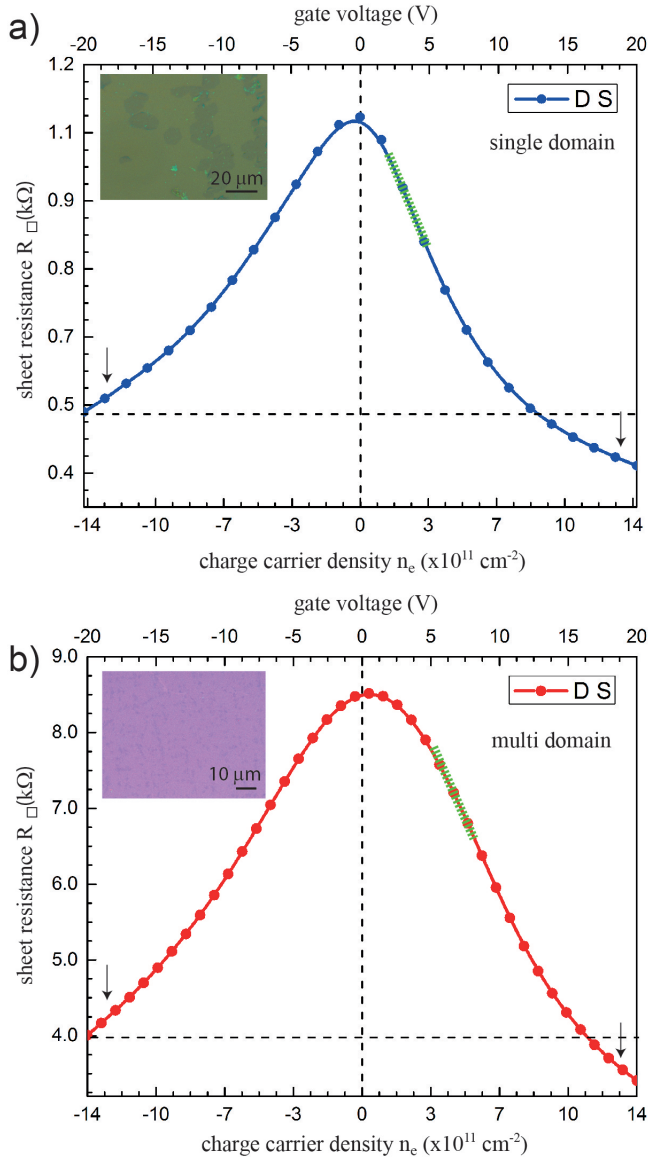


Figure 2.5: Electrical characterization Source–drain (DS) measurement of the sheet resistance as a function of the charge carrier density n_e for both SD (a) and MD (b) graphene samples, using a bias voltage V_{DS} of 10 mV. Inset: Optical image of the SD and MD graphene on SiO $_2$. The field-effect mobility was calculated using the slope of the conductance curve determined by the green stripes. The dotted lines and arrows highlight the asymmetry in the field-effect characteristics. Source–drain measurement of the sheet resistance R as a function of the charge carrier density n_e for both SD (a) and MD (b) graphene samples, using a bias voltage of V_{DS} of 10 mV. Inset: Optical image of the SD and MD graphene on SiO $_2$. The field-effect mobility was calculated using the slope of the conductance curve determined by the green stripes. The dotted lines and arrows highlight the asymmetry in the field-effect characteristics.

2.6. Conclusion & outlook

By performing a systematic Raman and electrical characterization of the transferred SD and MD graphene, we find a similar upshift of the G and 2D peak positions for both graphene morphologies when compared to polymer-free freshly exfoliated graphene on SiO₂/Si substrate. Although CVD graphene films can be compressively strained due to the transfer process, the observed shift in our case can be predominantly attributed to p-doping in the presence of water and contaminants. Electrical transport measurements performed after thermal annealing in low vacuum show a Dirac peak close to 0 V, suggesting the absence of p-doping. The field-effect mobility of SD graphene is found to be about five times higher than in MD graphene. The higher sheet resistance values measured in MD graphene reveal an increased charge scattering due to grain boundaries, wrinkles, folds and crystal defects, even though the Raman mapping of SD and MD graphene show similar characteristics.

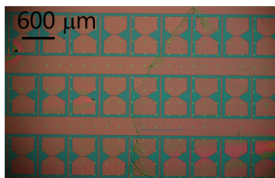
Part 1.3 and 1.5 of this chapter and Figures 1.2, 1.3 and 1.5 are extracted from our paper published in *physica status solidi (RRL)*, 10(11), 807-811, 2016. The authors are Kishan Thodkar, Maria El Abbassi, Felix Lüönd, Frédéric Overney, Christian Schoenenberger, Blaise Jeanneret, and Michel Calame. K.T did the graphene growth and fabrication. K.T. and M.E. participated to the electrical and Raman characterization. All the authors participated in the discussion and the writing of the manuscript.

G. Appendix

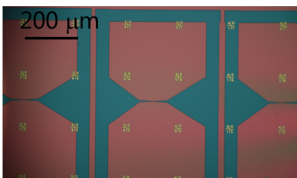
G.1. Sample layout

2

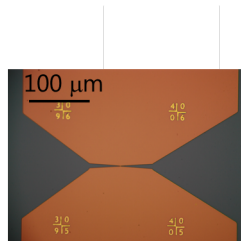
1-Graphene patterning



9x3 devices

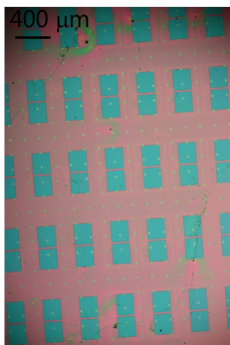


1x3 devices

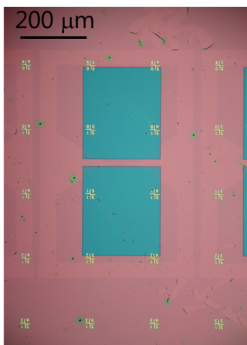


1x1 device

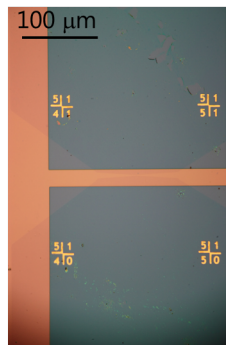
2-Contact patterning



6x5 devices



1x1 devices



1x1 device

Figure 2.6: Optical images of the sample at different fabrication steps.

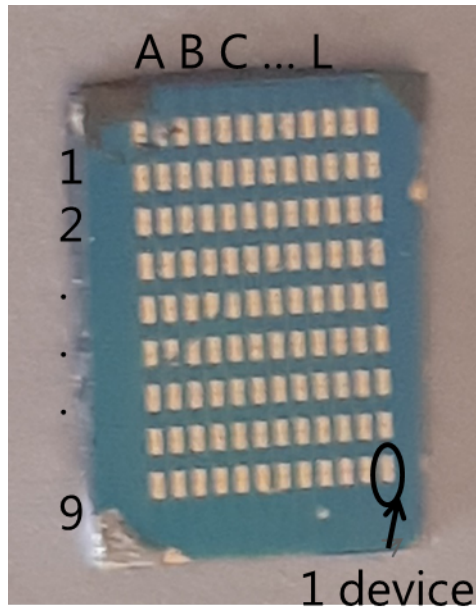


Figure 2.7: A final sample with 12 columns of devices with 9 devices each. The sample is 0.8 cm wide and 1.4 cm long.

2

Bibliography

- [1] Emanuel Lörtscher. Wiring molecules into circuits. *Nature nanotechnology*, 8(6):381–384, 2013.
- [2] Sk. Fahad Chowdhury, Sushant Sonde, Somayyeh Rahimi, Li Tao, Sanjay Banerjee, and Deji Akinwande. Improvement of graphene field-effect transistors by hexamethyldisilazane surface treatment. *Applied Physics Letters*, 105(3):033117, 2014.
- [3] Wangyang Fu, Cornelia Nef, Oren Knopfmacher, Alexey Tarasov, Markus Weiss, Michel Calame, and Christian Schönenberger. Graphene transistors are insensitive to pH changes in solution. *Nano letters*, 11(9):3597–3600, 2011.
- [4] Sreekar Bhaviripudi, Xiaoting Jia, Mildred S. Dresselhaus, and Jing Kong. Role of kinetic factors in chemical vapor deposition synthesis of uniform large area graphene using copper catalyst. *Nano letters*, 10(10):4128–4133, 2010.
- [5] Yan Jin, Baoshan Hu, Zidong Wei, Zhengtang Luo, Dapeng Wei, Yi Xi, Ye Zhang, and Yunling Liu. Roles of h₂ in annealing and growth times of graphene cvd synthesis over copper foil. *J. Mater. Chem. A*, 2(38):16208–16216, 2014.
- [6] Shanshan Chen, Hengxing Ji, Harry Chou, Qiongyu Li, Hongyang Li, Ji Won Suk, Richard Piner, Lei Liao, Weiwei Cai, and Rodney S. Ruoff. Millimeter-size single-crystal graphene by suppressing evaporative loss of cu during low pressure chemical vapor deposition. *Advanced materials (Deerfield Beach, Fla.)*, 25(14):2062–2065, 2013.
- [7] Ivan Vlasiouk, Murari Regmi, Pasquale Fulvio, Sheng Dai, Panos Datskos, Gyula Eres, and Sergei Smirnov. Role of hydrogen in chemical vapor deposition growth of large single-crystal graphene. *ACS nano*, 5(7):6069–6076, 2011.
- [8] Xuesong Li, Carl W. Magnuson, Archana Venugopal, Rudolf M. Tromp, James B. Hannon, Eric M. Vogel, Luigi Colombo, and Rodney S. Ruoff. Large-area graphene single crystals grown by low-pressure chemical vapor deposition of methane on copper. *Journal of the American Chemical Society*, 133(9):2816–2819, 2011.
- [9] Dong Soo Choi, Keun Soo Kim, Hyeongkeun Kim, Yena Kim, TaeYoung Kim, Se-hyun Rhy, Cheol-Min Yang, Dae Ho Yoon, and Woo Seok Yang. Effect of cooling condition on chemical vapor deposition synthesis of graphene on copper catalyst. *ACS applied materials & interfaces*, 6(22):19574–19578, 2014.
- [10] Jihyung Seo, Junghyun Lee, A-Rang Jang, Yunseong Choi, Ungsoo Kim, Hyeon Suk Shin, and Hyesung Park. Study of cooling rate on the growth of graphene via chemical vapor deposition. *Chemistry of Materials*, 29(10):4202–4208, 2017.

- [11] Ji Won Suk, Alexander Kitt, Carl W. Magnuson, Yufeng Hao, Samir Ahmed, Jinho An, Anna K. Swan, Bennett B. Goldberg, and Rodney S. Ruoff. Transfer of cvd-grown monolayer graphene onto arbitrary substrates. *ACS nano*, 5(9):6916–6924, 2011.
- [12] A. C. Ferrari, J. C. Meyer, V. Scardaci, C. Casiraghi, M. Lazzeri, F. Mauri, S. Piscanec, D. Jiang, K. S. Novoselov, S. Roth, and A. K. Geim. Raman spectrum of graphene and graphene layers. *Physical review letters*, 97(18):187401, 2006.
- [13] A. Gupta, G. Chen, P. Joshi, S. Tadigadapa, and P. C. Eklund. Raman scattering from high-frequency phonons in supported n-graphene layer films. *Nano letters*, 6(12):2667–2673, 2006.
- [14] A. Das, S. Pisana, B. Chakraborty, S. Piscanec, S. K. Saha, U. V. Waghmare, K. S. Novoselov, H. R. Krishnamurthy, A. K. Geim, A. C. Ferrari, and A. K. Sood. Monitoring dopants by raman scattering in an electrochemically top-gated graphene transistor. *Nature nanotechnology*, 3(4):210–215, 2008.
- [15] Andrea C. Ferrari and Denis M. Basko. Raman spectroscopy as a versatile tool for studying the properties of graphene. *Nature nanotechnology*, 8(4):235–246, 2013.
- [16] Simone Pisana, Michele Lazzeri, Cinzia Casiraghi, Kostya S. Novoselov, A. K. Geim, Andrea C. Ferrari, and Francesco Mauri. Breakdown of the adiabatic born-oppenheimer approximation in graphene. *Nature materials*, 6(3):198–201, 2007.
- [17] L. G. Cançado, A. Jorio, E. H. Martins Ferreira, F. Stavale, C. A. Achete, R. B. Capaz, M. V. O. Moutinho, A. Lombardo, T. S. Kulmala, and A. C. Ferrari. Quantifying defects in graphene via raman spectroscopy at different excitation energies. *Nano letters*, 11(8):3190–3196, 2011.
- [18] C. Neumann, S. Reichardt, P. Venezuela, M. Drömler, L. Banszerus, M. Schmitz, K. Watanabe, T. Taniguchi, F. Mauri, B. Beschoten, S. V. Rotkin, and C. Stampfer. Raman spectroscopy as probe of nanometre-scale strain variations in graphene.
- [19] A. Pirkle, J. Chan, A. Venugopal, D. Hinojos, C. W. Magnuson, S. McDonnell, L. Colombo, E. M. Vogel, R. S. Ruoff, and R. M. Wallace. The effect of chemical residues on the physical and electrical properties of chemical vapor deposited graphene transferred to sio₂. *Applied Physics Letters*, 99(12):122108, 2011.
- [20] B. Huard, N. Stander, J. A. Sulpizio, and D. Goldhaber-Gordon. Evidence of the role of contacts on the observed electron-hole asymmetry in graphene. *Physical Review B*, 78(12), 2008.
- [21] Luca Banszerus, Michael Schmitz, Stephan Engels, Jan Dauber, Martin Oellers, Federica Haupt, Kenji Watanabe, Takashi Taniguchi, Bernd Beschoten, and Christoph Stampfer. Ultrahigh-mobility graphene devices from chemical vapor deposition on reusable copper. *Science advances*, 1(6):e1500222, 2015.
- [22] L. Wang, I. Meric, P. Y. Huang, Q. Gao, Y. Gao, H. Tran, T. Taniguchi, K. Watanabe, L. M. Campos, D. A. Muller, J. Guo, P. Kim, J. Hone, K. L. Shepard, and C. R. Dean. One-dimensional electrical contact to a two-dimensional material. *Science (New York, N.Y.)*, 342(6158):614–617, 2013.

Electrical Breakdown of graphene: Substrate and environment effect

In this chapter, we report on the characterization of the Electrical Breakdown (EB) process for the formation of tunneling nanogaps in single-layer graphene. In particular, we investigate the role of oxygen in the breakdown process by varying the environmental conditions (vacuum and ambient conditions). We show that the density of oxygen molecules in the chamber is a crucial parameter that defines the physical breakdown process: at low density, the graphene lattice is sublimating, whereas at high density the process involved is oxidation, independent of the substrate material. To estimate the activation energies of the two processes, we use a scheme which consists of applying voltage pulses across the junction during the breaking. By systematically varying the voltage pulse length, and estimating the junction temperature from a 1D thermal model, we extract activation energies which are consistent with the sublimation of graphene in high vacuum and the electroburning process in air.

3.1. Introduction

The use of graphene as electrode material for molecular electronics has been demonstrated experimentally [1–3], and relies on the formation of nanogaps using the electroburning process [1, 2, 4]. This process allows the production of sub-5nm gaps with a junction formation yield of > 95% [5]. However, to achieve control of the edge termination or crystallographic structure, understanding the details of the EB process is critical. Here, in order to identify the key parameters in the EB process, we study the influence of the environmental conditions, and in particular, the role of the oxygen content. We find that at ambient conditions the EB is caused by the conventional electroburning process, while in high vacuum, sublimation takes place. By using a simple heat-transport model, we extract estimates for the relevant activation energies, which are consistent with the proposed electroburning and sublimation processes. To exclude the substrate as a source of oxygen, we also performed a comparative study of the EB process on SiO₂ and Si₃N₄ substrates. In contrast to previous reports [6], we find that the presence of oxygen in the substrate does not play a role in the EB process.

3.2. Principle of the measurement

Nanogaps were formed using EB of the graphene bridges. The EB process is performed by applying high voltage pulses with increasing amplitude to the device. The current response is measured for each pulse (Fig. 3.1b), from which the high bias resistance is calculated (R_{high}). At each EB step the pulse height, V_{high} is increased by 5 mV, and the process is stopped after the first pulse, when R_{high} exceeds 500 k Ω . This corresponds often to a jump in the resistance. The influence of the pulse length on the EB process is systematically studied using 5 μ s to 5 s pulses. Between subsequent pulses an offset voltage of 100 mV is applied to determine the low bias resistance, R_{low} . The measurements were performed both at ambient conditions (in air) and in high vacuum (down to $p = 10^{-7}$ mbar).

Fig. 3.1a shows the evolution of R_{high} and R_{low} for a typical EB process in vacuum with a pulse length of 10 ms. Due to Joule heating [7], R_{high} increases as the pulse height is increased, whereas R_{low} remains almost constant until the breakdown occurs at V_{bd} . Changes of the low bias resistance can occur because of annealing effects. Different polymer residues from the transfer and lithography resist can lead to a change of the graphene resistance due to increased scattering or doping effects. The high current during EB induces cleaning of the devices and hence changes of the resistance [8].

Fig. 3.1c shows the I-V curves of a graphene bridge before and after EB. Before EB, the current-voltage characteristic of the graphene bridge is linear with a resistance of 12.5 k Ω . After EB, the device shows S-shaped I-V curves, characteristic for tunneling. Assuming a rectangular barrier, we can fit the curves to the Simmons model [9] and obtain an estimate of the gap size of about 1.5 nm for this particular device. The low bias resistance of the graphene nanogaps after EB provides a first indication about the size and the cleanliness of the gap. It has been suggested that an ideal device should have a resistance of a few G Ω [10]. Very wide gaps will exhibit larger resistance values resulting often in unresolvable tunnel currents. Lower resistances, in the M Ω regime, can be explained by the presence of carbon islands or residues bridging the gap. To test the latter, we have systematically performed

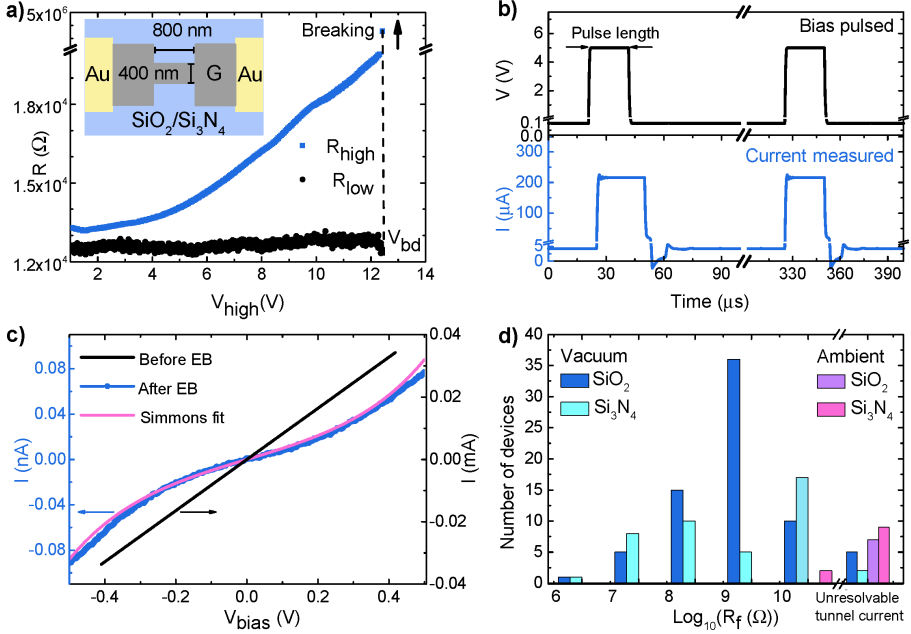


Figure 3.1: Description of the EB process: a) Resistance at high bias R_{high} (in blue) and low bias R_{low} (in black) during EB of a device in vacuum with pulse lengths of 10 ms. An increase of resistance due to Joule heating is observed at high bias. At breakdown voltage V_{bd} , a jump of resistance is observed, as a sign of the gap formation. The inset is a schematic of the device. b) The applied voltage pulse is shown with the simultaneously recorded current for a pulse length of 25 μs . c) Current-voltage characteristic of a device before and after EB. Before EB, the I-V curve is linear and the current is in the mA range (right axis, black). After EB, we measure non linear I-V curves with currents in the nA range, due to the presence of a gap (left axis, blue). The pink curve represents a Simmons fit of the tunneling curve. d) Distribution of the low bias resistance R_f at zero gate voltage of the junctions after EB in vacuum and at ambient conditions for both substrates. For resistances larger than $10^{11} \Omega$, no tunnel current could be resolved.

gate dependent measurements of the tunneling behavior at room temperature. A few devices were also characterized at low temperature (see chapter 3). The majority of the devices, typically more than 70%, do not show any gate dependence at room temperature. Fig. 3.1d shows the distribution of the low bias resistances after EB for SiO₂ and Si₃N₄ substrates both in vacuum and in air at zero gate voltage.

In our measurements the EB always happens immediately: even if we apply ultrashort pulses (down to 5 μs width), we cannot detect any precursor of the breakdown before the last, breaking pulse. In agreement with our previous report [5] on SiO₂ substrates, here we observed that for both substrates a measurable tunnel current corresponding to a few nm gap size is achieved with a yield of 95% if the EB is performed in vacuum. In air, however there is a much higher chance to achieve unmeasurably large resistance values, and thus a large and uncontrolled gap size. We note, that in Refs [[1, 4, 10, 11]] gradual breakdown, and smaller gap sizes are achieved in air using real time feedback controlled EB protocol with $>200\mu\text{s}$ response time, and different sample geometries (e.g. multilayer exfoliated graphene [1, 11] and single-layer CVD graphene with a bowtie geometry [4, 10]). It is

not yet clarified, whether this different behavior can be attributed to fabrication differences or distinct driving protocols.

3.3. Substrate and Atmosphere effect on the EB process

The EB of graphene is commonly attributed to an electroburning process [1, 2]: due to the current induced high local temperature the graphene atoms oxidize at the hottest point of the junction and form a nanogap. Under high vacuum, however, a much smaller number of oxygen molecules are available and other processes may take place, similarly as in the study of carbon nanotubes [12], where electroburning is replaced by oxide failure/sublimation as the pressure is decreased. To study this effect, we performed EB measurements both in air and in high vacuum. In addition to the pressure, we also varied the length of the voltage pulses.

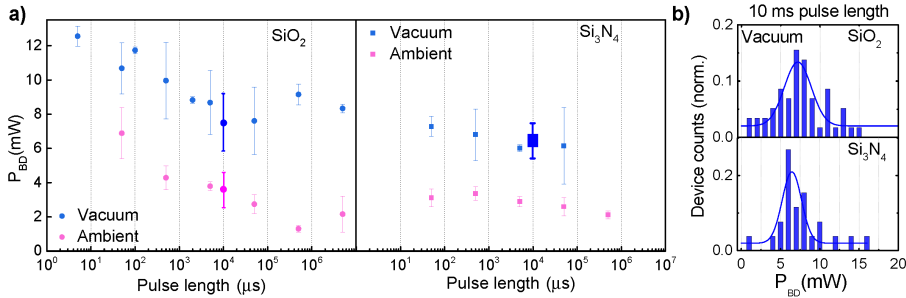


Figure 3.2: Evolution of the breaking power. a) Average breakdown power for graphene nanostructures on SiO₂ (left) and on Si₃N₄ (right) as a function of pulse length in vacuum (blue) and under ambient conditions (pink). An average breakdown power is calculated from measurements of 2 to 5 devices (small symbols). b) Distribution of the breakdown powers for Si₃N₄ and SiO₂ for a pulse length of 10 ms in vacuum. Measurements are reported from 52 devices for SiO₂ and 24 devices for Si₃N₄. The lines correspond to the gaussian fit of the distribution. As a reference the mean values and the standard deviations of the fitted gaussians are represented as larger symbols panel a). Similar measurements were carried out for SiO₂ in air (large pink dot). The corresponding distribution is not shown. The error bars represent the standard deviation of these datapoints.

For all pulse lengths, an average power was calculated from measurements on 2 to 5 devices on Si₃N₄ and SiO₂ substrates (Fig. 7.2a, small symbols) under ambient conditions and in vacuum ($p = 10^{-7}$ mbar). The figures clearly show that for both substrates a higher power is needed for the breakdown in vacuum than in air. We also notice that on average, a higher power is required to break a junction on a SiO₂ substrate than on Si₃N₄. A larger number of devices were measured in vacuum with 10 ms pulse length for both substrates. The corresponding distribution of breakdown power is shown in Fig. 3.2b. An average value and a standard deviation are extracted from the data using a Gaussian fit. The values of the fit parameters are plotted in the left panel (bigger symbols with error bar representing the standard deviation). We can notice that the values extracted from measurements of a higher number of devices are in a good agreement with the trend observed during the change of the pulse length.

3.4. Heat study

To study the effect of oxygen from the atmosphere on the EB process, we first estimate the number of oxygen molecules arriving on a single atomic site during the breakdown process. According to the kinetic theory of gases the flux of oxygen molecules from 2π solid angle to the graphene sample is $j_{\text{ox}} = n_{\text{ox}}\bar{v}/4$, where n_{ox} and \bar{v} are the density and the average speed of the oxygen molecules. These quantities are defined as $n_{\text{ox}} = \alpha_{\text{ox}}p/(k_{\text{B}}T)$, where $\alpha_{\text{ox}} = 0.21$ is the fraction of oxygen molecules in air, p is the pressure, $T = 300\text{K}$ is the temperature and k_{B} is the Boltzmann constant. The average speed of the oxygen molecules is expressed as $\bar{v} = \sqrt{\frac{8k_{\text{B}}T}{\pi\mu}}$, where $\mu = 5.31 \times 10^{-26}\text{kg}$ is the mass of an oxygen molecule. From these the number of oxygen molecules arriving to a half unit cell of graphene (single atomic site) during a single pulse is $N \approx 1.5 \times 10^7 \cdot \tau \cdot p/p_{\text{ambient}}$, where τ is the pulse length in seconds, and p_{ambient} is the atmospheric pressure. Since the carrier cooling time for graphene is in the order of picoseconds [13], we consider the heating/cooling time constant much shorter than our pulse length, i.e. we assume that our graphene bridge is hot only during the pulse. Based on all these, with the pressure (10^{-7} mbar to 1 bar) and with the pulse length ($5\mu\text{s}$ to 5 s) we can experimentally tune the number of oxygen molecules hitting an atomic site during a single pulse by 16 orders of magnitude.

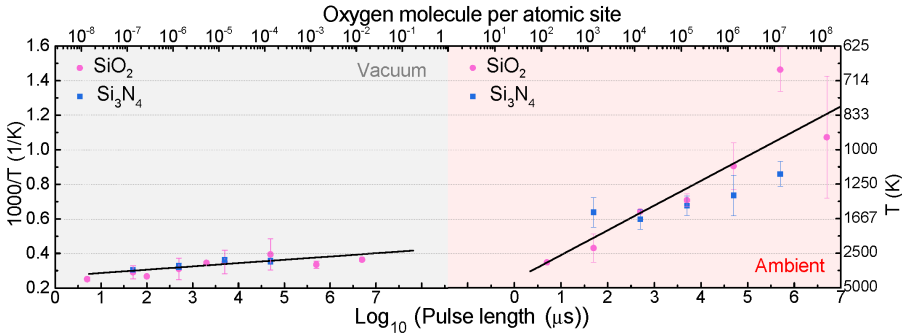


Figure 3.3: Temperature during EB process. Arrhenius plot of $1/T$ as a function of the logarithmic pulse length for Si_3N_4 (in blue) and SiO_2 (in pink). The top axis is scaled to the number of oxygen molecules arriving on a single atomic site during a single EB pulse. The right axis shows the maximum temperature within the junction. To estimate the temperature, we fixed the thermal conductivities to $\kappa_{\text{g}} = 1000\text{WK}^{-1}\text{m}^{-1}$, $\kappa_{\text{ox}} = 1.4\text{WK}^{-1}\text{m}^{-1}$ and $\kappa_{\text{ni}} = 30\text{WK}^{-1}\text{m}^{-1}$, and the thermal boundary resistivity $\rho_{\text{gox}} = 1 \times 10^{-8}\text{m}^2\text{K/W}$. To determine the activation energies two separate lines were fitted to the vacuum and the ambient regions. The thermal boundary resistivity ρ_{gni} was tuned to achieve the least squared deviation between the temperatures calculated for Si_3N_4 and SiO_2 . This procedure yielded $\rho_{\text{gni}} = 4.8 \times 10^{-7}\text{m}^2\text{K/W}$.

To interpret the data in terms of electroburning, it is useful to give a common axis to Figs. 3.2a showing the number of oxygen molecules hitting an atomic site during a single pulse. This rescaled top axis is shown in Fig. 3.3, such that the vertical axis is scaled to temperature (see later), and the raw power data with the common top axis are shown in Fig. S1 of the supporting information. In high vacuum, the number of oxygen molecules/atomic site during the breakdown is much smaller than 1 for any pulse length, indicating that a breakdown process different than burning may take place. One could still speculate that the oxygen from the SiO_2 substrate may take part in the burning process even in the absence of atmospheric

oxygen, however, the fact, that on Si_3N_4 substrate a similar EB is observed in vacuum stands against this assumption. In this regime we rather attribute the breakdown to the sublimation of graphene. In the following, we try to understand the different breakdown processes using a heat transport model.

As the EB shows similar tendencies on both substrates, we assume that both on SiO_2 and on Si_3N_4 the same physical processes are involved in the breakdown. This means, that at a given pulse length and pressure the breakdown should happen at the same local temperature of graphene regardless of the chosen substrate. Therefore we wish to rescale the axis of the breakdown power to the maximal local temperature of the graphene junction when the EB happens. To estimate the power dependence of the temperature of the graphene constriction during EB, one can use the analytic solution of the 1D heat equation [11]. Assuming that the temperature at the contacts is fixed to room temperature (T_0), one obtains:

$$T(x) = T_0 + \frac{p_x}{g} \left(1 - \frac{\cosh(x/L_H)}{\cosh(L/2L_H)} \right). \quad (3.1)$$

Here $L = 800 \text{ nm}$ is the length of the constriction, g is the thermal conductance to the substrate per unit length, p_x is the Joule heating rate in Watts per unit length, and L_H is the *thermal healing length* defined as: $L_H = \sqrt{\frac{\kappa_g W t_g}{g}}$, where $t_g = 0.335 \text{ nm}$ is the thickness of a monolayer of graphene, $W = 400 \text{ nm}$ is the width of the constriction, and κ_g is the heat conductivity of graphene. Throughout our calculations we use a constant heat conductivity of $\kappa_g = 1000 \text{ WK}^{-1}\text{m}^{-1}$, which is consistent with the data from J. O. Island et al. [11] For the SiO_2 substrate the thermal conductance to the substrate is calculated as:

$$g_{\text{ox}} = \frac{1}{\frac{t_{\text{ox}}}{\kappa_{\text{ox}} W} + \frac{\rho_{\text{gox}}}{W}}, \quad (3.2)$$

where t_{ox} corresponds to the 300 nm oxide thickness, κ_{ox} is the thermal conductivity of the oxide and ρ_{gox} is the thermal boundary resistivity between the graphene constriction and the oxide substrate. In the case of Si_3N_4 , we use the following expression:

$$g_{\text{ni}} = \frac{1}{\frac{t_{\text{ni}}}{\kappa_{\text{ni}} W} + \frac{t_{\text{ox}}}{\kappa_{\text{ox}} W} + \frac{\rho_{\text{gni}}}{W}}. \quad (3.3)$$

where t_{ox} corresponds to the 80 nm oxide thickness, t_{ni} to the 140 nm nitride thickness, κ_{ni} to the thermal conductivity of the nitride and ρ_{gni} to the thermal boundary resistivity between the graphene constriction and the nitride substrate.

The parameters used for our model are given in the caption of Fig. 3.3. All the parameters were taken from literature [11, 14], except the thermal boundary resistivity between Si_3N_4 and graphene, for which we are not aware of any prior measurement. Relying on the assumption that the breakdown should happen at the same temperature using SiO_2 or Si_3N_4 , we use ρ_{gni} as a fitting parameter to obtain the least squared deviation between the breakdown temperatures on both substrates at the various pulse lengths and pressures. This fitting yields a value of $\rho_{\text{gni}} = 4.8 \times 10^{-7} \text{ m}^2 \text{ K/W}$ for the thermal boundary resistivity. Note, that this value is more than an order of magnitude larger than the thermal boundary resistivity for SiO_2 , which indicates weak van der Waals interactions between graphene and

the Si_3N_4 substrate.

As both the electroburning and the sublimation are activated processes, the number of reactions per unit area and unit time can be written as:

$$\frac{N}{A \cdot t} = C \cdot e^{-\frac{E_a}{k_B T}}, \quad (3.4)$$

where E_a is the activation energy, and C is a pre-exponential parameter. We assume that in all the breakdown processes a similar number of carbon atoms are involved in the reaction, and so N/A is assumed to be the same for any pulse length. With this

$$\log_{10}(\tau) = \log_{10}\left(\frac{N}{C \cdot A}\right) + \frac{E_a \cdot \log_{10} e}{k_B} \cdot \frac{1}{T} \quad (3.5)$$

follows, where the first term on the right side is constant, thus the slope between $\log_{10}(\tau)$ and $1/T$ yields the activation energy. Fig. 3.3 presents the Arrhenius plot of the inverse of the calculated temperature at $x = 0$ (left axis) as a function the logarithm of the pulse length for both substrates, together with the common linear fits. On the right axis the corresponding temperature is shown. For the EB in vacuum all the data points are close to the fitting line, whereas at ambient conditions a larger scattering of the data is observed, nevertheless it is clear that the two regions yield significantly different activation energies. From the slopes of the fits the activation energy in vacuum is 10.4 ± 2.4 eV, whereas in air it is 1.38 ± 0.28 eV, where the uncertainties are related to the statistical error of the linear fit, but do not include the error of the calculated temperature due to the uncertainties in the parameters of the thermal model. As an example, changing the heat conductance κ_g to $2000 \text{ WK}^{-1} \text{ m}^{-1}$ would result in activation energies of 7.5 ± 1.7 eV in high vacuum and 1.15 ± 0.22 eV in air. A more detailed analysis on the sensitivity to the parameters of the thermal model are given in the supporting information. As a comparison, prior studies have reported ~ 7 eV activation energy for the sublimation of carbon atoms in the graphene lattice in presence of defects [15–17], and 1 – 2 eV activation energy for the burning process [18]. Based on all these we can state that the interpretation of the EB process as graphene sublimation in high vacuum and as electroburning in air is consistent based on the estimated activation energies.

3.5. Effect of the thermal transport parameters on the estimated junction temperature and the activation energies

As the estimation of the junction temperature relies on somewhat uncertain thermal transport parameters, we investigate the stability of our results against the variation of these factors in the case of the SiO_2 substrate. The heat conductivity of SiO_2 (κ_{ox}) is relatively well known, so we focus our analysis on the variation of the heat conductivity of graphene (κ_g) and the thermal boundary resistivity towards the SiO_2 substrate ($\rho_{g,ox}$). The black curves in Fig. ?? are replottting the black lines of Fig. 3.3 for ambient and vacuum conditions using a linear temperature scale instead of the Arrhenius plot. These curves are calculated using the reference thermal transport parameters, that were applied for our analysis in the previous section. The blue/light blue curves demonstrate the calculated junction temperature using a doubled/halved thermal conductivity of graphene compared to the value used in the main

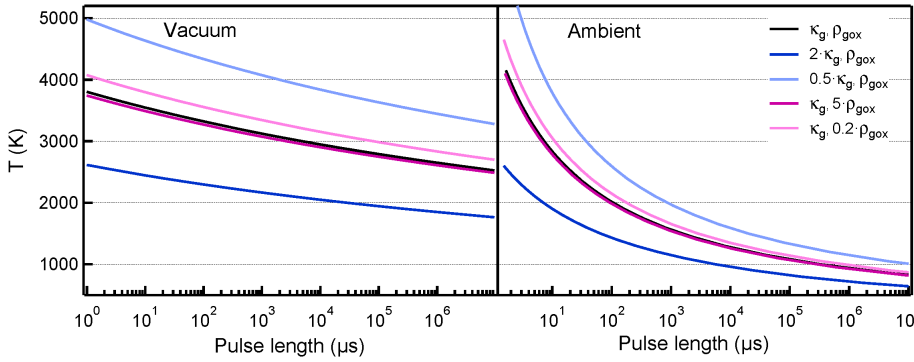


Figure 3.4: Effect of the thermal conductivity of graphene (κ_g) and the thermal boundary resistivity towards the SiO_2 substrate (ρ_{gox}) on the estimated breakdown temperature. The black curves are equivalent to the black fitting lines in Fig. 3 of the manuscript. First these curves are scaled back to breakdown power applying equation (1) of the main text with the thermal transport parameters used in the main text, and then these pulse length dependent power values are scaled to breakdown temperature using the same equation with detuned thermal transport parameters.

text, and keeping the the thermal boundary resistivity towards the substrate unchanged. The purple/pink curves demonstrate the estimated temperature using five times larger/smaller ρ_{gox} with unchanged κ_g . It is clear that the thermal conductivity of graphene has more pronounced influence on the junction temperature than the thermal boundary resistivity towards the substrate.

We have also calculated the activation energies corresponding to these detuned parameters, as shown by the table bellow. The results demonstrate that a factor of two detuning of κ_g yields only $\approx 20 - 30\%$ variation of the calculated activation energies, whereas a factor of five detuning of ρ_{gox} has even less influence on the results. Based on this analysis we can state that our results are stable against the chosen thermal transport parameters: in a broad interval of the these the estimated sublimation and burning activation energies remain consistent with the values known from the literature. The 7-8 times difference between the estimated activation energies in vacuum and in air is even less sensitive to the chosen parameters, clearly demonstrating the fundamental difference between the two breakdown processes.

	κ_g, ρ_{gox}	$2\kappa_g, \rho_{gox}$	$0.5\kappa_g, \rho_{gox}$	$\kappa_g, 5\rho_{gox}$	$\kappa_g, 0.2\rho_{gox}$
κ_g ($WK^{-1}m^{-1}$)	1000	2000	500	1000	1000
ρ_{gox} ($1E-8m^2K/W$)	1	1	1	5	0.2
E_a (eV) ambient	1.38	1.15	1.63	1.44	1.37
E_a (eV) vacuum	10.4	7.52	13.3	11.1	10.3

3.6. Conclusion

In summary, we have studied the EB process, used for creating graphene nanogaps, under different conditions. We have shown, that the process of breakdown is different for low and

high oxygen concentration. At high oxygen concentration a conventional electroburning process takes place. As pressure is lowered, the system enters a regime where no oxygen molecules can reach the junction during a single voltage pulse. In this regime, the EB process can still take place but at a significantly higher power than in ambient conditions. Based on the systematic study of the breakdown power at various pulse lengths, and the conversion of power to contact temperature based on a thermal model we have estimated the activation energies of the involved processes. According to this analysis the EB process is shown to be consistent with electroburning at ambient conditions and sublimation in high vacuum. By performing a comparative study using SiO_2 and Si_3N_4 substrates we have also shown, that the oxygen originating from SiO_2 does not play a substantial role in the breakdown process.

3.7. Outlook

Understanding the fracture mechanics of 2d materials in general and graphene, in particular, is attracting a lot of interest [19–22]. Indeed, the electronic properties of graphene are very sensitive to its edge termination. For example, edges with a certain degree of electron-hole symmetry near the Fermi level support quantum-confined electronic states relevant for anisotropic electron and spin transport [23–27]. The understanding and control of the propagation of cracks in graphene along the selected axis are necessary to achieve a controlled formation of edges. TEM and LEM measurements have shown that the propagation of cracks in graphene follows both armchair and zigzag edges that are considered as predominant axes [19, 21]. These observations were explained theoretically by a nonmonotonic dependence of graphene edge energy on the edge orientation with respect to the lattice.

Based on these observations, one can expect that in the sublimation regime, the nanogap formation will probably start at a defect and follow the crystallographic axis with the lowest energy. Therefore, EB on large grain graphene shall create gaps with better-defined edges. We have performed the first tests on a sample with large grain graphene. From the SEM image (Fig. 3.6), we could observe a gap with a regular shape and 60° angle between its different axes. Nevertheless, a deep study has to be performed to gain more understanding of the edge structure and termination of the gaps.

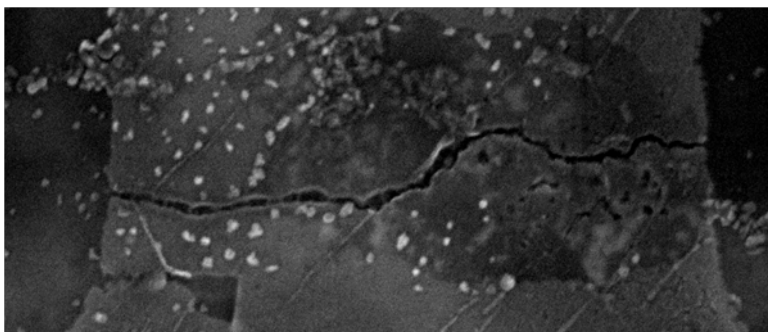


Figure 3.5: SEM image of a graphene junction after EB.

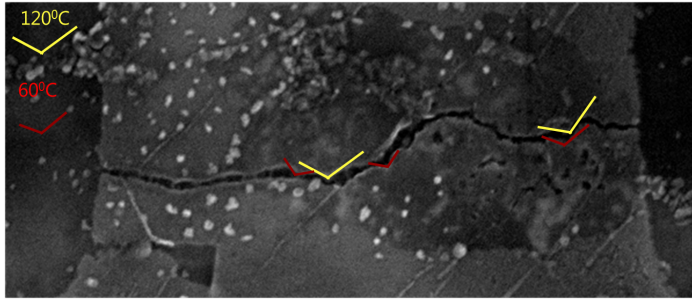


Figure 3.6: SEM image of a graphene junction after EB. 60 and 120^{circ}C angles are marked resp. with red and yellow lines.

Contributions This chapter has been published *Nanoscale*, 2017,9, 17312-17317. The authors are Maria El Abbassi, Laszlo Posa, Peter Makk, Cornelia Nef, Kishan Thodkar, Andras Halbritter, and M. Calame. K.T provided the CVD graphene. M.E made the samples. M.E and L.P performed the measurements and the analysis. All the authors contributed to the data analysis and the manuscript writing.

Bibliography

- [1] F. Prins et al., *Nano Lett.*, 2011, 11 (11), pp 4607-4611
- [2] J. Mol et al., *Nanoscale*, 2015, 7, 13181
- [3] C. Jia et al., *Science*, 2016, Vol. 352, Issue 6292, pp. 1443-1445
- [4] C. S. Lau et al., *Phys. Chem. Chem. Phys.*, 2014, 16, 20398-20401
- [5] C. Nef et al., *Nanoscale*, 2014, 6, 7249
- [6] Beilstein *J. Nanotechnol.* 2015, 6, 711-719
- [7] L. Grosse et al., *Nature Nanotechnology* 6, 287-290 (2011)
- [8] J. Moser et al., *Appl. Phys. Lett.* 91, 163513 (2007)
- [9] J. G. Simmons, *J. Appl. Phys.* 34, 1793 (1963)
- [10] P. Gehring et al., *Nano Lett.*, 2016, 16 (7), 4210-4216
- [11] J. O. Island et al., *Journal of Physics: Condensed Matter*, 2014, 26, 474205
- [12] A. Liao et al., *Phys. Rev. B* 82, 205406
- [13] K. J. Tielrooij et al., *Nature Nanotechnol.* 2015, 10, 437-443
- [14] A. A. Balandin, *Nano Lett.*, 2008, 8 (3), pp 902-907
- [15] J.Y. Huang et al., *PNAS* 2009 106 (25) 10103-10108
- [16] A. Santana et al., *Chemical Physics Letters*, 557, 2013, 80-87
- [17] A. Barreiro et al., *Nano Lett.*, 2012, 12 (4), 1873-1878
- [18] N. Tao et al., *J. Phys. Chem. C*, 2011, 115 (11), pp 4730-4737
- [19] K. Kim et al., *Nano Lett.*, 2012, 12 (1), pp 293-297
- [20] Y. Guo et al., *ACS Nano*, 2016, 10 (9), pp 8980-8988
- [21] F. Meng et al., *J. Phys. Chem. Lett.*, 2015, 6 (20), pp 4038-4042
- [22] M. Fujihara et al., *ACS Nano*, 2015, 9 (9), pp 9027-9033
- [23] M. Fujita et al., *J. Phys. Soc. Jpn.* 65, 19201923 (1996).

- [24] Y.-W. Son et al., *Nature*, 444, 347 (2006).
- [25] A. H. Castro Neto et al., *Rev. Mod. Phys.* 81, 109 (2009).
- [26] K. A. Ritter et al., *Nat. Mater.* 8, 235 (2009).
- [27] M. Wimmer et al., *Phys. Rev. B* 82, 045409 (2010).

Part II

Graphene tunnel junctions

4 Characterisation of the graphene tunnel junctions

In this chapter, we report on the Raman spectroscopy and electrical measurements performed on graphene nanogaps after electrical breakdown (EB). Raman spectra were measured to investigate the quality of the graphene. In addition, IV curves of the junctions were recorded at different temperatures and gate voltages. Finally, the junction size was estimated using the Simmons model for fitting individual IV curves.

4.1. Introduction

An in-depth understanding of the graphene tunnel junctions is of great importance for the reliability of the molecular junctions formed with those gaps, as the cleanliness of the gap, the edge structure and the presence of defects in the gap region have a strong influence on charge transport [1, 2]. They may interfere with or even mask the signature of the molecule. For this reason, we performed systematic electrical measurements of the gaps after the electric breakdown (EB) process, before the deposition of the molecules. We also recorded Raman spectra to assess the quality of the graphene films.

4.2. Raman spectroscopy

EB of graphene nanogaps was carried out as described in the previous chapter. After EB, Raman mapping was performed to check the quality of the graphene and characterize the gap region. One of the main limitations of this spectroscopy technique is the fact that the laser spot size is diffraction limited. Using a 785nm laser yields a lower limit for the diameter of about 400 nm. Figure 4.1 compares a spectrum recorded in the gap region with one obtained for the rest of the graphene bridge. The plot shows significant differences between the two spectra, with a decrease in intensity for the 2D and G peak and an increase of the intensity of the D peak in the gap region. Figure 4.1b) presents a two-dimensional (2d) map of the intensity of the 2D peak of a graphene device. The global intensity of the 2D peak is homogeneous over the graphene bridge, except for a dark line, which we attribute to the gap region, where the intensity is drastically decreased. This could indicate the presence of amorphous carbon and/or disordered graphene [3], in agreement with the characteristics of the EB process during which high temperatures are reached.

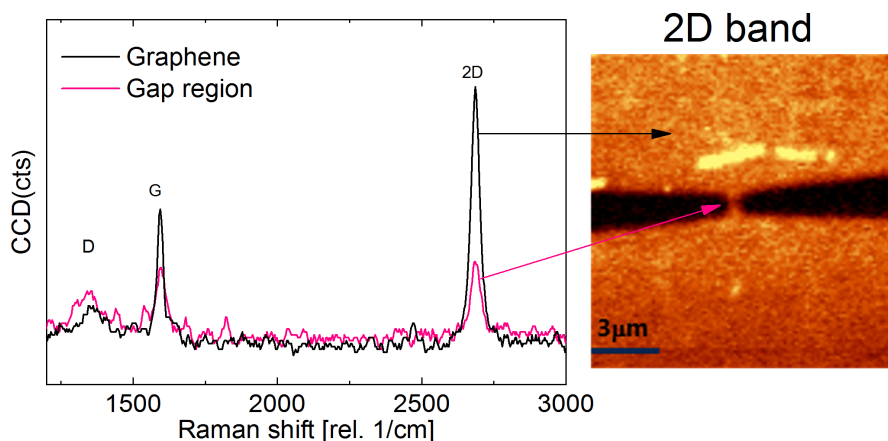


Figure 4.1: Raman characterization of a graphene junction after EB. The purple/black curve corresponds to a scan near/far from the gap region. b) 2d Raman map of the intensity of the 2D peak in the region around the constriction. A strong contrast in the intensity is observed between the graphene constriction and the gap region.

4.3. Estimation of the gap size by Simmons fitting

The size of the nanogap dictates the types of molecules which can be contacted. It is therefore important to get an estimate of the gap size after EB. This can be done by fitting tunneling curves to the Simmons tunneling model. For an electron tunneling between two electrodes separated by a gap region, modeled by a rectangular barrier, the model has three parameters, namely the work function of the electrode material Φ , the gap size d , and gap area A . The current I can be expressed as:

$$I = \frac{Ae}{4\pi^2\hbar^2} \left(\left(\Phi - \frac{eV_{bias}}{2} \right) \exp \left(\frac{-2d}{\hbar} \sqrt{2m} \sqrt{\Phi - \frac{eV_{bias}}{2}} \right) - \left(\Phi + \frac{eV_{bias}}{2} \right) \exp \left(\frac{-2d}{\hbar} \sqrt{2m} \sqrt{\Phi + \frac{eV_{bias}}{2}} \right) \right) \quad (4.1)$$

e is the elementary charger, \hbar is the reduced Planck's constant and V_{bias} is potential applied. When applying the Simmons model [4], one has to be careful, as different combinations of parameters may provide very similar fitting curves. In case of graphene, an educated guess of the area may solve part of this issue, as we can anticipate that the junction width is larger than a single atom and smaller than the initial cross section of the graphene nanoribbon (400 nm). The height is assumed to be a single carbon atom. To account for this uncertainty in the actual junction area, we performed the Simmons fitting procedure using these two limiting cross sections, and argue that the actual junction width is located between the obtained limiting values, resulting in a sub-nm uncertainty in gap size. Figure.4.2 presents the distribution of the estimated gap sizes for the two different substrates used previously (SiO_2 and Si_3N_4). To perform the fit, the junction area was fixed to 0.01 and 100 nm^2 (resp. purple and gray). For both substrates, we obtain a distribution of gap sizes with a mean value around 1 – 1.5 nm independently on the junction area.

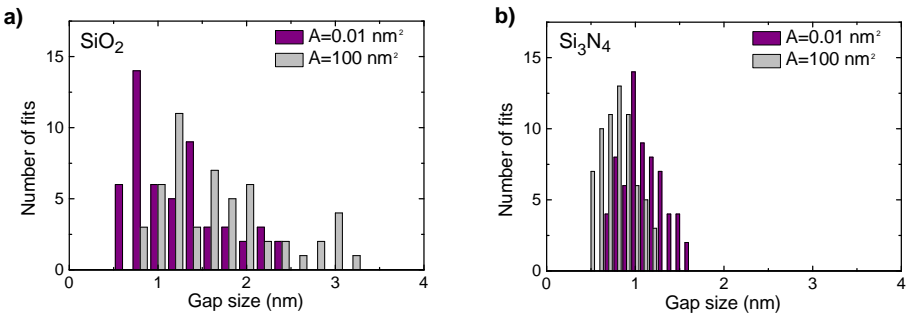


Figure 4.2: Histogram of the gap size estimation by fitting to the Simmons model after EB in vacuum. The fit procedure is performed by fixing the tunneling area to 0.01 nm^2 (purple) and 100 nm^2 (gray). Panel a) corresponds to gaps on SiO_2 and b) to gaps on Si_3N_4 .

4.4. Simulation of the effect of the gate on tunneling junctions using the Simmons model

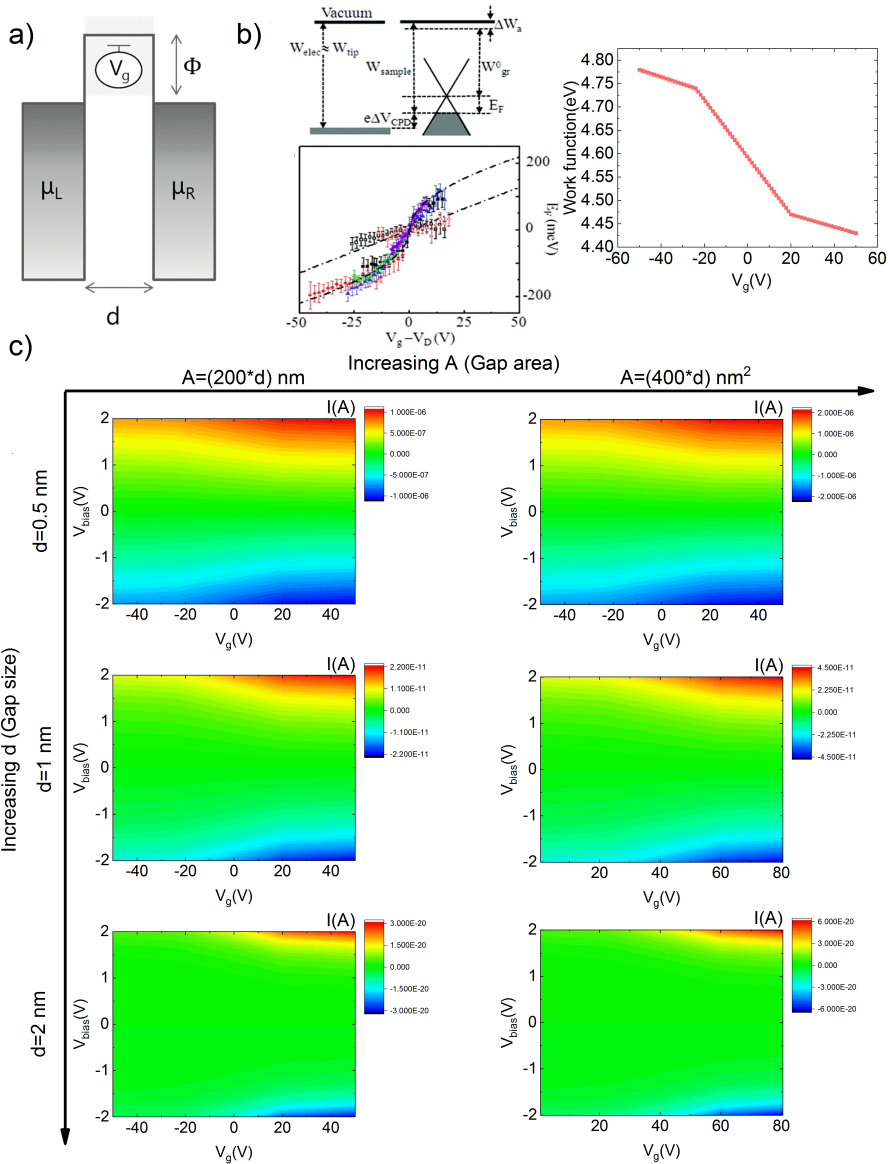


Figure 4.3: Simulation of the effect of the gate on tunneling junctions using the Simmons model. a) Drawing of a tunnel junction assuming a rectangular barrier. b) Dependence of the graphene work function on the gate voltage, extracted from literature [7]. c) Simulated values of IV curves function of gate voltage calculated by combining the Simmons model with the experimental values in b).

To estimate the effect of gating on the tunneling behavior, we used a simple model based

on Simmons tunneling theory [4]. We first consider that the energy barrier Φ of the Simmons model is approximately the graphene work function (Fig.4.3a) [5,6]. Secondly, we suppose that the main effect of the gate voltage will be a shift of the Fermi energy of the electrodes inducing a change of the graphene work function. Figure 4.3b) presents the dependence of the graphene work function on the gate voltage, extracted from Ref. [7]). These data show that increasing the Fermi energy position when applying a gate voltage induces a decrease of the graphene work function. Using those values (Figure.4.3b)), we calculate the corresponding IV-curves using the Simmons formula for three different gap sizes ($d=1,2$ and 3 nm) and two different widths ($w=200$ and 400 nm). Figure 4.3c), presents the simulated stability diagrams. The effect of the gating is a small increase of the conductance at higher gate voltages, meaning a lower energy barrier. This effect is weaker with increasing gap sizes at which the current decreases exponentially. We further comment on this on the paragraph below.

4.5. Gate dependence

After EB systematic gate-dependent measurements were performed at room temperature. This was done to ensure that the gaps are truly empty, with no carbon islands or other residues. Figure 4.4 shows the stability diagram at room temperature of (dirty) low resistance junction. The junctions show relatively high current (more than 1nA at 1V) and modulations of the current due at varying gate voltage. However, only a minority of the samples exhibited such strong gate dependence. All these devices had relatively small resistance smaller than ($1M\Omega$). This behavior can be attributed to the presence of weakly coupled carbon islands or to strongly coupled graphene filaments bridging the two electrodes [1]. Due to the small size of the gap, the energies of the carbon islands are very close to the one of a molecule and could interfere with it. To avoid such issues, only devices with a resistance in the $G\Omega$ regime were considered and measured after molecular deposition.

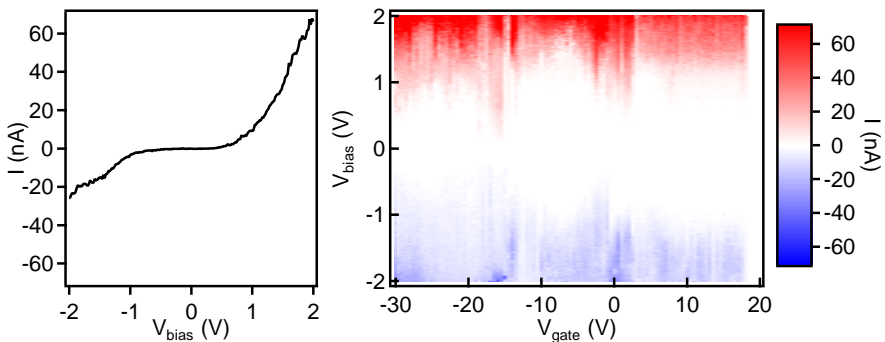


Figure 4.4: Room temperature characterization of a (dirty) low resistance junction after EB. The left panel corresponds to a typical I-V at zero gate voltage. The right panel corresponds to the gate dependent characterization of the gap. A strong gate dependence is observed at room temperature.

But for the majority of the devices (more than 70%) no gate dependence was observed, indicating the formation of empty gaps. Figure 4.5 presents the stability diagram at 12K of

two devices showing weak gate dependence. A small increase of current is observed for the first device at increasing gate voltage value and can be attributed to a decrease of the work function explained in the previous section.

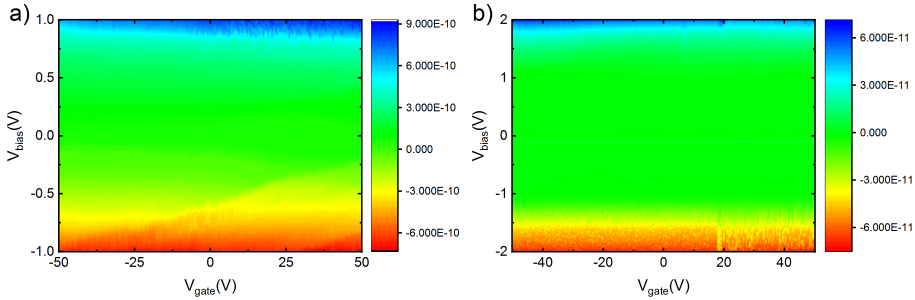


Figure 4.5: Characterization of clean junctions after EB at 12K. Stability diagram of two junctions represented in a) and b) showing a weak gate dependence.

4.6. Temperature dependence

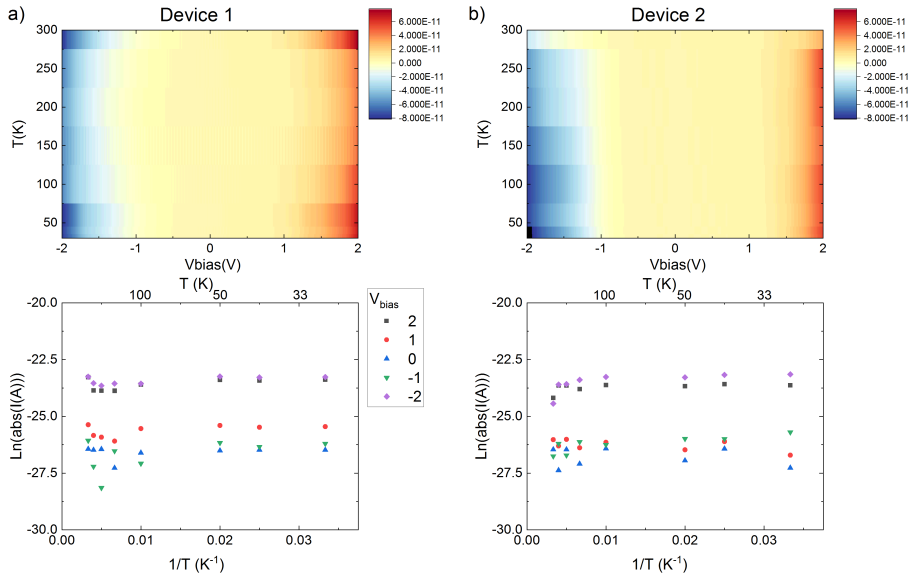


Figure 4.6: Effect of the temperature on the tunneling behavior. Two devices are represented in a) and b). The top panel represents the evolution of the IV curves from 20 to 300K. The bottom panel, contains cut of the logarithmic value of the current at different bias values function of the inverse of the temperature.

We have also performed characterization of some of the high resistance junctions at different temperatures. We recorded 100 IV curves at fixed temperatures between 20 and 300K. The top panel of Figure. 4.6 shows the evolution of the IV curves as a function of

temperature for two devices. The currents show little dependence on the temperature. The bottom panel of Figure. 4.6 shows the evolution of the logarithmic value of the current as a function of temperature at different bias values. The currents are flat over the entire temperature range, confirming the weak effect of temperature on tunneling through the graphene junction [5]. This can be explained by the weak dependence of the graphene electronic properties on temperature [8].

4.7. Conclusion

A detailed characterization of the graphene junctions before molecular deposition is important. Our measurements demonstrate that an *empty* graphene nanogap exhibits a tunneling current that is only weakly dependent on the gate voltage and temperature. Stability of the junctions over a large temperature range and weak effect of the gating make the graphene electrodes a good platform for measuring molecules.

4.8. Outlook: Measurements under a magnetic field

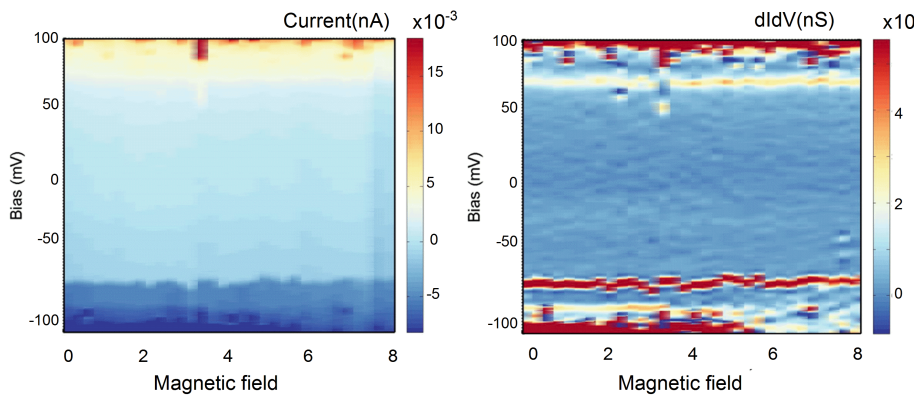


Figure 4.7: Effect of the magnetic field on the tunneling behavior.

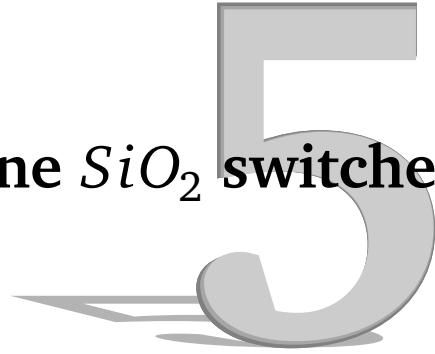
Recent theoretical calculations from Jaime Ferrer have predicted that depending on the graphene edges, spin-dependent transport may be observed in the graphene junctions. Thus, we were interested in the characterization of the effect of a magnetic field on the transport through our graphene junctions. The first measurements were done in collaboration with the group of Prof. Van der Zant in Delft and calculations were performed by Jaime Ferrer et al [9]. Figure .4.7 presents the evolution of the current and the differential conductance of an empty gap as a function of the magnetic field. For that device no significant dependence was observed except modulation in the intensity of the differential conductance $dIdV$ at varying magnetic field that still need to be understood.

Contributions Figure 4.2 is extracted from our paper published in *Nanoscale*, 2017,9, 17312-17317. The measurements of Figure4.7 were performed by Max Koole from Van der Zant group in Delft on a sample made by Maria El Abbassi in Basel.

Bibliography

- [1] P. Gehring, H. Sadeghi, S. Sangtarash, C.S. Lau, J. Liu, A. Ardavan, J.H. Warner, C.J. Lambert, G.A.D Briggs, and J.A. Mol. Quantum interference in graphene nanoconstrictions. *Nano letters*, 16(7):4210–4216, 2016.
- [2] D.J. Carrascal, VM. García-Suárez, and J. Ferrer. Impact of edge shape on the functionalities of graphene-based single-molecule electronics devices. *Phys. Rev. B*, 85(19):195434, 2012.
- [3] L.G. Cançado, A. Jorio, E.H Ferreira, Martins and F Stavale, C.A Achete, R.B Capaz, M.VO Moutinho, A. Lombardo, T.S Kulmala, A.C. and Ferrari. Quantifying Defects in Graphene via Raman Spectroscopy at Different Excitation Energies. *Nano Letters*, 11(8):3190-3196, 2011.
- [4] J. G. Simmons. Generalized Formula for the Electric Tunnel Effect between Similar Electrodes Separated by a Thin Insulating Film. *J. Appl. Phys.*, 34,1793, 1963.
- [5] F. Prins, A. Barreiro, J. W. Ruitenberg, J. S. Seldenthuis, N. Aliaga-Alcalde, L. M.K. Vandersypen, and H. S.J. van der Zant. Room-temperature gating of molecular junctions using few-layer graphene nanogap electrodes. *Nano letters*, 11(11):4607–4611, 2011.
- [6] C. S. Lau, J. A. Mol, J. H. Warner, and G. A. D. Briggs. Nanoscale control of graphene electrodes. *Physical chemistry chemical physics : PCCP*, 16(38):20398–20401, 2014.
- [7] Y.J. Yu, Y. Zhao, S. Ryu, L.E. Brus, K.S. Kim and P Kim. Tuning the Graphene Work Function by Electric Field Effect. *Nano Letters*, 9(10):3430-3434, 2009.
- [8] Y.-W. Tan, Y. Zhang, H.L. Stormer, and P Kim Temperature dependent electron transport in graphene *Eur. Phys. J. Special Topics*, 148, 15–18 (2007)
- [9] VM. García-Suárez, A. García-Fuente, D. Carrascal, M. Koole, E. Burzuri, H. S. J. van der Zant, M. El Abbassi, M. Calame, and J. Ferrer Spin signatures in the electrical response of graphene nanogaps. *to be submitted*

Graphene SiO_2 switches



A bias driven switching behavior was observed during the gaps characterization. In this chapter, we study this switching behavior that we associate to the formation of microscopically distinct SiO_x amorphous and crystalline phases between the graphene electrodes. The reset transition is attributed to an amorphization process due to a voltage driven self-heating; it can be triggered at any time by appropriate voltage levels. In contrast, the formation of the crystalline ON state is conditional and only occurs after the completion of a thermally-assisted structural rearrangement of the as-quenched OFF state which takes place within the dead time after a reset operation.

5.1. Introduction

While current CMOS technology is reaching the sub-10 nm regime, a broad consensus arises that a further boosting in computational power will primarily rely on novel circuit elements exhibiting an increased functional complexity as well as on beyond-von Neumann architectures benefiting from an improved interconnectivity of their building blocks. [1] Two-terminal resistance change memory devices (ReRAMs) [2–5] are outstanding candidates as they are not only scalable below 10 nm due to the filamentary nature of their resistive switchings but they also offer multi-bit operations via the analog tunability of their resistance states. The large scale integration of such devices on semiconductor industry compatible material platforms is demonstrated in the form of stacked crossbar arrays which are operated at reasonable current and voltage levels and a reduced thermal budget. [6–9] Non-volatile data storage is enabled by the widely observed exponential dependence of the set and reset times on the bias voltage which provides the means of fast programming at higher voltage and non-invasive readout at lower signal levels. [10, 11] This highly nonlinear behavior together with the possibility of multilevel programming provide the basis for a diverging number of applications ranging from long-term, non-volatile data storage to neural network modeling involving programmable learning and forgetting abilities among other synaptic functionalities. [1, 12, 13]

The two-terminal nature of ReRAM devices also offer the possibility of a major simplification with respect to conventional CMOS architectures relying on three-terminal, unipolarly driven units. However, the operation of various memristive devices utilizing bidirectional ion transport requires bipolar voltage signals. Alternatively, ReRAM cells exhibiting unipolar current-voltage $[I(V)]$ characteristics eliminate the need for such bipolar driving but this approach sacrifices the possibility of the zero bias read-out of the low and high resistance states. [14]

Here we report on the experimental observation of a complex memristive behavior in thermally grown SiO_x thin films where the active region of the resistive switching is confined under the 2 nm wide gap realized by controlled electrobreakdown of a narrow graphene constriction. We found that the switching dynamics is not only governed by the above mentioned, voltage dependent set/reset times but an additional independent timescale, the so-called *dead time* also appears playing a crucial role in the device operation: after switching the device OFF, the ON state cannot be restored as long as the dead time has not passed. This effect gives rise to the opportunity of reproducible transitions between unipolar and bipolar switching characteristics within the same nanodevice and thus programming its either state at zero bias by unipolar voltage signals. We also analyze the complex switching behavior arising from the coexistence of the strongly voltage dependent set and reset times and the dead time rule.

Planar nanogap structures defined by electromigration techniques over SiO_x substrates have also been investigated [15–17], however, only gap sizes exceeding 10 nm were studied. In contrast, the electrobreakdown protocol results in reproducible, high yield formation of <3 nm wide gaps between graphene electrodes. We anticipate that the intrinsic resistive switching in the underlying SiO_x layer also takes place within a similarly short lengthscale. We demonstrate a pronounced dead time effect, set and reset times <100 ns, large endurance and significantly smaller electroforming voltages than reported in larger SiO_x junctions.

5.2. Electrical characterization of the switch

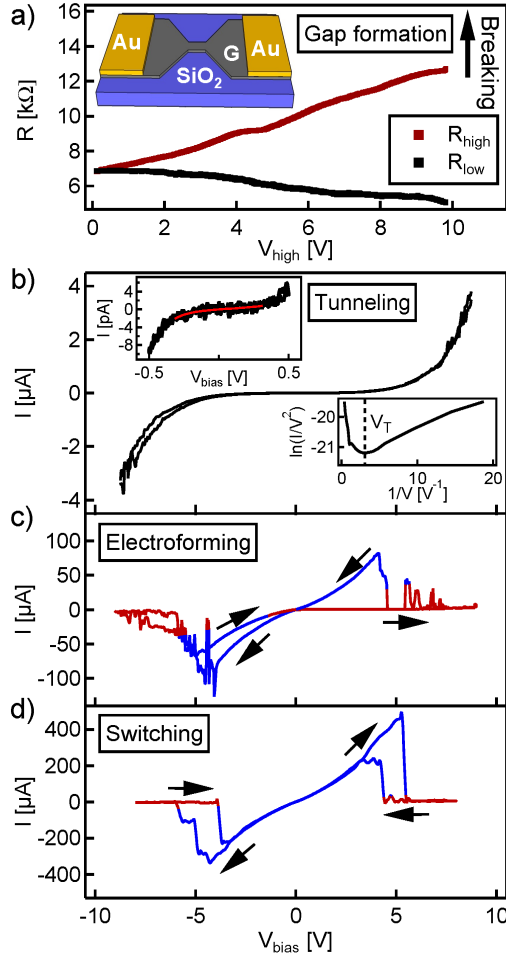


Figure 5.1: (a) Resistance during the electrobreakdown process at high bias (red) and low bias (black) as the function of the pulse amplitude. A sudden breakdown occurs at 9.8 V. The inset shows the schematics of the device. The graphene nanostripe at the middle is 800 nm long and 400 nm wide. (b) Electrical characterization of the tunnel junction after gap formation. By fitting the low bias trace to the Simmons model 2.0 ± 0.3 nm gap size was obtained (top inset). The minimum of the $\ln(I/V^2)$ vs. $1/V$ plot, V_T defines the voltage interval, where the Simmons fitting is applied (bottom inset). The junction exhibits an S-shaped tunneling $I(V)$ curve up to $V_{\max} = 8.75$ V (main panel). Higher amplitude voltage sweeps result in large current fluctuations signalling the electroforming process (c). After a few voltage sweeps an unipolar switching characteristics having well defined set and reset voltages is stabilized (d). The red/blue colored parts of the traces correspond to resistances higher/lower than the predefined threshold of $V/I = 150$ k Ω .

5.2.1. Electroformation of the Graphene- SiO_2 switch

After EB, we recorded $I(V)$ curves by applying an increasing amplitude voltage signal. At a typical threshold amplitude of 9V electroforming took place, i.e., the reproducible S-shaped $I(V)$ curve characteristic to pristine tunnel junctions (Fig. 5.1b) was replaced by a noisy and hysteretic trace (Fig. 5.1c). During repeated $I(V)$ measurements a clear unipolar switching behavior was observed, which became stable after a few voltage ramps (Fig. 5.1d). Starting from a low resistance ON state at zero bias the conductance of the junction drops abruptly at $V_{\text{reset}} = 5.5\text{V}$ switching the device to its high resistance OFF state. During the subsequent reverse voltage sweep the current increases suddenly at $V_{\text{set}} = 4.4\text{V}$ and the device switches back to the ON state. Due to the unipolar nature of the switching the same characteristic behavior can be seen at opposite voltage polarity and, consequently, the device is always set to its ON state at zero bias.

In accordance with previous studies [18, 19] we also found that resistive switching does not take place at ambient conditions. As the pressure increases the reset voltage is shifted to lower values and finally the sample cannot be set to its ON state any more. The switching reappears after reducing the pressure to its initial value.

Summarizing our characterization measurements, all the basic properties of the observed resistive switching were found to be consistent with previous studies on SiO_x switching devices contacted either by carbon or non-carbon electrodes. [15, 20, 21] As a sole difference we observe a significantly smaller electroforming voltage (9V) than the common values of 20–30V in other, larger SiO_x switches [20, 22]. It was shown that the electroforming voltage scales with the gap size, i.e. the electric field is the relevant parameter of the electroforming process. [20, 23] Accordingly, the small electroforming voltage in our measurements is attributed to the very small, nanometer scale gap size, which can be achieved by the controlled electrical breakdown of graphene.

5.2.2. Frequency dependence of the switching behavior

As a control measurement we tested 50 similar devices fabricated on amorphous silicon-nitride substrates, where larger work function values were obtained (3 – 5 eV) and no switching behavior was observed. This is in sharp contrast to the devices on SiO_x , where the absence of the switching phenomenon is exceptional. All these confirm that in our devices the switching indeed occurs in the SiO_x layer and not an intrinsic phenomenon of graphene [24–26] is observed.

SiO_x based ReRAMs were shown to exhibit reproducible switching between ON and OFF zero bias states [15]. Such an observation is clearly inconsistent with a unipolar current-voltage characteristics demonstrated in Fig. 5.1d and in the top curve of Fig. 5.2a, where the OFF state is inherently inaccessible at zero bias. In the following we analyze this issue in detail. We found that a clear unipolar behavior is only observed for slow bias sweeps (0.5Hz triangular signal with $V_{\text{max}} = 8\text{V}$ for the top curve in Fig. 5.2a). Increasing the speed of the $I(V)$ measurement a striking phenomenon is observed. At 2Hz frequency (middle curve in Fig. 5.2a) the $I(V)$ curve resembles a bipolar operation: the initially ON state device still switches OFF at the positive reset voltage, but during the positive polarity backward sweep it does not switch back to the ON state, rather the device ends up in the OFF state at zero bias. Increasing the voltage at negative polarity the device stays in the OFF state, and finally

during the negative polarity backward sweep it switches back to the ON state, which is the final state at the end of the driving period. At an even higher frequency (50 Hz, bottom curve in Fig. 5.2a) the $I(V)$ curve indicates a single-use memory operation: the initially ON state device switches OFF in the first quarter of the driving period but it does not switch back to the ON state along the rest of the cycle.

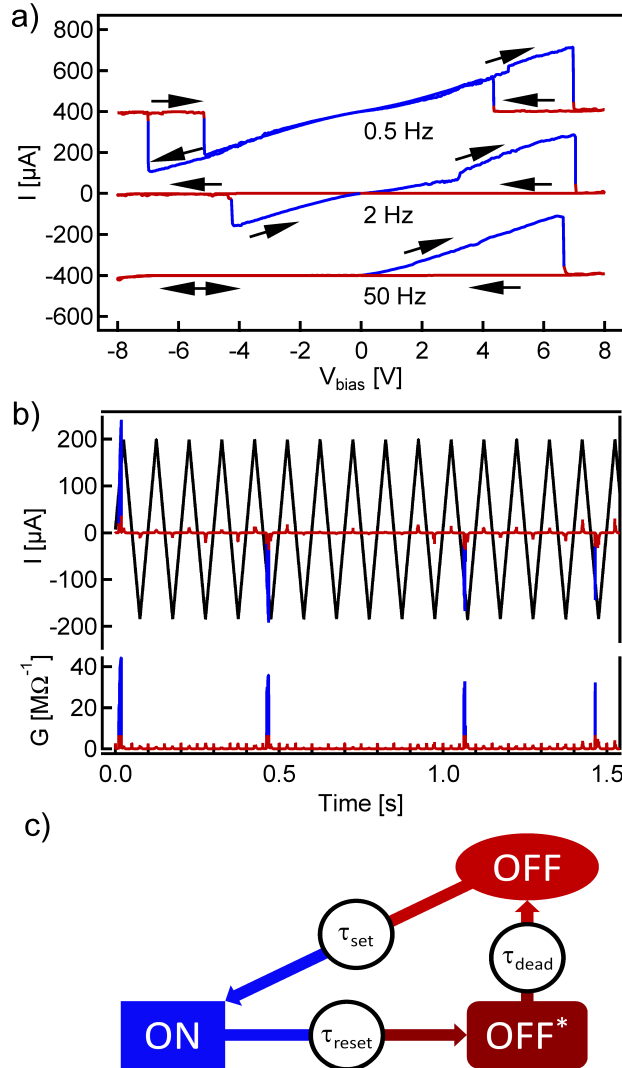


Figure 5.2: (a) Typical $I(V)$ curves measured at different driving frequencies. (b) Illustration of the dead time by applying multiple periods of a triangular voltage signal with an amplitude of 7.5 V and frequency of 10 Hz (black curve, voltage scale not shown). The current is measured simultaneously (red/blue). The bottom part demonstrates the corresponding conductance, $G = I/V$. (c) Cartoon illustrating the dead time rule and the timescales involved in the operation cycle.

5.3. Timescales determination

5.3.1. Dead time

To further investigate these phenomena, we applied multiple periods of the triangular driving signal (Fig. 5.2b). Following the convention applied for all switching figures in this Letter, the blue/red segments mark the ON/OFF states with the arbitrary threshold of $V/I = 150 \text{ k}\Omega$. Note that the small peaks in the red part of the curve correspond to the highly nonlinear current increase in the OFF states at high bias as demonstrated in the $I(V)$ trace shown in Fig. 5.1b. We found that the initially ON state device is switched OFF in the first quarter of the first driving period. Afterwards the device stays in the OFF state for 4 periods, and it finally switches back to the ON state in the 5th period. Similar behavior is observed during the following driving periods.

We describe all these observations by a simple operation rule: once the device is switched OFF, it is blocked in the OFF state for the period of the *dead time*, even if the driving signal level would be sufficient for initiating a set transition. Once the *dead time* has passed, the device can be switched ON again at the first appropriate set voltage level. A similar effect does not appear in the opposite switching direction: after the set process the device can be switched OFF without any dead time as illustrated by the flow chart of Fig. 5.2c. In the following we further investigate the three timescales (τ_{set} , τ_{reset} and τ_{dead}) governing the device operation by pulsed measurements.

We further analyzed the above dead time rule by performing pulsed measurements. Figure 5.3a shows a sequence of set and reset voltage pulses where the driving voltage between the pulses is set to zero. First the ON state is prepared by a set pulse with an amplitude of $V_{\text{set}} = 4.5 \text{ V}$, followed by a higher amplitude reset pulse ($V_{\text{reset}} = 9 \text{ V}$) to switch OFF the device. After this initialization protocol a second set pulse is applied with a varying delay time τ_{delay} with respect to the reset pulse. If this delay time is shorter than the dead time (top curve), the set pulse cannot switch ON the device, whereas at $\tau_{\text{delay}} > \tau_{\text{dead}}$ (bottom curve) the set pulse can induce a set transition, in accordance with the dead time rule. Based on a statistical ensemble of measurements we have determined the $F(\tau_{\text{dead}})$ cumulative probability distribution function of the dead time as shown by the dots in Fig. 5.3c. The green line represents a Gaussian distribution function fitted to the data. The corresponding $\rho(\tau_{\text{dead}})$ Gaussian probability density function (the derivative of $F(\tau_{\text{dead}})$) is shown by the green line in Fig. 5.3d revealing a dead time of $\tau_{\text{dead}} = 120 \pm 31 \text{ ms}$, where the error stands for the standard deviation of the Gaussian. (Note that the probability density functions are plotted in a normalized fashion with unity peak amplitudes in Fig. 5.3 for clarity.)

We emphasize that even the initializing pulse sequence of Fig. 5.3a would not work without the dead time rule: if the unipolar $I(V)$ characteristics of the top curve in Fig. 5.2a would hold for any driving speed, then the reset pulse could only switch OFF the device temporarily, but by the end of the pulse, as the driving voltage falls to zero, the device would immediately switch ON again. In contrast, utilizing the dead time rule the device can be set to both its ON and OFF states at zero bias by the proper choice of the unipolar pulse sequences.

An alternative method to deduce the dead time in the same device is illustrated in Fig. 5.3b. A pulsing scheme is applied, where the same reset pulse initializes the device to its OFF state, but after this pulse the voltage is kept constant at the set value of 4.5 V (see

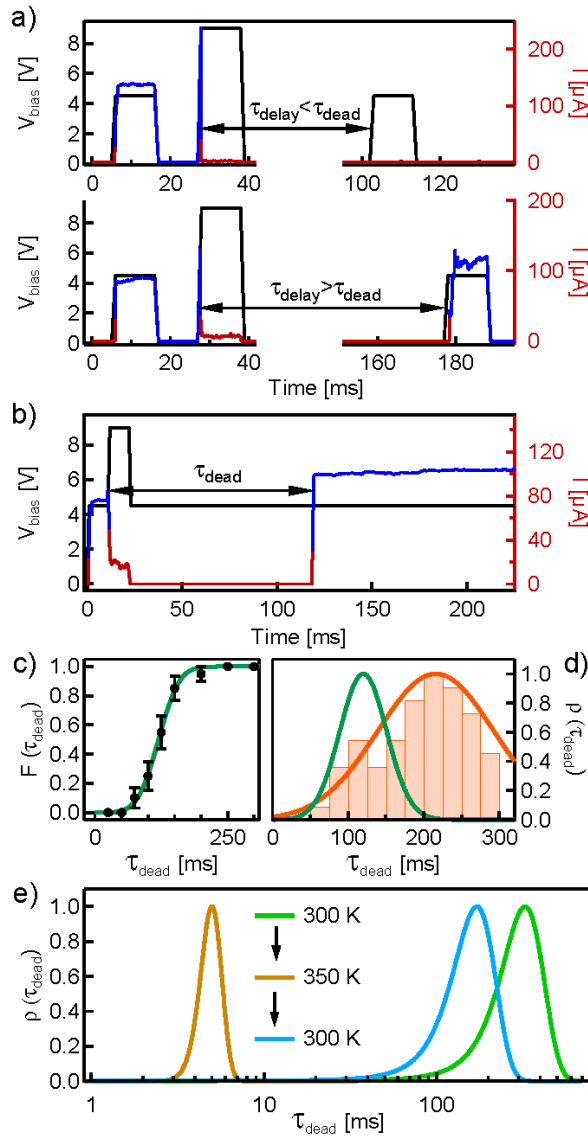


Figure 5.3: Deducing the dead time by two different pulse sequences: The device is initialized by a set and subsequent reset transition. The next set voltage pulse is applied after a zero bias waiting period (a). The amplitude of the set pulse is adjusted to a voltage level which grants a < 2 ms set time (see Fig. 5.4b). Alternatively, the set voltage is constantly applied after similar initialization (b). Using the scheme of panel (a) the probability of the set transition upon the delayed set pulse is evaluated based on an ensemble of 20 measurements performed at each delay time setting (c). A Gaussian probability distribution fitted to the data (black dots) and the corresponding density function are displayed by the green lines in (c) and (d), respectively. The orange histogram summarizing 65 independent measurements and its Gaussian fitting in panel (d) show the statistical distribution of the dead times directly deduced by using the scheme of panel (b). (e) The similarly evaluated probability density functions of the dead times along a thermal cycle.

black curve). With this scheme we wished to check, whether the dead time can be reduced by an increased driving voltage. The red/blue current trace in Fig. 5.3b evidences that the device switches ON only when a certain period of time has passed, directly providing the value of the dead time in each individual measurement. The orange histogram and the corresponding fitted Gaussian probability density function (orange line) in Fig. 5.3d illustrate the distribution of the dead times revealing $\tau_{\text{dead}} = 216 \pm 77$ ms.

Comparing the results of the two pulsing schemes we conclude that – unlike the set and reset times (see later) – the dead time does not depend strongly on the driving conditions, the set transition is blocked for a similar time period both in the unbiased case (panel a) and also when the device was continuously driven by the set voltage (panel b). Our anticipation, that the dead time could be reduced by finite bias voltage is clearly contradicted by these experiments. Furthermore, we have observed a tendency, that the dead time in a given device slightly increases by time, but this aging effect typically leads to a variation below a factor of three. According to our experience, aging is somewhat accelerated if the set voltage is applied over longer periods of time, which explains the slightly higher mean value and standard deviation of the dead time distribution in the biased case compared to the unbiased one. Based on the room temperature investigation of 29 independent devices on 6 chips, the device to device variation of the dead time spans an order of magnitude ranging from a few hundreds of milliseconds to a few seconds.

The variation of the dead time in the ambient conditions was also studied. Applying the pulsing scheme of Fig. 5.3a we determined the dead time distribution of a device operated at 300K, followed by the same measurement at 350K and at 300K again. The corresponding fitted Gaussian probability density functions are plotted in Fig. 5.3e, showing that a temperature increase of 50K induces an almost two orders of magnitude reduction in the dead time, but reducing the temperature to its initial value the dead time returns to a modestly lower value than before the heat treatment. The orders of magnitude reduction of the dead time at elevated temperatures demonstrates that a thermally activated process is concerned, whereas the modest permanent decrease by the end of the thermal cycle implies that the heat treatment somewhat reverses the above mentioned aging effect. In contrast to the strong temperature dependence, we found that the dead-time is insensitive to the ambient oxygen concentration in the entire pressure range, where the SiO_x resistive switching was achievable ($\approx 4 \cdot 10^{-6} - 5 \cdot 10^{-4}$ mbar).

These findings indicate that instead of a voltage driven mechanism a thermally activated process is responsible for the observed dead time rule, and the underlying process happens spontaneously, even at zero voltage. The relatively long dead times in our measurements imply, that slow microscopic processes are involved. According to in-situ HRTEM imaging [27] the reset transition is interpreted as a self-heating induced amorphization which destroys the conducting crystalline nanowire built up by the electric field upon the set transition. Within this picture our findings demonstrate that the as-quenched amorphous state established right after the reset pulse is not appropriate for immediate recrystallization upon a subsequent set pulse, as long as a thermally driven, self-assembling reorganization of the amorphous OFF state is incomplete. The latter presumably involves slow diffusion processes in the junction region.

We believe that the dead time is closely related to the 4-6 orders of magnitude faster backward-scan effect reported in Ref. [28]. According to our measurements, however, the dead time is a more general phenomenon, which is not activated by the backward sweep

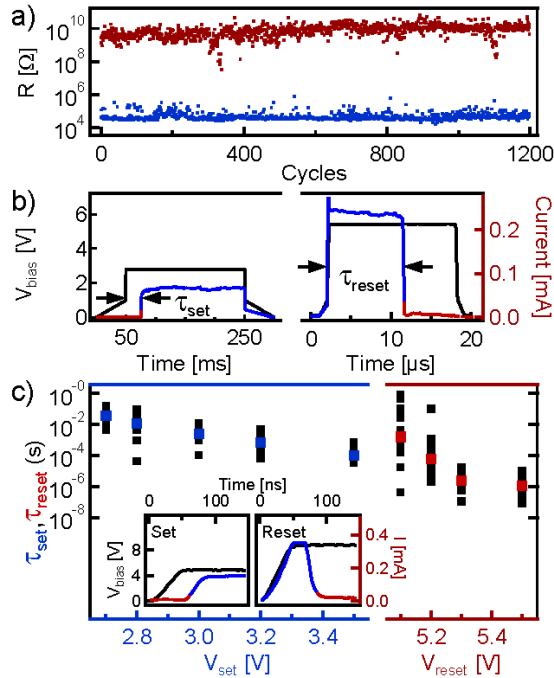


Figure 5.4: (a) Endurance test up to 10^3 switching cycles by voltage pulses of 3.5 V (set) and 9 V (reset). The displayed low bias resistance values were determined at 1 V. (b) Illustration of the time-resolved set and reset transitions. (c) Statistical analysis of the set/reset times as a function of the set/reset voltages. The mean values are highlighted in blue/red. The insets demonstrate the fastest set/reset transitions achieved at the time resolution of our pulsing setup.

itself. In our nanometer-scale devices the switching region is well defined by the narrowest cross-section of the nanogap, therefore we have to wait until this particular region rearranges properly for subsequent recrystallization. In a larger vertical device the recrystallization can occur at any segment of a much larger cross section, therefore the characteristic timescale is expected to downscale with increasing device cross section. This may explain the faster, μs timescale of the backward-scan effect. Presumably the dead time is also sensitive to the microscopic material properties of the SiO_x layer, thus it is expected to be sensitive to the pretreatment of the substrate.

5.3.2. Endurance properties and set-reset transitions

Finally, we characterize the set and reset transitions. Figure 5.4a illustrates device resistances upon a repeated set/reset pulse train similar to the scheme used for recording the bottom curve of Fig. 5.3a. The samples show excellent endurance, one can write and erase the device more than 10^3 times without any degradation. The logarithmic current scale of Fig. 5.4a demonstrates that the device exhibits a sufficiently large OFF/ON resistance ratio ($> 10^4$).

Figure 5.4b displays the device's real time response to individual set and reset pulses. The square pulses are superimposed on linearly ramped segments having positive/negative

slopes at the rising/falling edges of the pulse, which are used to determine the low bias resistance before and after the pulse. Figure 5.4c shows that both the set and the reset times change many orders of magnitude upon a modest variation of the set and reset voltages, similarly to the observations in Ref. [29]. By proper driving both the reset and set transitions could be achieved within 50 ns as illustrated in the insets of Fig. 5.4c representing the instrumental limitation of our pulsing setup.

Our time-resolved measurement also show, that the set and reset actions are not gradual transitions, but the device stays in its initial state for a certain time delay from the pulse's rising edge (see τ_{set} and τ_{reset} in Fig. 5.4b), which is followed by an abrupt switching to the final state. The resolution of the latter *switching time* is always limited by our instrumental bandwidth. This delayed action implies that both the electric field driven crystallization (set) and the voltage-induced, self-heating driven amorphization (reset) are preceded by 'hidden' microscopic processes, which do not directly affect the device resistance, yet they are prerequisites of the actual transitions. In case of the set transition, a nucleation process conditional for the crystalline conducting bridge formation is conceived. The reset transition is accompanied by similar power dissipation as the electrical breakdown of graphene ($> 8\text{ V}$ voltage at $\approx 10\text{ k}\Omega$ resistance), where local temperatures above 1000 K are reasonable. [17, 30–32] At the SiO_x reset transition this power is dissipated in an even smaller volume, though the heat is presumably conducted better towards the substrate. Based on this rough comparison, we find it reasonable to achieve similarly extreme temperatures. During the set transition more than 4 orders of magnitude smaller power is dissipated, therefore no significant selfheating is expected. We also note, that according to measurements on similarly sized nanodevices, [33, 34] and thermal models based on the classical theory of heat conduction [35–37] the thermal time constant of the active junction region is expected to be in the nanosecond range, i.e. below the duration of our shortest pulses (50 ns). Accordingly, steady state temperatures are expected to set already along the pulse edges.

5.3.3. Physical process

The resistive switching capability of SiO_x was discovered in the 1960's in silicon rich metal-insulator-metal structures. [38–40] In the recent years various types of SiO_x based resistive switches were demonstrated based on either extrinsic [41–43] or intrinsic [20, 44] mechanisms. In the former case the SiO_x merely acts as a passive matrix for metallic filament formation fueled by the electrodes while in the latter it plays an active role by forming conductive, silicon rich pathways upon biasing. The complete switching cycle is explained in terms of crystallization and amorphization of the Si along the conductive filament. The presence of Si nanocrystals (NCs) embedded in the SiO_x matrix within the active device volume was indeed confirmed by *in-situ* transmission electron microscopy studies. [18, 27, 45] Additionally, the accumulation of defect sites were also identified to contribute to filamentary resistive switching. [21, 46–49] Vertically stacked devices with SiO_x thicknesses above 10 nm show non-volatile behavior, good endurance ($>10^4$ cycles), high OFF/ON resistance ratios ($>10^5$) and short set/reset times ($<100\text{ ns}$) [23, 50], while below this layer thickness a lower yield of successful electroforming and less stable switching behavior is typically observed. [23]

5.4. Conclusion

In conclusion, we have studied SiO_x resistive switching memories confined in few nanometer wide graphene nanogaps, demonstrating the potential of electrical breakdown techniques in establishing ultrasmall ReRAM devices. Thank to the small dimensions, low voltage electroforming was achieved close to the reset voltage level. As the conducting pathway formation is driven by the electric field, [23, 27, 51] we anticipate that the active volume of the device is confined to the nanometer scale gap region, where the electric field is the largest.

We have demonstrated that the device operation is governed by complex microscopic processes involving multiple physical timescales. The set/reset transitions do not follow a common gradual crossover, rather the set/reset times are regarded as a *time delay*, while no resistance change occurs, followed by a sudden crossover taking place within a short *switching time*, the latter falling below our experimental resolution (< 50 ns). Both the set and the reset times can be tuned over many orders of magnitude by the modest linear variation of the set/reset voltages, thus both transitions are classified as voltage activated processes. A further fundamental timescale, the *dead time* is also identified as an essential ingredient to intrinsic resistive switching in SiO_x . If the device is driven slowly compared to the dead time, a clear unipolar operation is observed, where the OFF state is inaccessible at zero bias. However, at faster driving the dead time rule temporarily blocks the device in the OFF state after the reset transition, and therefore both the ON and OFF states can be restored at zero bias by the proper choice of unipolar pulse sequences. We attribute the dead time to a slow reorganization of the as-quenched amorphous OFF state, which is required before the repeated recrystallization.

Studying the response to various driving sequences, we have found that – unlike the set and reset times – the dead time does not arise from a voltage driven mechanism, it is rather a spontaneous process assisted by the ambient temperature. The fundamental technological impact of the dead time rule lies in the fact that it enables the programming of SiO_x phase change memory devices by unipolar voltage pulses, nonvolatile two-state information storage at zero bias and low-voltage read-out at the same time.

5.5. Outlook

Despite, the technological relevance of the graphene- SiO_x switch, it represents a new challenge towards the development of graphene-based molecular electrodes. Presence of defects at SiO_x the oxide surface can interfere with the signature of molecules. Few strategies can be employed to counter this issue. The use of SiN substrates is a possibility or the passivation of the gap region.

Contributions This chapter has been published Nanoscale, 2017,9, 17312-17317. The authors are Laszlo Posa, Maria El Abbassi, Peter Makk, Botond Santa, Cornelia Nef, Miklos Csontos, Michel Calame and Andras Halbritter. M.E made the samples. L.P performed the measurements and the analysis. All the authors contributed to the data analysis and the manuscript writing.

5

Bibliography

- [1] Geoffrey W. Burr, Robert M. Shelby, Abu Sebastian, Sangbum Kim, Seyoung Kim, Severin Sidler, Kumar Virwani, Masatoshi Ishii, Pritish Narayanan, Alessandro Fumarola, Lucas L. Sanches, Irem Boybat, Manuel Le Gallo, Kibong Moon, Jiyoo Woo, Hyunsang Hwang, and Yusuf Leblebici. Neuromorphic computing using non-volatile memory. *Advances in Physics: X*, 2(1):89–124, 2017.
- [2] R. Waser and M. Aono. Nanoionics-based resistive switching memories. *Nature Materials*, 6:833–840, 2007.
- [3] D. B. Strukov and R. S. Williams. Exponential ionic drift: fast switching and low volatility of thin-film memristors. *Applied Physics A*, 94:515–519, 2008.
- [4] J. Borghetti, G. S. Snider, P. J. Kuekes, J. J. Yang, D. R. Stewart, and R. S. Williams. Memristive switches enable stateful logic operations via material implication. *Nature*, 464(8):873–876, 2010.
- [5] J. J. Yang, D. B. Strukov, and D. R. Stewart. Memristive devices for computing. *Nature Nanotechnology*, 8(1):13–24, 2013.
- [6] Tz yi Liu, Tian Hong Yan, Roy Scheuerlein, Yingchang Chen, Jeffrey KoonYee Lee, Gopinath Balakrishnan, Gordon Yee, Henry Zhang, Alex Yap, Jingwen Ouyang, Takahiko Sasaki, Ali Al-Shamma, Chinyu Chen, Mayank Gupta, Greg Hilton, Achal Kathuria, Vincent Lai, Masahide Matsumoto, Anurag Nigam, Anil Pai, Jayesh Pakhale, Chang Hua Siau, Xiaoxia Wu, Yibo Yin, Nicolas Nagel, Yoichiro Tanaka, Masaaki Higashitani, Tim Minvielle, Chandu Gorla, Takayuki Tsukamoto, Takeshi Yamaguchi, Mutsumi Okajima, Takayuki Okamura, Satoru Takase, Hirofumi Inoue, and Luca Fasoli. A 130.7-mm² 2-layer 32-gb reram memory device in 24-nm technology. *IEEE Journal of Solid-State Circuits*, 49(1):140–153, 2014.
- [7] M. Prezioso, F. Merrikh-Bayat, B. D. Hoskins, G. C. Adam, K. K. Likharev, and D. B. Strukov. Training and operation of an integrated neuromorphic network based on metal-oxide memristors. *Nature*, 521:61–64, 2015.
- [8] B. Chakrabarti, M. A. Lastras-Montaño, G. Adam, M. Prezioso, B. Hoskins, K.-T. Cheng, and D. B. Strukov. A multiply-add engine with monolithically integrated 3d memristor crossbar/cmos hybrid circuit. *Scientific Reports*, 7:42429, 2017.
- [9] Gina C. Adam, Brian D. Hoskins, Mirko Prezioso, Farnood Merrikh-Bayat, Bhaswar Chakrabarti, and Dmitri B. Strukov. 3-d memristor crossbars for analog and neuromorphic computing applications. *IEEE Transactions on Electron Devices*, 64(1):312–318, 2017.

- [10] Stephan Menzel, Ulrich Böttger, Martin Wimmer, and Martin Salinga. Physics of the switching kinetics in resistive memories. *Advanced Functional Materials*, 25:6306–6325, 2015.
- [11] A. Gubicza, M. Csontos, A. Halbritter, and G. Mihály. Non-exponential resistive switching in ag_2s memristors: a key to nanometer-scale non-volatile memory devices. *Nanoscale*, 7:4394–4399, 2015.
- [12] S. H. Jo, T. Chang, I. Ebong, B. B. Bhadviya, P. Mazumder, and W. Lu. Nanoscale memristor device as synapse in neuromorphic systems. *Nano Letters*, 10(4):1297–1301, 2010.
- [13] T. Ohno, T. Hasegawa, T. Tsuruoka, K. Terabe, J. K. Gimzewski, and M. Aono. Short-term plasticity and long-term potentiation mimicked in single inorganic synapses. *Nature Materials*, 10(8):591–595, 2011.
- [14] R. Waser, R. Dittmann, G. Staikov, and K. Szot. Redox-based resistive switching memories - nanoionic mechanisms, prospects, and challenges. *Advanced Materials*, 21(25-26):2632–2663, 2009.
- [15] Jun Yao, Jian Lin, Yanhua Dai, Gedeng Ruan, Zheng Yan, Lei Li, Lin Zhong, Douglas Natelson, and James M. Tour. Highly transparent nonvolatile resistive memory devices from silicon oxide and graphene. *Nat Commun*, 3:1101, Oct 2012.
- [16] Congli He, Zhiwen Shi, Lianchang Zhang, Wei Yang, Rong Yang, Dongxia Shi, and Guangyu Zhang. Multilevel resistive switching in planar graphene/sio2 nanogap structures. *ACS Nano*, 6(5):4214–4221, 2012.
- [17] Albert D. Liao, Paulo T. Araujo, Runjie Xu, and Mildred S. Dresselhaus. Carbon nanotube network-silicon oxide non-volatile switches. *Nature Communications*, 5:5673, Dec 2014.
- [18] Jun Yao, Zhengzong Sun, Lin Zhong, Douglas Natelson, and James M. Tour. Resistive switches and memories from silicon oxide. *Nano Letters*, 10(10):4105–4110, 2010.
- [19] Yao-Feng Chang, Li Ji, Zhuo-Jie Wu, Fei Zhou, Yanzhen Wang, Fei Xue, Burt Fowler, Edward T. Yu, Paul S. Ho, and Jack C. Lee. Oxygen-induced bi-modal failure phenomenon in siox-based resistive switching memory. *Applied Physics Letters*, 103(3):033521, 2013.
- [20] Jun Yao, Lin Zhong, Zengxing Zhang, Tao He, Zhong Jin, Patrick J. Wheeler, Douglas Natelson, and James M. Tour. Resistive switching in nanogap systems on sio2 substrates. *Small*, 5(24):2910–2915, 2009.
- [21] Burt W. Fowler, Yao-Feng Chang, Fei Zhou, Yanzhen Wang, Pai-Yu Chen, Fei Xue, Yen-Ting Chen, Brad Bringham, Scott Pozder, and Jack C. Lee. Electroforming and resistive switching in silicon dioxide resistive memory devices. *RSC Adv.*, 5:21215–21236, 2015.
- [22] Yanzhen Wang, Burt Fowler, Yen-Ting Chen, Fei Xue, Fei Zhou, Yao-Feng Chang, and Jack C. Lee. Effect of hydrogen/deuterium incorporation on electroforming voltage of siox resistive random access memory. *Applied Physics Letters*, 101(18), 2012.

- [23] Yao-Feng Chang, Pai-Yu Chen, Burt Fowler, Yen-Ting Chen, Fei Xue, Yanzhen Wang, Fei Zhou, and Jack C. Lee. Understanding the resistive switching characteristics and mechanism in active siox-based resistive switching memory. *Journal of Applied Physics*, 112(12), 2012.
- [24] Syed Ghazi Sarwat, Pascal Gehring, Gerardo Rodriguez Hernandez, Jamie H. Warner, G. Andrew D. Briggs, Jan A. Mol, and Harish Bhaskaran. Scaling limits of graphene nanoelectrodes. *Nano Letters*, 17(6):3688–3693, 2017.
- [25] Hang Zhang, Wenzhong Bao, Zeng Zhao, Jhao-Wun Huang, Brian Standley, Gang Liu, Fenglin Wang, Phillip Kratz, Lei Jing, Marc Bockrath, and Chun Ning Lau. Visualizing electrical breakdown and on/off states in electrically switchable suspended graphene break junctions. *Nano Letters*, 12(4):1772–1775, 2012.
- [26] Brian Standley, Wenzhong Bao, Hang Zhang, Jehoshua Bruck, Chun Ning Lau, and Marc Bockrath. Graphene-based atomic-scale switches. *Nano Letters*, 8(10):3345–3349, 2008.
- [27] Jun Yao, Lin Zhong, Douglas Natelson, and James M. Tour. In situ imaging of the conducting filament in a silicon oxide resistive switch. *Scientific Reports*, 2:242, Jan 2012.
- [28] Yao-Feng Chang, Li Ji, Yanzhen Wang, Pai-Yu Chen, Fei Zhou, Fei Xue, Burt Fowler, Edward T. Yu, and Jack C. Lee. Investigation of edge- and bulk-related resistive switching behaviors and backward-scan effects in siox-based resistive switching memory. *Applied Physics Letters*, 103(19), 2013.
- [29] Yao-Feng Chang, Burt Fowler, Ying-Chen Chen, Fei Zhou, Chih-Hung Pan, Ting-Chang Chang, and Jack C. Lee. Demonstration of synaptic behaviors and resistive switching characterizations by proton exchange reactions in silicon oxide. *Scientific Reports*, 6:21268 EP –, Feb 2016.
- [30] Young Duck Kim, Hakseong Kim, Yujin Cho, Ji Hoon Ryoo, Cheol-Hwan Park, Pilkwang Kim, Yong Seung Kim, Sunwoo Lee, Yilei Li, Seung-Nam Park, Yong Shim Yoo, Duhee Yoon, Vincent E. Dorgan, Eric Pop, Tony F. Heinz, James Hone, Seung-Hyun Chun, Hyeonsik Cheong, Sang Wook Lee, Myung-Ho Bae, and Yun Daniel Park. Bright visible light emission from graphene. *Nat Nano*, 10(8):676–681, Aug 2015.
- [31] Stéphane Berciaud, Melinda Y. Han, Kin Fai Mak, Louis E. Brus, Philip Kim, and Tony F. Heinz. Electron and optical phonon temperatures in electrically biased graphene. *Phys. Rev. Lett.*, 104:227401, Jun 2010.
- [32] Benedikt Westenfelder, Jannik C. Meyer, Johannes Biskupek, Simon Kurasch, Ferdinand Scholz, Carl E. Krill, and Ute Kaiser. Transformations of carbon adsorbates on graphene substrates under extreme heat. *Nano Letters*, 11(12):5123–5127, 2011.
- [33] F. Stellari, K. A. Jenkins, A. J. Weger, B. P. Linder, and P. Song. Self-heating measurement of 14-nm finfet soi transistors using 2-d time-resolved emission. *IEEE Transactions on Electron Devices*, 63(5):2016–2022, May 2016.

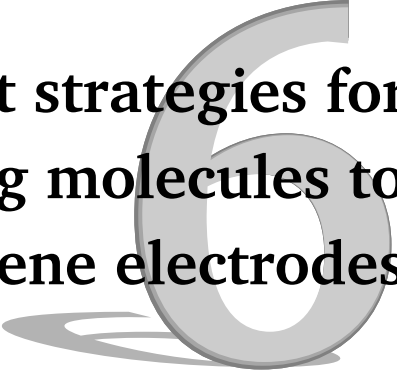
- [34] C. Prasad, S. Ramey, and L. Jiang. Self-heating in advanced cmos technologies. In *2017 IEEE International Reliability Physics Symposium (IRPS)*, pages 6A-4.1-6A-4.7, April 2017.
- [35] Daolin Cai, Zhitang Song, Houpeng Chen, and Xiaogang Chen. Temperature model for ge2sb2te5 phase change memory in electrical memory device. *Solid-State Electronics*, 56(1):13 – 17, 2011.
- [36] J. P. Reifenberg, D. L. Kencke, and K. E. Goodson. The impact of thermal boundary resistance in phase-change memory devices. *IEEE Electron Device Letters*, 29(10):1112–1114, Oct 2008.
- [37] C. Xu, S. K. Kolluri, K. Endo, and K. Banerjee. Analytical thermal model for self-heating in advanced finfet devices with implications for design and reliability. *IEEE Transactions on Computer-Aided Design of Integrated Circuits and Systems*, 32(7):1045–1058, July 2013.
- [38] T. W. Hickmott. Low-frequency negative resistance in thin anodic oxide films. *Journal of Applied Physics*, 33(9):2669–2682, 1962.
- [39] J. G. Simmons and R. R. Verderber. New conduction and reversible memory phenomena in thin insulating films. *Proceedings of the Royal Society of London A: Mathematical, Physical and Engineering Sciences*, 301(1464):77–102, 1967.
- [40] G Dearnaley, A M Stoneham, and D V Morgan. Electrical phenomena in amorphous oxide films. *Reports on Progress in Physics*, 33(3):1129, 1970.
- [41] Sung Hyun Jo and Wei Lu. Cmos compatible nanoscale nonvolatile resistance switching memory. *Nano Letters*, 8(2):392–397, 2008.
- [42] G. S. Tang, F. Zeng, C. Chen, H. Y. Liu, S. Gao, S. Z. Li, C. Song, G. Y. Wang, and F. Pan. Resistive switching with self-rectifying behavior in cu/siox/si structure fabricated by plasma-oxidation. *Journal of Applied Physics*, 113(24), 2013.
- [43] Christina Schindler, Sarath Chandran Puthen Thermadam, Rainer Waser, and Michael N. Kozicki. Bipolar and unipolar resistive switching in cu-doped sio2. *IEEE Transactions on Electron Devices*, 54(10):2762–2768, 10 2007.
- [44] Jun Yao, Lin Zhong, Douglas Natelson, and James M. Tour. Etching-dependent reproducible memory switching in vertical sio2 structures. *Applied Physics Letters*, 93(25), 2008.
- [45] Congli He, Jiafang Li, Xing Wu, Peng Chen, Jing Zhao, Kuibo Yin, Meng Cheng, Wei Yang, Guibai Xie, Duoming Wang, Donghua Liu, Rong Yang, Dongxia Shi, Zhiyuan Li, Litao Sun, and Guangyu Zhang. Tunable electroluminescence in planar graphene/sio2 memristors. *Advanced Materials*, 25(39):5593–5598, 2013.
- [46] Adnan Mehonic, Sébastien Cuffe, Maciej Wojdak, Stephen Hudziak, Olivier Jambois, Christophe Labbé, Blas Garrido, Richard Rizk, and Anthony J. Kenyon. Resistive switching in silicon suboxide films. *Journal of Applied Physics*, 111(7), 2012.

- [47] Adnan Mehonic, Sébastien Cueff, Maciej Wojdak, Stephen Hudziak, Christophe Labbé, Richard Rizk, and Anthony J Kenyon. Electrically tailored resistance switching in silicon oxide. *Nanotechnology*, 23(45):455201, 2012.
- [48] A. Mehonic, A. Vrajitoarea, S. Cueff, S. Hudziak, H. Howe, C. Labbé, R. Rizk, M. Pepper, and A. J. Kenyon. Quantum conductance in silicon oxide resistive memory devices. *Scientific Reports*, 3:2708 EP –, Sep 2013.
- [49] Yuefei Wang, Xinye Qian, Kunji Chen, Zhonghui Fang, Wei Li, and Jun Xu. Resistive switching mechanism in silicon highly rich siox films based on silicon dangling bonds percolation model. *Applied Physics Letters*, 102(4), 2013.
- [50] Jun Yao, Lin Zhong, Douglas Natelson, and James M. Tour. Intrinsic resistive switching and memory effects in silicon oxide. *Applied Physics A*, 102(4):835–839, 2011.
- [51] Jin Jang, Jae Young Oh, Sung Ki Kim, Young Jin Choi, Soo Young Yoon, and Chae Ok Kim. Electric-field-enhanced crystallization of amorphous silicon. *Nature*, 395(6701):481–483, Oct 1998.

Part III

Molecular junctions

Different strategies for anchoring molecules to graphene electrodes



Electron and phonon transport through an electrode-molecule-electrode junction is very sensitive to the interface between the molecule and the electrode material. Understanding and developing new strategies for attaching molecules is therefore crucial for device applications. Graphene electrodes offer a very interesting platform to test different binding possibilities like strong C-C covalent bonds or weaker $\pi-\pi$ interaction. In this chapter, we list the different possibilities that were investigated during this thesis for contacting molecules in a reliable way using graphene nanogaps.

6.1. Introduction

To attach molecules to graphene electrodes, several binding mechanisms were investigated both experimentally and theoretically. Jia et al. [1] demonstrated the operation of a stable and reversible photoswitch by covalently binding a diarylethene molecule to the graphene electrodes. In this study, gaps were formed by reactive etching of graphene using an oxygen plasma. As a result, the gap edges are oxygen terminated acting as possible reaction sites for the covalent bond formation. Similarly, assuming oxidized graphene edges, but this time with EB junctions, Xu et al. [2] characterized a short benzene molecule connected to the electrodes using an amine group and measured single-electron transistor behavior. However, in this case, the yield of junction formation was smaller than 20 %. This low yield can be due to the lack of control over the edge termination of the graphene electrodes using the EB technique. Moreover, due to the strong interaction with the electrodes, it has been predicted theoretically that charge transport will be highly sensitive to the electrode shape [3].

$\pi - \pi$ interaction between the molecule and the graphene electrode could offer an alternative to direct covalent binding. This approach has the advantage that it does not impose any requirements on the edge termination of the gap; it only requires the molecule to contain π -conjugated groups. Furthermore, the weaker electronics coupling allows for a better decoupling of the properties of the molecules from the ones of the electrode. Transport across the junction is therefore expected to be less sensitive to the electrode shape. This approach was verified by Mol et al. [4], who used tetrabenzofluorene anchors to connect zinc-porphyrin molecules. They observed multiple redox states at room temperature and single-electron charging energies insensitive to the molecular junction. The drawback of this method is that the weak interaction with the contacts also leads to a limited mechanical stability of the junctions at room temperature [5].

For our graphene EB junctions, no control of the edge termination and electrode geometry is possible so far, making weak $\pi - \pi$ interaction a more suitable approach to achieve reproducible electronic features. The main focus for our graphene-based molecular junctions is to achieve, next to electronic stability, a high mechanical stability.

6.2. $\pi - \pi$ interaction

The first molecule that was measured is a cobalt complex with pyrene anchors (see Figure 6.1 a) for the chemical structure). The molecule was synthesized by Shlomo Yitzchaik et al., from the Hebrew university of Jerusalem. Figure 6.1 b) shows a stability diagram measured on a junction after deposition, with the corresponding IV curves at different gate voltage in Figure 6.1 c). An increase of current of more than a factor 500 is measured. Currents before deposition are typically lower than 1 nA and in this case after deposition we reach 500 nA. However, as we can see in Figure 6.1 b), in the negative gate region the currents decrease drastically. IV curves were recorded from positive gate voltage to negative ones. In this case, around -20V, the current decreases by a factor more than 100. We were not able to reproduce the measurements of Figure 6.1 b) because the currents remained small after that ramp. We attribute this effect to the sliding of the molecules at the surface of the graphene which is possible at room temperature because of the weak nature of $\pi - \pi$ interaction [5].

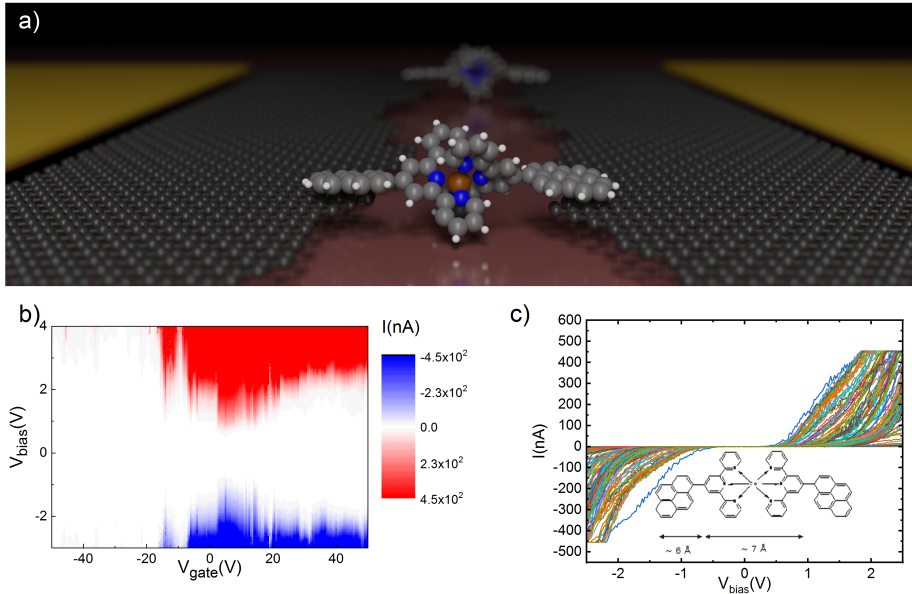


Figure 6.1: Pyrene cobalt complex measurements a) Drawing of a molecule inside a graphene gap. b and c) Electrical measurements at room temperature: b) presents the stability diagram recorded for a device and c) presents the IV curves recorded at different gate voltage values extracted from the stability diagram in b).

6.2.1. Covalent binding to the substrate combined with $\pi - \pi$ interaction to the electrode

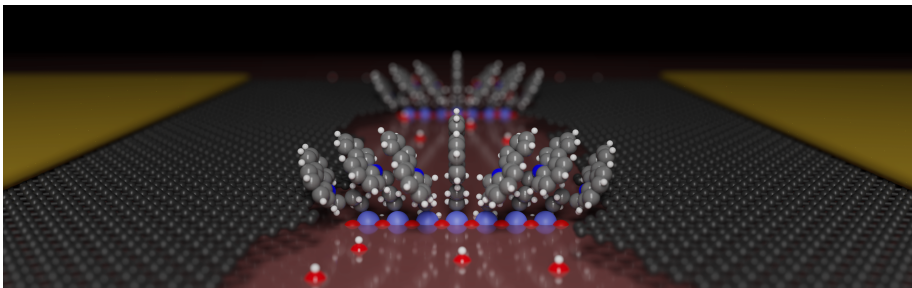


Figure 6.2: Silanization combined with $\pi - \pi$ stacking to anchor the molecules. Schematic of the ground-state relaxed geometry of seven 3-carbazolylpropyltrimethoxysilane molecules in series bridging a graphene nanogap. The nanogaps are formed using the electrical breakdown technique. The molecules are attached to the substrate via silanization of the surface. OH groups are represented with red and white atoms on the SiO_2 surface. The color difference between the carbon atoms of the molecule and those of the graphene is for clarity reasons only.

To overcome the mechanical stability problem faced in the previous section but preserve the electronic advantages of the weak electronic binding, we have decided to decouple the mechanical anchoring of the molecule from the electronic charge injection barrier. The molecule is covalently anchored to the substrate using silanization for mechanical robustness,

rather than to graphene electrodes, and electronically coupled to the graphene electrode via a π conjugated group (see Figure.6.2), with a N-carbazole headgroup). Figure.6.2 shows a drawing of the molecular junction consisting of a layer of molecules binding to the oxide. A detailed study of these molecules is presented in the following chapters.

6.2.2. Graphene Nanoribbons

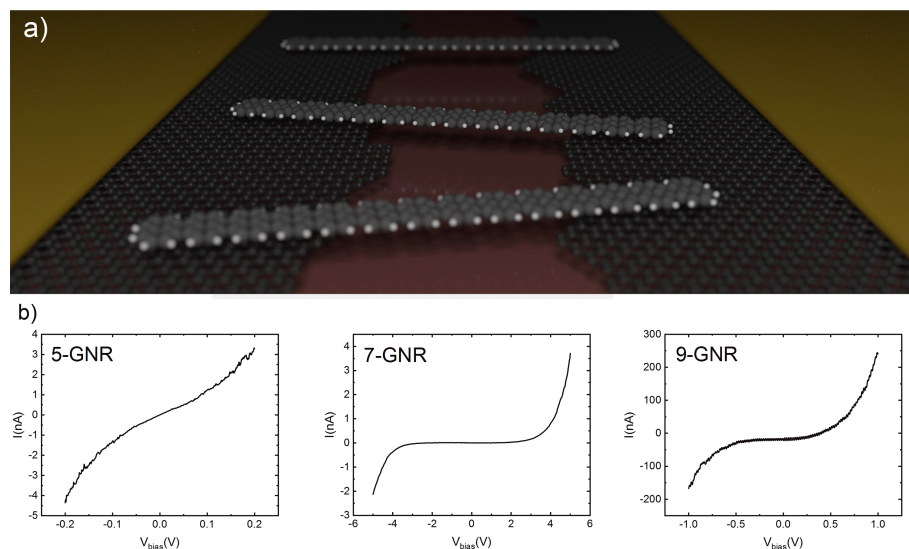


Figure 6.3: Room temperature of armchair graphene nanoribbons a) Drawing of GNRs bridging a graphene nanogap. b) IV curves recorded after transfer on armchair graphene nanoribbons with three different widths: 5, 7 and 9 atoms.

Another option to stabilize the junctions is to use larger π conjugated anchor groups. This possibility was explored using graphene nanoribbons (GNR). Their tunable electronic and magnetic properties, combined with the recent advances in the bottom-up synthesis of these objects [6], make them very interesting for electronic device applications. The most studied GNR have armchair edges, and are divided into three families according to their width, i.e., $N_a = 3p$, $N_a = 3p + 1$, and $N_a = 3p + 2$, where N_a is the number of carbon atoms across the ribbon width and p an integer number. Each of these families possess specific bandgaps and level structure [6–9]. 5 atoms wide GNRs are predicted to be metallic with the smallest bandgap of the armchair families around 100 meV on Au surface [9]. GNRs from the two other families possess a larger bandgap, resp, 2.5 eV for the 7 atoms wide ribbons [7, 10] and 1.5-2eV for the 9 atoms wide ones [8]. So far, all measurements to investigate their level structure were performed either with STM on Au surface or with metallic contacts. In our case, we studied three different GNRs each, from a different family (5,7 and 9 atoms wide GNRs). Figure.6.3 a) presents a drawing of a 5AGNR bridging a graphene gap.

Figure 6.3 b) shows typical IV curves measured for the three GNRs. Whereas the 5 GNR shows an approximately linear IV curve around 0 V bias voltage, the IV curves from the 2 other ribbons show a blocking region where no current is going through the junction for low

bias voltages.

The measurements show that the 7-GNR exhibits a larger blocking region than the 9-GNR and overall smaller currents. In general, the size of the blocking region is dependent on the bandgap of the ribbons and their alignment with the Fermi energy of the electrodes. The difference in blocking region size observed for the three ribbons is in a good agreement with theoretical predictions in the literature. In chapter 9, we will go into more detail in the charge transport mechanism of the 5 AGNRs.

6.3. Conclusion

In this chapter, we briefly listed the different molecules investigated during this thesis. Details of the electrical characterization of the various approaches are given in the following chapters.

Contributions All the schematic pictures were made by Mickael Perrin with Blender. The PtP-Co and the carbazole-silane molecules were provided by Shlomo Yitzchaik. The graphene nanoribbons are grown at EMPA by Gabriela Borin Barin from Roman Fasel group.

Bibliography

- [1] Chuancheng Jia, Agostino Migliore, Na Xin, Shaoyun Huang, Jinying Wang, Qi Yang, Shuopei Wang, Hongliang Chen, Duoming Wang, Boyong Feng, Zhirong Liu, Guangyu Zhang, Da-Hui Qu, He Tian, Mark A. Ratner, H. Q. Xu, Abraham Nitzan, and Xuefeng Guo. Covalently bonded single-molecule junctions with stable and reversible photoswitched conductivity. *Science*, 352(6292):1443–1445, 2016.
- [2] Qizhi Xu, Giovanni Scuri, Carly Mathewson, Philip Kim, Colin Nuckolls, and Delphine Bouilly. Single electron transistor with single aromatic ring molecule covalently connected to graphene nanogaps. *Nano letters*, 17(9):5335–5341, 2017.
- [3] Hatef Sadeghi, Sara Sangtarash, and Colin Lambert. Robust molecular anchoring to graphene electrodes. *Nano Letters*, 17(8):4611–4618, 2017.
- [4] Jan A Mol, Chit Siong Lau, Wilfred JM Lewis, Hatef Sadeghi, Cecile Roche, Arjen Cnossen, Jamie H Warner, Colin J Lambert, Harry L Anderson, and G Andrew D Briggs. Graphene-porphyrin single-molecule transistors. *Nanoscale*, 7(31):13181–13185, 2015.
- [5] Suzhi Li, Qunyang Li, Robert W Carpick, Peter Gumbsch, Xin Z Liu, Xiangdong Ding, Jun Sun, and Ju Li. The evolving quality of frictional contact with graphene. *Nature*, 539(7630):541–545, 2016.
- [6] Jinming Cai, Pascal Ruffieux, Rached Jaafar, Marco Bieri, Thomas Braun, Stephan Blankenburg, Matthias Muoth, Ari P Seitsonen, Moussa Saleh, Xinliang Feng, Klaus Mullen and Roman Fasel Atomically precise bottom-up fabrication of graphene nanoribbons *Nature*, 466: 470–473,2010.
- [7] Pascal Ruffieux, Jinming Cai, Nicholas C. Plumb, Luc Patthey, Deborah Prezzi, Andrea Ferretti, Elisa Molinari, Xinliang Feng, Klaus Müllen, Carlo A. Pignedoli, and Roman Fasel. Electronic Structure of Atomically Precise Graphene Nanoribbons *ACS Nano*, 6 (8):6930–6935, 2012.
- [8] Juan Pablo Llinas, Andrew Fairbrother, Gabriela Borin Barin, Wu Shi, Kyunghoon Lee, Shuang Wu, Byung Yong Choi, Rohit Braganza, Jordan Lear, Nicholas Kau, Wonwoo Choi, Chen Chen, Zahra Pedramrazi, Tim Dumslaff, Akimitsu Narita, Xinliang Feng, Klaus Mullen, Felix Fischer, Alex Zettl, Pascal Ruffieux, Eli Yablonovitch, Michael Crommie, Roman Fasel and Jeffrey Bokor Short-channel field-effect transistors with 9-atom and 13-atom wide graphene nanoribbons *Nature Communications* 8: 633, 2017.
- [9] Amina Kimouche, Mikko M. Ervasti, Robert Drost, Simo Halonen, Ari Harju, Pekka M. Joensuu, Jani Sainio and Peter Liljeroth. Ultra-narrow metallic armchair graphene nanoribbons *Nature Communications* 6: 10177, 2015.

- [10] Yen-Chia Chen, Dimas G. de Oteyza, Zahra Pedramrazi, Chen Chen, Felix R. Fischer, and Michael F. Crommie. Tuning the Band Gap of Graphene Nanoribbons Synthesized from Molecular Precursors *ACS Nano*,7 (7): 6123–6128, 2013.

Silanization as a robust way to contact molecules



In this chapter, we describe a statistically robust graphene-based multi-molecule junction, achieved by anchoring molecules directly to the substrate using silanization, rather than to graphene electrodes. This approach yields molecular junctions with robust mechanical properties, and allows for decoupling of the mechanical anchoring from the electronic charge injection barrier. Using a vector-based clustering method, we identify various transport characteristics and demonstrate that our novel contacting method leads to a statistically reproducible electronic signature throughout multiple samples.

Introduction

As discussed in the previous chapters, to realise reliable graphene-based junctions, several issues still need to be addressed. First, graphene-based junctions have been reported to exhibit signatures similar to these of molecules, with gate-dependent resonance features, such as Coulomb blockade [2, 10], quantum interference [3] and Fabry-Perrot resonances [12]. Secondly, connecting molecules to the graphene remains very challenging: $\pi - \pi$ stacking is believed to be the most suitable strategy [3] offering advantages such as a high thermoelectric efficiency, but leads to mechanically unstable junctions [7]. Molecules have also been bonded covalently to graphene yielding mechanically stable junctions [11]. However, transport through strongly coupled molecules is expected to be heavily influenced by electrode geometry, edge termination and crystallographic structure. These lead to a large variability in the shape of the current-voltage characteristics [3]. Third, the silicon dioxide substrate has been reported to yield feature-rich charge-transport characteristics, primarily due to switching within the oxide [9]. Furthermore, junction-to-junction variability remains high for the above-mentioned methods of anchoring molecules to graphene [10, 11], leading to poor devices statistics.

7 In this study, we report on the realization of statistically robust graphene-based molecular devices which address several key challenges in the field. This is achieved by anchoring molecules directly to the substrate using silanization, rather than to the graphene electrodes. This approach yields electrical properties that are statistically reproducible, and allows for independent tuning of the mechanical and electronic properties of the junction. Using a vector-based clustering method [12], we identify various transport characteristics and demonstrate that our novel contacting method is statistically robust throughout multiple samples.

7.1. Molecular structures and deposition

Anchoring of the molecules to the substrate occurred via silanization. This process is commonly used to cover surfaces with organofunctional molecules [1], and consists of the deposition of alkoxy silane molecules that react with hydroxyl groups on the silicon dioxide surface to form a covalent Si-O-Si bond. A schematic illustration of the device after silanization is presented in Fig.7.1.a. This approach offers two advantages. First, the molecules are bound to the substrate, rather than to the graphene, thereby avoiding uncontrolled edge termination and mechanically unstable $\pi - \pi$ stacking. The process passivates the silicon surface, thereby reducing unwanted switching effects [9].

The two investigated molecules structures are shown in Fig. 7.1b, contain a silane anchoring group, an alkane spacer and a head group. We choose two head groups, an aromatic N-carbazole and a methyl-terminated compound as a reference. In the following, the two molecules are referred as N-carbazole and the reference molecule, respectively. The aromatic head groups are expected to form $\pi - \pi$ stacked structures (Fig. 7.1a) which are more conductive than the reference molecule in which no delocalised π -system is formed. Density functional theory calculations (DFT) calculations in Fig.7.1.c show that for the

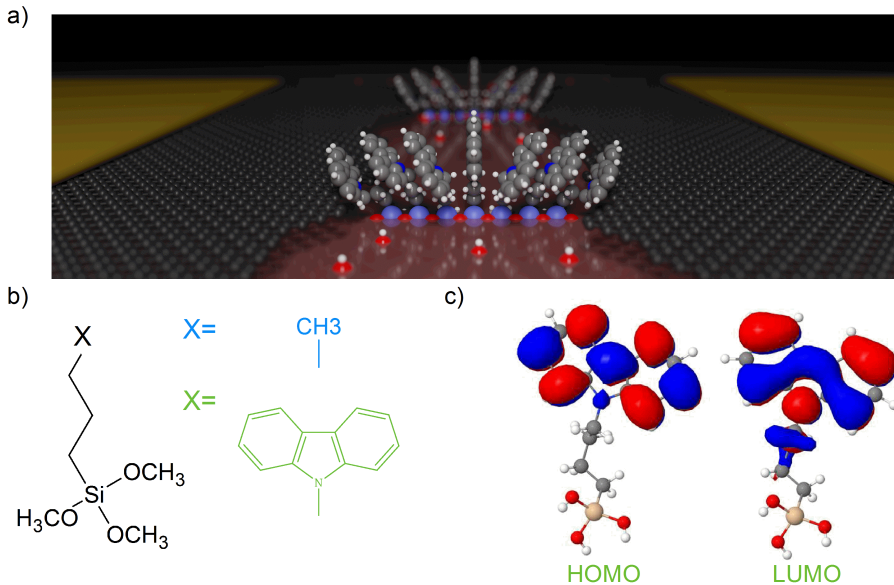


Figure 7.1: Molecular junction geometry. a) Schematic of the ground-state relaxed geometry of seven 3-carbazolylpropyltrimethoxysilane molecules in series bridging a graphene nanogap. The nanogaps are formed using the electrical breakdown technique. The molecules are attached to the substrate via silanization of the surface. OH groups are represented with red and white atoms on the SiO_2 surface. The color difference between the carbon atoms of the molecule and those of the graphene is for clarity reasons only. b) Chemical structure of the measured molecules: Both molecules have a silane group for the functionalization of the surface and an alkane chain to decouple the aromatic group X from the substrate. The aromatic group consists of either a CH_3 group or a N-carbazole group. c) Isosurfaces of the wavefunctions of the HOMO and LUMO of the molecule with the N-carbazole group using density functional theory (see methods for details).

N-carbazole molecule, the wave function of both frontier orbitals (the highest occupied molecular orbital (HOMO) and the lowest unoccupied molecular orbital (LUMO)) are mostly localized on the head group, indicating that charge transport is mainly mediated by the head group. Moreover, richer transport characteristics are expected due to the $\pi - \pi$ interaction between the head groups. Different arrangement will lead to distincts IV curves.

The molecular deposition was performed by immersion of the samples into a dry toluene solution containing the molecules of interest. In order to promote the silanization process, the solution was heated to 80°C and the sample submerged for 20 hours. After deposition, devices were rinsed with chloroform, acetone and finally isopropanol. We note that no treatment of the substrate to initiate a higher density of hydroxyl groups can be performed due to the presence of the graphene.

7.2. Measurements

Typical room-temperature current-voltage (IV) characteristics before and after deposition are presented for both molecules in the left panel of Figure. 7.2. For the reference molecule, we observe a tunneling current which is on average significantly smaller than before deposition.

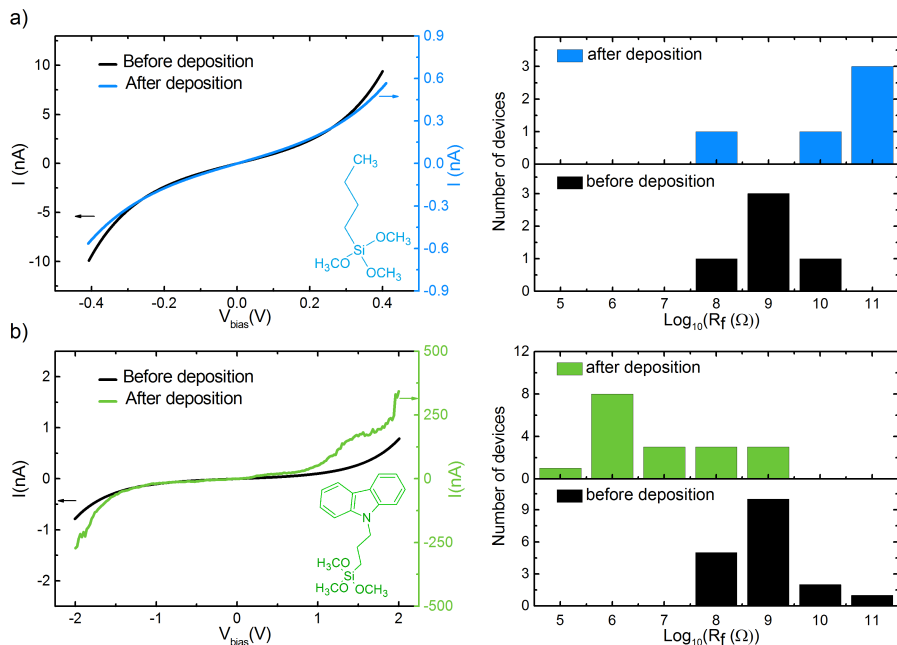


Figure 7.2: Comparison of the electrical measurements and device statistics before and after molecular deposition. The left panel presents current-voltage (IV) characteristics recorded on devices exposed to (a) the reference molecule and (b) the N-carbazole molecule. The right panel shows the statistics of the resistance before and after deposition. 5 devices were measured for the reference molecule and 18 for the carbazole molecule. Devices with a resistance lower than $100 \text{ M}\Omega$ after EB were not considered.

In fact, in the right panel of Figure 7.2.a, the histogram shows that the resistance of the devices before deposition is typically higher after deposition. This may be attributed to the cleaning effect that solvents such as toluene or chloroform have on the junctions, leading to a systematic increase in their resistance. In contrast to the tunneling curves observed for the reference molecule, the IV's observed for the N-carbazole molecule exhibit step-like features and modulations in the current. Moreover, an increase of conductance of up to two orders of magnitude was systematically observed after deposition. The current for the carbazole molecule is about three orders of magnitude larger than the reference molecule.

7.3. DFT calculations

To investigate charge transport through these graphene/molecule/graphene junctions, we calculated the transmission probability $T(E)$ of electrons with energy E passing through the molecules from one graphene electrode to another. We obtain the material specific mean-field Hamiltonian from the SIESTA implementation of the density functional theory [14] combined with the Gollum implementation of the non-equilibrium Green's function method to calculate $T(E)$ [15] (see computational method). The conductance G was calculated for different Fermi energies and temperatures using the Landauer formula: $G = G_0 \int dE T(E) (-df/dE)$

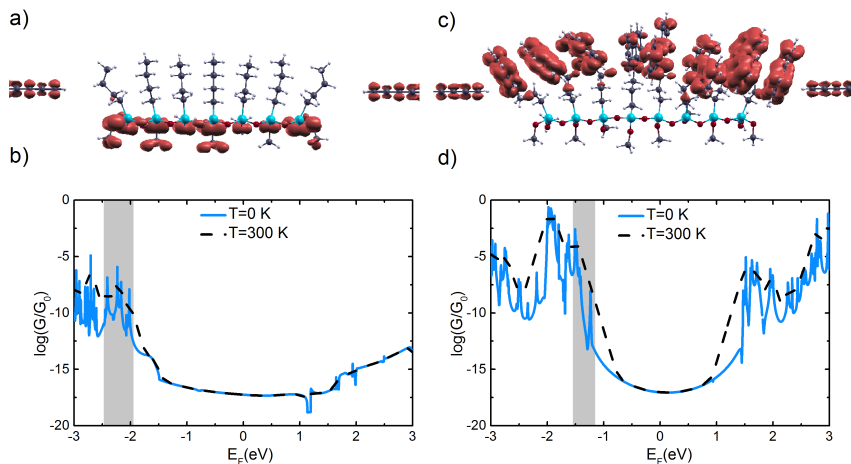


Figure 7.3: Transport through graphene/molecule/graphene junctions, with and without the N-carbazole group. (a,c) Local density of states (*LDOS*) plot for the reference and N-carbazole molecule, respectively. For the reference molecule the wavefunction is localized on the silane groups, while for the N-carbazole the wavefunction is extended over the carbazole groups, demonstrating the separation between the mechanical anchoring and the electronic path. (b,d) Conductance (G/G_0) for different Fermi energies (E_F) at $T = 0\text{K}$ and room temperature ($T = 300\text{K}$) for the junctions shown in a) and c). $E_F = 0$ corresponds to the DFT-predicted Fermi energy. The shaded area indicates the energy range for which the LDOS in a) and c) have been calculated.

where $f = (1 + \exp((E - E_F)/k_B T))^{-1}$ is the Fermi Dirac distribution function, T is the temperature, and $k_B = 8.6 \times 10^{-5} \text{eV/K}$ is Boltzmann's constant.

Figure 7.3 shows the computed conductance (G/G_0) for both N-carbazole and the reference molecule. The transmission through the reference molecule is systematically lower than for the N-carbazole, regardless of the choice of Fermi energy. Furthermore, the HOMO-LUMO gap is larger for the reference molecule. In addition, as shown in the local density of state calculations (Fig. 7.3a,c), the wave function is extended over the N-carbazole head groups. This indicates that the main transport channels are a result of the π - π interaction between the head groups. This observation highlights the separation between the mechanical anchoring and the charge injection, because the transport channels are localized in the headgroups, while the silane groups are responsible for the mechanical anchoring. Moreover, the head groups are electronically decoupled from the silane anchoring groups by the alkane chains. For the reference molecule, on the other hand, delocalized orbitals are not formed and the transport occurs via the poorly conducting silane groups. These calculations demonstrate the crucial role of π - π stacked head groups in the transport, and rationalize the large differences in conductance observed experimentally for the two molecules.

DFT + NEGF calculations were also performed for various other geometries of the headgroups (see Supplementary information), systematically yielding a larger transmission than for the reference molecule. The calculations also show that the interaction energy between the headgroups is in the range of 10-100meV, which is in the same order of magnitude as thermal fluctuations at room temperature ($k_B T \approx 25 \text{meV}$). We therefore expect such fluctuations to affect transport at room temperature.

7.4. Cluster analysis

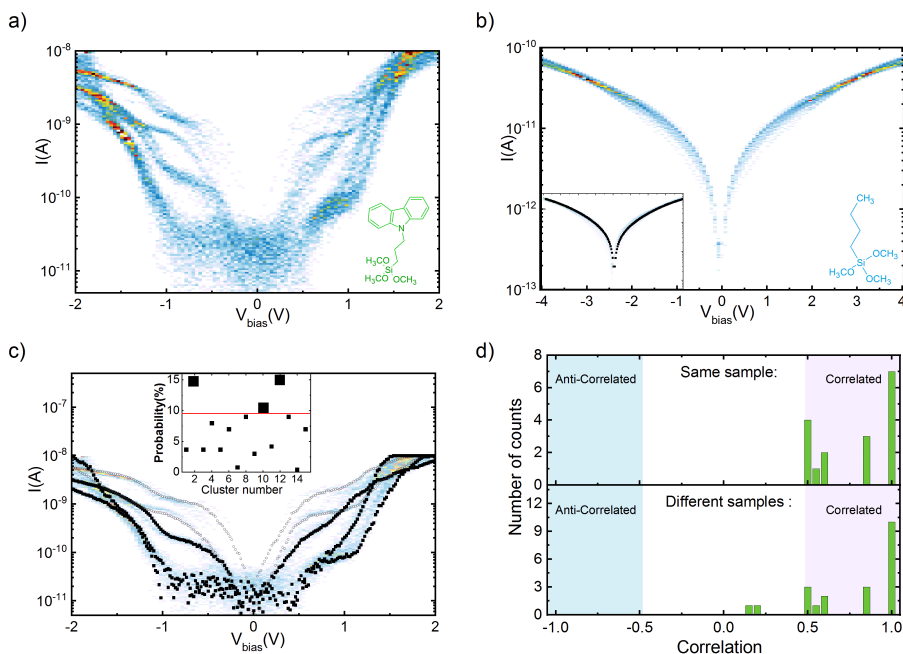


Figure 7.4: Inter-sample reproducibility analysis based on the clustering analysis. a) Density plot of the IVs recorded on one device after deposition of the N-carbazole molecule, plotted on logarithmic scale. b) Density plot of the IVs recorded on one device after deposition of the reference molecule, plotted on logarithmic scale. Note the different current scale for a and b. c) Five average IV curves of the computed clusters are plotted on top of the density plot shown in a). The inset presents the probability distribution for 15 clusters (larger symbols Clusters that are represented in the figure). d) Distribution of the correlation coefficients between devices from the same sample and devices from different samples at 15 clusters. The regions (blue, white, red) are colored according to the degree of correlation (anti-correlated, non-correlated and correlated, respectively).

One of the main challenges of graphene-based molecular junctions is the variability in molecule-like features that are measured before and after deposition and the lack of reproducibility between devices. To determine the reproducibility of the observed features for the N-carbazole molecule, we recorded thousands of IV-curves on different devices and different samples, from which the statistical robustness of our anchoring method can be assessed. The recorded IVs are visualized by constructing density plots in which the areas of high count represent the most likely types of current-voltage characteristic. Such density plots are constructed by dividing both the current and the voltage axes into bins, and assigning each data point of the IVs to the corresponding bin. Figure 7.4a presents the density maps recorded on one device exposed to the N-carbazole molecules with the current on a logarithmic scale. The plot shows variations in the most probable IV-characteristics, with step-like features appearing for each type of IV at different bias voltages and with different heights. In addition, the low-bias conductance and maximum current vary. The density map recorded for the reference molecule (Figure 7.4b), on the other hand, presents only a single type of IV, with negligible variation in the conductance.

Variations in the shapes of IV-curves therefore point towards the critical role of the head group in charge transport through such junctions and may be attributed to changes in its arrangements. These observations are in line with the weak interaction between the head groups. These fluctuations, albeit undesirable for reliable device operation, are intrinsic to the N-carbazole and therefore constitute its distinct signature. In the following, we will utilize these fluctuations to unambiguously demonstrate the robustness of the silanization process for anchoring molecules in graphene-based molecular junctions.

The first step in the robustness analysis of the anchoring is the classification of the IVs according to their shape, while a correlation analysis between samples is performed. For this purpose, we adapt the vector-based data clustering scheme inspired by the work of Albrecht et al. [12]. This approach has been previously used to classify breaking traces in STM break-junction measurements, and we now extend it to categorize IVs. Details of the analysis are presented in the supplementary information. The general idea behind this approach is that the individual IVs are described by one or multiple coordinates, each corresponding to one of its properties, for instance the number of points in the IV, the maximum current, the low-bias conductance, etc. These coordinates are chosen according to the required classification criteria and can be used to cluster data and identify different types of behavior. In this work, IVs are classified according to their shape by comparing them to a reference tunnelling IV, using as coordinates the distance and the angle between the two curves.

We applied the clustering scheme to the combined data set obtained from 6 devices (2 samples), resulting in a total of more than 15000 thousand IV's. For each device, the corresponding tunneling IV was used as the reference. The clustering analysis yields 15 types of IVs. Figure 7.4.c shows the mean IV for each cluster, overlaid on top of the density plot of Figure 7.4.a for one device. The mean IVs reproduce well the areas of high counts in the density map, indicating that the clustering approach successfully identifies the dominant types of behavior.

As the clustering analysis scheme has been applied to the IVs of all samples and devices, each cluster is represented in each device and each sample, albeit with a different probability. This yields a specific probability distribution of clusters for each different device, from which the device-to-device reproducibility is quantified based on the correlation between the probability distribution. Figure 7.4.c presents the distribution of correlation coefficients between two devices from the same sample in the top panel and between two devices from different samples in the lower panel. The upper histogram shows a strong correlation between devices on the same sample, with all coefficients larger than 0.5. The lower plot shows that this correlation also holds when comparing devices on different samples. This is a strong indication that, independently of the sample and device, similar molecular junctions are measured.

7.5. Discussion

Although the junctions are statistically stable and similar conductance maps could be identified from one device to another, for a given device, different groups of conductances are observed. This is attributed to the variability of the number of molecules bridging the gap region and sample parameters such as the gap dimensions (size and width) and the number of OH groups available at the surface of the oxide. In addition, although the width of the

junctions is fixed during the graphene bridge pre-patterning and can therefore be excluded as the main cause for the current differences, the size of the gap is not controlled during the sublimation process. We estimate the gap size of our devices to be in the sub-5nm range. Another crucial parameter is the number of OH groups present at the surface. This number depends on the pre-treatment of the oxide surface and on the high temperature generated during gap formation [2]. To increase the number and uniformity of the active OH sites, ozone treatments and/or exposure to piranha solution could be employed. These treatments, however, are known to damage the graphene.

The multiple categories of IVs can also be explained by considering the possibility of different stacking geometries of the head groups. Figure S1,2 in the Supporting Information shows some examples of different stacking configurations. Our molecular dynamics simulation shows that snake-shape transport paths are formed by $\pi - \pi$ stacking of the head groups (figure S2d in the Supporting Information) could change at room temperature. The resulting changes in the angle between the head groups lead to a variation of the overlap between the adjacent π -orbitals, resulting in differences in the electron transmission function, as evidence by our multi-scale modeling. The total energy difference between the various stacking configurations lies in the 10 – 100meV range, which is comparable to the thermal energy at room temperature. Therefore switching between different geometries will occur. Figure S3 shows that the transmission coefficient, and therefore the electrical conductance, can vary by a few orders of magnitude from one device configuration to another.

Despite the fact that the rich features in charge transport allows for a robust correlation analysis, this behavior is unwanted for a device with a specific function. To decrease the number of configurations, while maintaining the mechanical stability of the anchoring, in-situ polymerisation of the head groups may be employed [17] to lock-in one specific conformation. This would allow for a covalent binding between the head groups and hence a significant decrease of the number of available geometries. Alternatively, one may use larger head groups with a $\pi - \pi$ interaction energy, which is significantly higher than the thermal energy.

7.6. Conclusion

In summary, we have demonstrated the realisation of statistically reproducible graphene-based molecular junctions by anchoring the molecules directly to the substrate using silanization. Using a vector-based clustering method, we identify different transport characteristics in the devices exposed to the N-carbazole molecule. Finally, we show that our novel contacting method is statistically reproducible throughout multiple devices.

Contributions This chapter is under review in Nature Nanotechnology. Maria El Abbassi made the samples and conducted the measurements. Maria El Abbassi and Mickael Perrin performed the data analysis. Shlomo Yitschaik provided the molecule. Sara Sangtarash, Hatef Sadeghi and Colin Lambert performed the DFT calculations.

G. Appendix

G.1. Theory and modeling

Methods

Molecular Dynamic: In order to understand how the 3-carbazolylpropyltrimethoxysilane molecules are interacting with graphene electrodes, molecular dynamic simulation was carried out using ADF [18] reaxFF package. The Velocity Verlet+Berendsen MD method were used with 0.250 fs time step. The atomic positions belong to the SiO_2 substrate and a part of graphene electrodes far from scattering region were constrained. The simulation run for 150000 MD-iterations. The snapshot of atomic coordinates of the junction were taken. These coordinates were used as initial geometries of the device for the density functional theory calculations.

Density functional theory calculation: The optimized geometry and ground state Hamiltonian and overlap matrix elements of each structure studied in this paper were self-consistently obtained using the SIESTA [14] implementation of the density functional theory (DFT). SIESTA employs norm-conserving pseudo-potentials to account for the core electrons and linear combinations of atomic orbitals (LCAO) to construct the valence states. The generalized gradient approximation (GGA) of the exchange and correlation functional is used with the Perdew-Burke-Ernzerhof (PBE) parameterization and a double- ζ polarized (DZP) basis set. The real-space grid is defined with an equivalent energy cut-off of 250 Ry. The geometry optimization for each structure is performed to the forces smaller than 20 meV/Å.

Transport: The mean-field Hamiltonian obtained from the converged SIESTA DFT calculation was combined with Gollum [15] implementation of the non-equilibrium Green's function method, to calculate the phase-coherent, elastic scattering properties of the each system consist of left (source) and right (drain) graphene leads connected to the scattering region formed from 3-carbazolylpropyltrimethoxysilane molecules. The transmission coefficient $T(E)$ for electrons of energy E (passing from the source to the drain) is calculated via the relation $T(E) = \text{trace}(\Gamma_R(E)G^R(E)\Gamma_L G^{R\dagger}(E))$. In this expression, $\Gamma_{L,R} = i(\Sigma_L, R(E) - \Sigma_L, R^\dagger(E))$ describe the level broadening due to the coupling between left (L) and right (R) electrodes and the central scattering region, are the retarded self-energies associated with this coupling and $G^R = (ES - H - \Sigma_L - \Sigma_R)^{-1}$ is the retarded Green's function, where H is the Hamiltonian and S is the overlap matrix. Using obtained transmission coefficient, the conductance is calculated by Landauer formula $G = G_0 \int dE T(E) (-\partial f(E, T) / \partial E)$ where $G_0 = 2e^2/h$ is the conductance quantum, $f(E, T) = (1 + \exp((E - E_F)/k_B T))^{-1}$ is the Fermi-Dirac distribution function, T is the temperature and $k_B = 8.6 \cdot 10^{-5}$ eV/K is Boltzmann's constant.

Molecular dynamic simulation of junctions

In order to understand how the 3-carbazolylpropyltrimethoxysilane molecules are interacting with graphene electrodes, we have carried out molecular dynamic simulation of a junction consisting of two graphene electrodes, SiO_2 substrate and the 3-carbazolylpropyltrimethoxysilane molecules in the gap (fig. 7.5) using ADF reaxFF package. The 3-carbazolylpropyltrimethoxysilane molecules are covalently bonded to the substrate through silane groups. Simulation has been carried out in the room temperature. The atoms in the substrate and part of the graphene electrodes are geometrically constrained to study behavior of the molecules in the junction and their interaction with graphene edges and surface in contact points. As a separate video

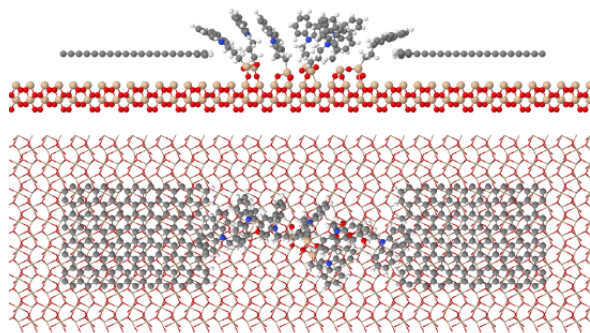


Figure 7.5: Junction geometry: shows the molecular structure of the junction formed by 3-carbazolylpropyltrimethoxysilane molecules in graphene nanogap on SiO_2 substrate.

file in the SI, we have made a movie of the dynamic of the junction. It is apparent that the N-carbazole groups interact with each other and the graphene surface through $\pi - \pi$ overlap between p orbitals of the N-carbazole group and graphene. Since the N-carbazole groups are attached to the SiO_2 substrate through flexible alkanes, the molecules are floppy and fluctuate at room temperature. We have taken snapshots of these junctions, and performed geometry relaxation using density functional theory and obtained mean-field Hamiltonian (see methods). These mean-field Hamiltonians were combined with the transport code Gollum to calculate the electrical properties of the junction.

Transport through the junctions with different conformations

We now consider junctions with four different arrangements as shown in figure 7.6. The corresponding zero and room temperature conductance graphs are shown in figure 7.7. Fig.7.6a shows the molecular structure of a junction where the N-carbazole groups inter-act

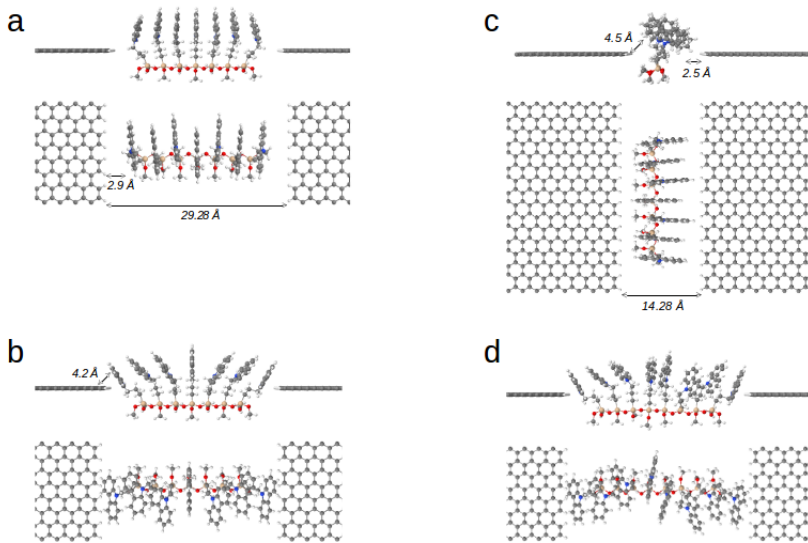


Figure 7.6: Graphene/molecule/graphene junctions: a-d show four example of molecular junctions formed by 3-carbazolylpropyltrimethoxysilane molecules between graphene electrodes.

with each other through $\pi - \pi$ interaction. However, they do not make a $\pi - \pi$ overlap with the graphene electrodes. In contrast, figure 7.6b shows the molecular structure of a junction where not only the N-carbazole groups interact with each other through $\pi - \pi$ interaction, but also do they make a $\pi - \pi$ overlap with the graphene electrodes. Figure 7.7a,b show corresponding conductance graphs. The conductance of the junction a is much less than the junction b. This demonstrates the crucial effect of the $\pi - \pi$ overlap with the graphene electrodes. Our MD and DFT simulations show that this $\pi - \pi$ overlap is energetically favorable. Figure 7.6c,d and corresponding conductance graphs in figure 7.7c,d show other examples of the junctions that may be formed.

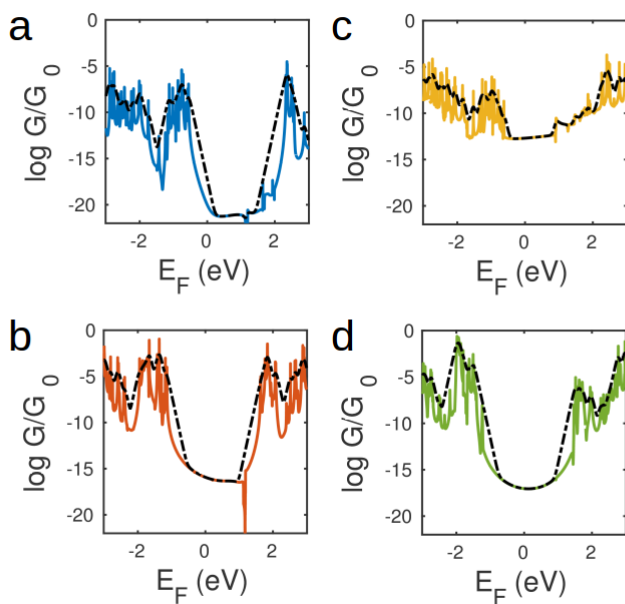


Figure 7.7: Conductance vs. Fermi energies: a-d show conductance for different Fermi energies in the unit of G_0 for the junction a-d in figure S7.6 respectively. Colored graphs are zero temperature conductances and dashed black line shows the corresponding room temperature conductances.

G.2. Clustering method and data analysis

Vector based clustering technique

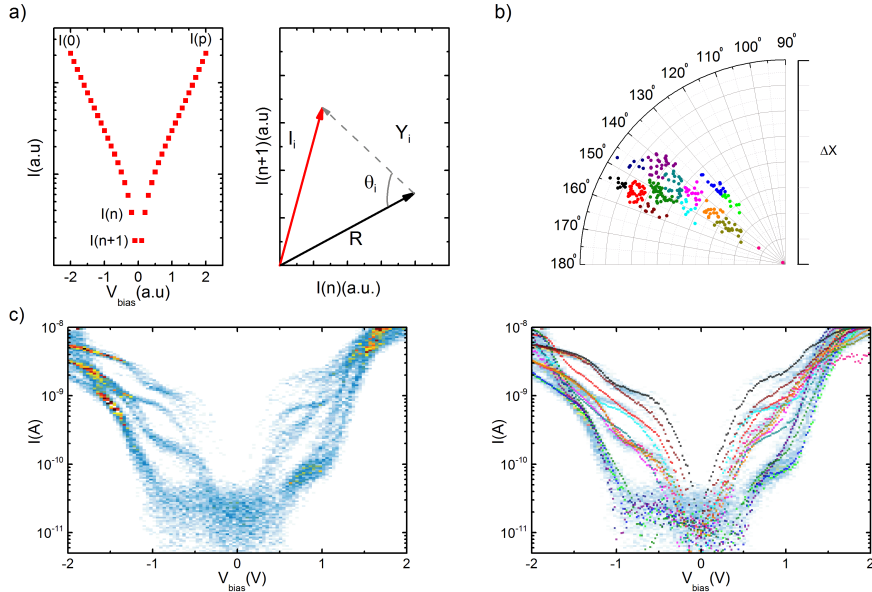


Figure 7.8: Description of the clustering analysis of the IV's: a) Left panel: Example of an IV plotted in log-scale with p data points. In the vector analysis approach, the p data points correspond to a p -dimension vector. Right panel: A reference vector corresponding to the tunneling regime is taken for all the junctions. Both reference the vector and data vector have p dimensions. For every IV vector, we calculate the angle between the two vectors (θ) and the norm of the $Y = I - R$. b) Every IV corresponds then to a point defined by the norm Y and angle θ that we plot in this polar plot. Gaussian fit is applied to fit the distribution of clusters. Points corresponding to the 15 different clusters are plotted in different color. c) Left panel: Density plot in the log-scale of IV's after deposition of the N-carbazole molecule. Large variability of IV's is observed. Right panel: Mean IV for every cluster is plotted on top of the density plot of the IV's. One can see the the mean IV's reproduce in a very good agreement features of the left panel.

In the cluster analysis, each IV (I_i with $i = 1, \dots, N$, N being the total number of IVs) is considered to be a p -dimensional vector $\vec{I}_i(p)$, which is of equal dimension as the reference vector $\vec{R}(p)$. We take as a reference, the vector $\vec{R}(p)$ corresponding to the tunneling curve before deposition of molecules. The first coordinate to be defined for the classification algorithm is the norm of the difference vector, $|\vec{Y}_i|$, where $\vec{Y}_i(p) = \vec{I}_i(p) - \vec{R}(p)$. The second one is the angle between the difference vector $\vec{Y}_i(p)$ and the reference vector $\vec{R}(p)$, yielding an angle θ_i . Every IV is then represented as a point of which the coordinates are the norm and the angle. To group all the obtained points in clusters, a 2D-Gaussian fitting scheme is used. Table 6 contains the distribution of IV's per cluster for the device shown in Figure 5c), together with the population of the remaining devices. The right panel of Fig. 5c) presents the color coded mean IV for all 15 clusters, which reproduce well the main features of the left panel.

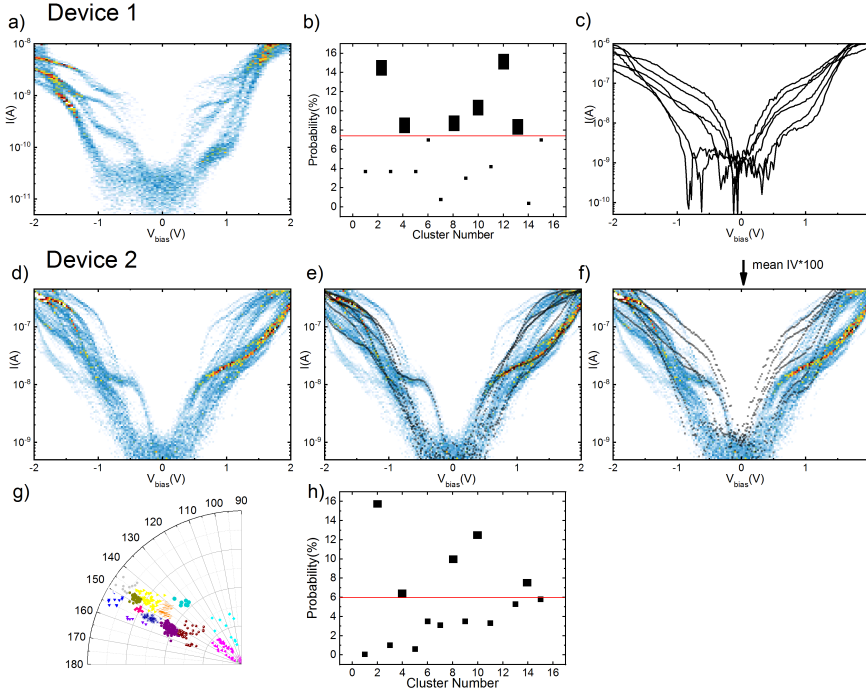


Figure 7.9: Device 1: a) Density plot in the log-scale of IV's after deposition of the N-carbazole molecule. b) Probability distribution for 15 clusters. c) Mean IVs of the five most probable clusters (large symbol in panel b). **Device 2:** d) Density plot in the log-scale of IV's after deposition of the N-carbazole molecule. e) Mean IV of the five most probable clusters (large symbol in the inset panel) are plotted on top of the density plot of the IV's. f) Five most probable mean IVs of device 1 plotted on top of the density plot of device 2. g) Polar plot of the corresponding points to the IV curves. h) Probability distribution for 15 clusters.

Correlation factor calculation

Determining the total number of clusters is non trivial and can in principle vary from 1 to N , N being the total number of IV's. In this study, we use the mean correlation coefficient between the samples to determine the suitable number of clusters. If we consider two devices a and b , and $A(c)$ and $B(c)$ the corresponding distribution probability of IVs per cluster, the correlation between the distributions A and B is defined as follows:

$$\text{correlation}(A,B) = \frac{\text{cov}(A,B)}{\sigma_A \sigma_B}, \quad (7.1)$$

where $\text{cov}(A,B)$ corresponds to the covariance between the distribution probabilities $A(c)$ and $B(c)$, and σ to their standard deviations. For all possible device combinations, we take the mean of all the correlation coefficient, for a given number of clusters. To determine the maximum number of clusters, we repeat this analysis for 1 to 18 cluster.

In fig.7.10, the plot shows that between 3 to 15 clusters the devices are highly correlated, with coefficients around 0.8. For more than 16 clusters, a drastic decrease in correlation is

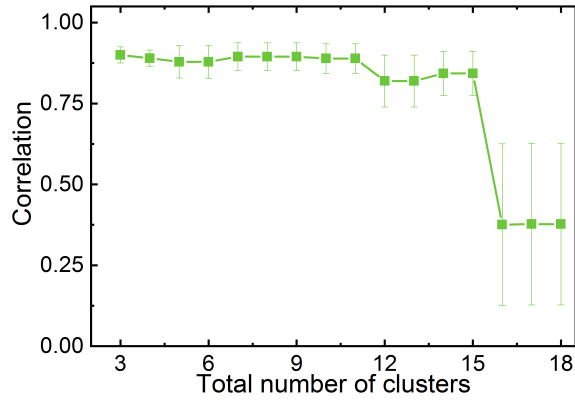


Figure 7.10: Average correlation factor between all the devices as a function of the number of clusters.

observed, meaning that clusters are being split that don't reproduce the main IV behaviours. For our study, we therefore use 15 clusters.

Example of measurements from other samples

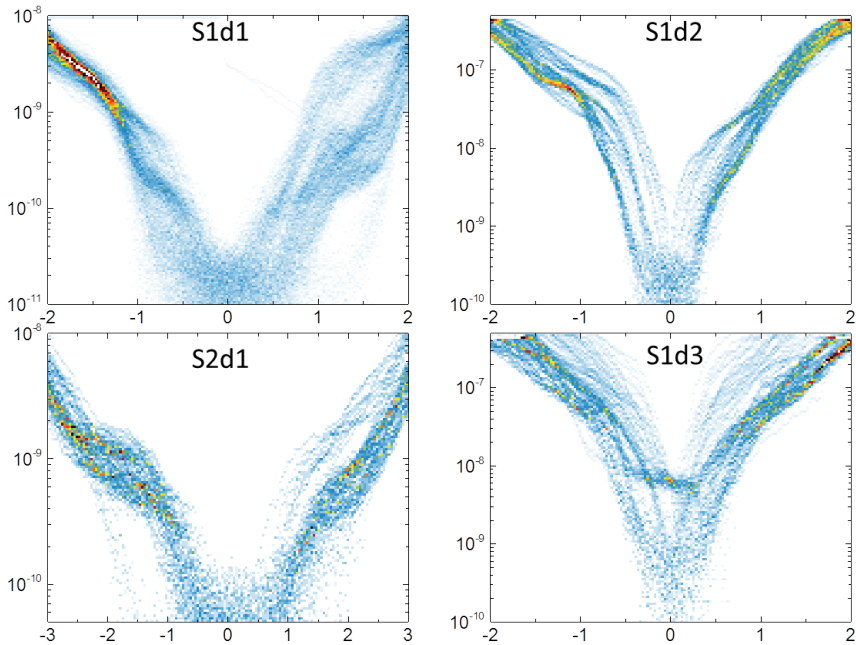


Figure 7.11: Density plot of 4 devices from 2 different samples.

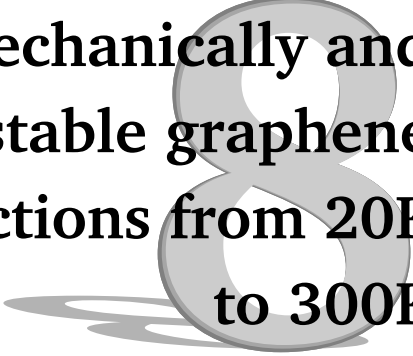
Figure 7.11 presents the density plots of devices from different samples. Qualitatively similarities between the different devices are observed that were characterized quantitatively using the clustering method.

Bibliography

- [1] Chit Siong Lau, Hatef Sadeghi, Gregory Rogers, Sara Sangtarash, Panagiotis Dallas, Kyriakos Porfyrakis, Jamie Warner, Colin J Lambert, G Andrew D Briggs, and Jan A Mol. Redox-dependent Franck–Condon blockade and avalanche transport in a graphene–fullerene single-molecule transistor. *Nano letters*, 16(1):170–176, 2015.
- [2] Amelia Barreiro, Herre SJ van der Zant, and Lieven MK Vandersypen. Quantum dots at room temperature carved out from few-layer graphene. *Nano letters*, 12(12):6096–6100, 2012.
- [3] Hatef Sadeghi, Jan A Mol, Chit Siong Lau, G Andrew D Briggs, Jamie Warner, and Colin J Lambert. Conductance enlargement in picoscale electroburnt graphene nanojunctions. *Proceedings of the National Academy of Sciences*, 112(9):2658–2663, 2015.
- [4] Pascal Gehring, Hatef Sadeghi, Sara Sangtarash, Chit Siong Lau, Junjie Liu, Arzhang Ardavan, Jamie H Warner, Colin J Lambert, G Andrew D Briggs, and Jan A Mol. Quantum interference in graphene nanoconstrictions. *Nano letters*, 16(7):4210–4216, 2016.
- [5] Hatef Sadeghi, Sara Sangtarash, and Colin Lambert. Robust molecular anchoring to graphene electrodes. *Nano Letters*, 17(8):4611–4618, 2017.
- [6] Suzhi Li, Qunyang Li, Robert W Carpick, Peter Gumbsch, Xin Z Liu, Xiangdong Ding, Jun Sun, and Ju Li. The evolving quality of frictional contact with graphene. *Nature*, 539(7630):541–545, 2016.
- [7] Hatef Sadeghi, Sara Sangtarash, and Colin Lambert. Robust molecular anchoring to graphene electrodes. *Nano Letters*, 17(8):4611–4618, 2017.
- [8] Chuancheng Jia, Agostino Migliore, Na Xin, Shaoyun Huang, Jinying Wang, Qi Yang, Shuopei Wang, Hongliang Chen, Duoming Wang, Boyong Feng, Zhirong Liu, Guangyu Zhang, Da-Hui Qu, He Tian, Mark A. Ratner, H. Q. Xu, Abraham Nitzan, and Xuefeng Guo. Covalently bonded single-molecule junctions with stable and reversible photoswitched conductivity. *Science*, 352(6292):1443–1445, 2016.
- [9] László Pósa, Maria El Abbassi, Péter Makk, Botond Sánta, Cornelia Nef, Miklós Csontos, Michel Calame, and András Halbritter. Multiple physical time scales and dead time rule in few-nanometers sized graphene–sio x-graphene memristors. *Nano letters*, 17(11):6783–6789, 2017.

- [10] Jan A Mol, Chit Siong Lau, Wilfred JM Lewis, Hatef Sadeghi, Cecile Roche, Arjen Cnossen, Jamie H Warner, Colin J Lambert, Harry L Anderson, and G Andrew D Briggs. Graphene-porphyrin single-molecule transistors. *Nanoscale*, 7(31):13181–13185, 2015.
- [11] Qizhi Xu, Giovanni Scuri, Carly Mathewson, Philip Kim, Colin Nuckolls, and Delphine Bouilly. Single electron transistor with single aromatic ring molecule covalently connected to graphene nanogaps. *Nano letters*, 17(9):5335–5341, 2017.
- [12] Mario Lemmer, Michael S Inkpen, Katja Kornysheva, Nicholas J Long, and Tim Albrecht. Unsupervised vector-based classification of single-molecule charge transport data. *Nature communications*, 7, 2016.
- [13] Sandra Gilles. *Chemical modification of silicon surfaces for the application in soft lithography*. PhD thesis, Forschungszentrum, Zentralbibliothek, 2007.
- [14] José M Soler, Emilio Artacho, Julian D Gale, Alberto García, Javier Junquera, Pablo Ordejón, and Daniel Sánchez-Portal. The siesta method for ab initio order-n materials simulation. *Journal of Physics: Condensed Matter*, 14(11):2745, 2002.
- [15] Jaime Ferrer, Colin J Lambert, Víctor Manuel García-Suárez, D Zs Manrique, D Visontai, L Oroszlany, Rubén Rodríguez-Ferradás, Iain Grace, SWD Bailey, Katalin Gillemot, H Sadeghi, and LA Algharagholy. Gollum: a next-generation simulation tool for electron, thermal and spin transport. *New Journal of Physics*, 16(9):093029, 2014.
- [16] Alexey V Krasnoslobodtsev and Sergei N. Smirnov. Effect of water on silanization of silica by trimethoxysilanes. *Langmuir*, 18(8):3181–3184, 2002.
- [17] T. Zhang, D. Guérin, F. Alibart, D. Vuillaume, K. Lmimouni, S. Lenfant, A. Yassin, M. Oçafrain, P Blanchard, and J. Roncali. Negative differential resistance, memory, and reconfigurable logic functions based on monolayer devices derived from gold nanoparticles functionalized with electropolymerizable tedot units. *The Journal of Physical Chemistry C*, 121(18):10131–10139, 2017.
- [18] F. Lorant A.C.T. van Duin, S. Dasgupta and W. A. Goddard. Reaxff: A reactive force field for hydrocarbons. *Journal of Physical Chemistry A*, 105:9396–9409, 2001.

Reproducible mechanically and electronically stable graphene molecular junctions from 20K to 300K



In this chapter, we report on the realization of a mechanically, electronically and statistically robust graphene-based molecular junction. The mechanical stability is achieved by covalently binding the molecule to the substrate [1, 2]. The electronic stability is due to a large overlap of the π orbitals of the conjugated head groups. The reproducibility is possible due to the nature of the $\pi - \pi$ stacking binding that is less sensitive to the electrode properties [3]. Several devices were characterized at 20 K and all showed resonance peaks at similar bias positions. Electronical stability is demonstrated by performing transport measurements of the devices from 20 K to 300 K, and observing the presence of a single category of IV-curve that is not significantly dependent on the temperature.

Introduction

One of the main challenges of molecular electronics is to achieve a mechanically stable device with reproducible and controllable electronic features, operating at room temperature [4, 5]. However, achieving at the same time mechanical stability and electrical reproducibility is not straightforward, as both impose different requirements on the junction properties [3, 6]. For mechanical stability, covalent binding of the molecule is needed [7], in particular when operating at room temperature. However, a strong interaction between the molecule and the electrode makes the electronic transport properties very sensitive to the electrode shape [3]. Due to the lack of control on the electrode geometry at the nanoscale, finding the proper balance between electronic and mechanical stability is challenging [8–12].

8.1. Junction geometry

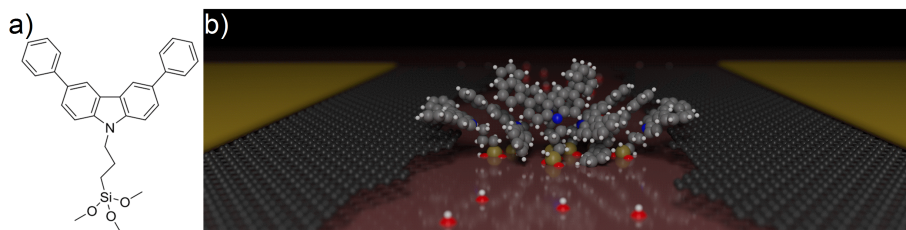


Figure 8.1: Junction Geometry (a) Drawing of the molecule measured. It is constituted of three main parts: the silane group for the covalent anchoring to the substrate, the alkane chain that decouples the silane group from the head group and the benzene-carbazole groups. (b) Schematic of the ground-state relaxed geometry of seven molecules in series bridging a graphene nanogap. The nanogaps are formed using the electrical breakdown technique. The molecules are attached to the substrate via silanization of the surface. OH groups are represented with red and white atoms on the SiO₂ surface. The color difference between the carbon atoms of the molecule and those of the graphene is for clarity reasons only.

In this study, we propose a new strategy to separate mechanical from electronic stability and as such achieve stable and reproducible junctions. This was realized by combining the stability of graphene electrodes with a specifically designed molecule, shown in Figure 8.1 a). Graphene was chosen as electrode material as it exhibits a high structural stability for a wide temperature range as a result of the covalent binding between neighboring carbon atoms. The molecule was designed with two main parts (an alkoxy silane group, and a π -conjugated head group), decoupled by a non-conjugated alkane chain (in the following, this molecule will be referred to as BC). The alkoxy silane part of the molecule reacts with the hydroxyl groups, present on the silicon dioxide surface, and forms a Si-O-Si bond [1, 2]. By covalently binding the molecule to the substrate using the silane group, we provide mechanically stable anchoring to the graphene-molecules junction. The electronic stability, on the other hand, is achieved by using large π -conjugated head groups with a strong interaction energy. The head group consists of two benzene rings connected to a carbazole group. The interaction energy is significantly larger than the thermal energy at room temperature ($k_B T = 25\text{meV}$). The molecules in the graphene nanogap after assembly are schematically shown in Figure 8.1 b).

The nanogaps in the graphene devices were formed using the electrical breakdown technique, as explained in previous studies [8, 13, 14] (see chapter 3). The graphene gaps

are first characterized at room temperature and at low temperature, before deposition of the molecules. Only junctions with resistances higher than $100M\Omega$ are selected for further use. After characterization of the empty gaps, the devices were immersed for 20 hours at 80 degrees in a solution containing dry toluene and the molecules of concern. The sample was then subsequently rinsed with dichloromethane, acetone and isopropanol.

8.2. Stability and intersample reproducibility at 20 K

After deposition of the molecules, the devices were cooled down to 20 K and characterized, as shown in Fig. 8.2 for three different devices. For each device, 100 IV curves were recorded successively. The left panel presents the density plot of these IVs, plotted on logarithmic scale. For all devices, small fluctuations are observed, with only one category of IVs present. For every device, the average IV is calculated, shown as inset, and exhibit similar currents and shape. Indeed, current amplitudes vary only by a factor of about 4 between the three devices, suggesting that a similar number of molecules is bridging the gap.

The right panel presents the corresponding differential conductance (dI/dV) traces (blue line), obtained by numerical differentiation of the average IV curve. For comparison, the red traces display the dI/dV curve before deposition. Resonance peaks are observed only after deposition, proving that they are a signature of the molecule. The positions of the predominant resonances measured for the three devices are highlighted with gray-shaded regions. These resonances are located at similar positions, as a result of the molecules being weakly coupled to the electrodes. However the resonances exhibit different amplitudes, which can be attributed to local variations in the junction configuration. These observations confirm the reproducibility of the electrical measurements.

8.3. Electronical stability of the junction at different temperatures

To further investigate the junction stability, the devices were characterized in a large range of temperature extending from 20 K to room temperature. Figure 8.3 a) shows the density plot of the recorded IV curves measured at three selected temperatures (20K, 150K and 300K) for device 1. From the density plots, one main category of IVs is observed throughout the entire temperature range with insignificant fluctuations, highlighting the high electronic stability up to room temperature.

Figure 8.3 b displays the evolution of the dI/dV with temperature. Independently on the temperature, only small fluctuations in intensity are measured. This is confirmed in Fig.8.3 c, where the differential conductance dI/dV at three selected temperatures is presented, showing similar resonances at comparable positions. At temperatures higher than 160 K, small differences in amplitude and broadening are observed. This can be attributed to thermal effects inducing the broadening of the density of state of the electrode and/or small local variations in the configuration of the molecules. Differential conductance at three selected temperatures are plotted in Figure 8.3 d. At 20K and 150K, the intensity of the resonance peak around 0.8 V however the width of the peak remains constant. At 300K, this resonance peak is broader with a smaller intensity (see appendix). In general, we could observe a transition in the behavior of the junction is observed at 160K (marked with the arrow).

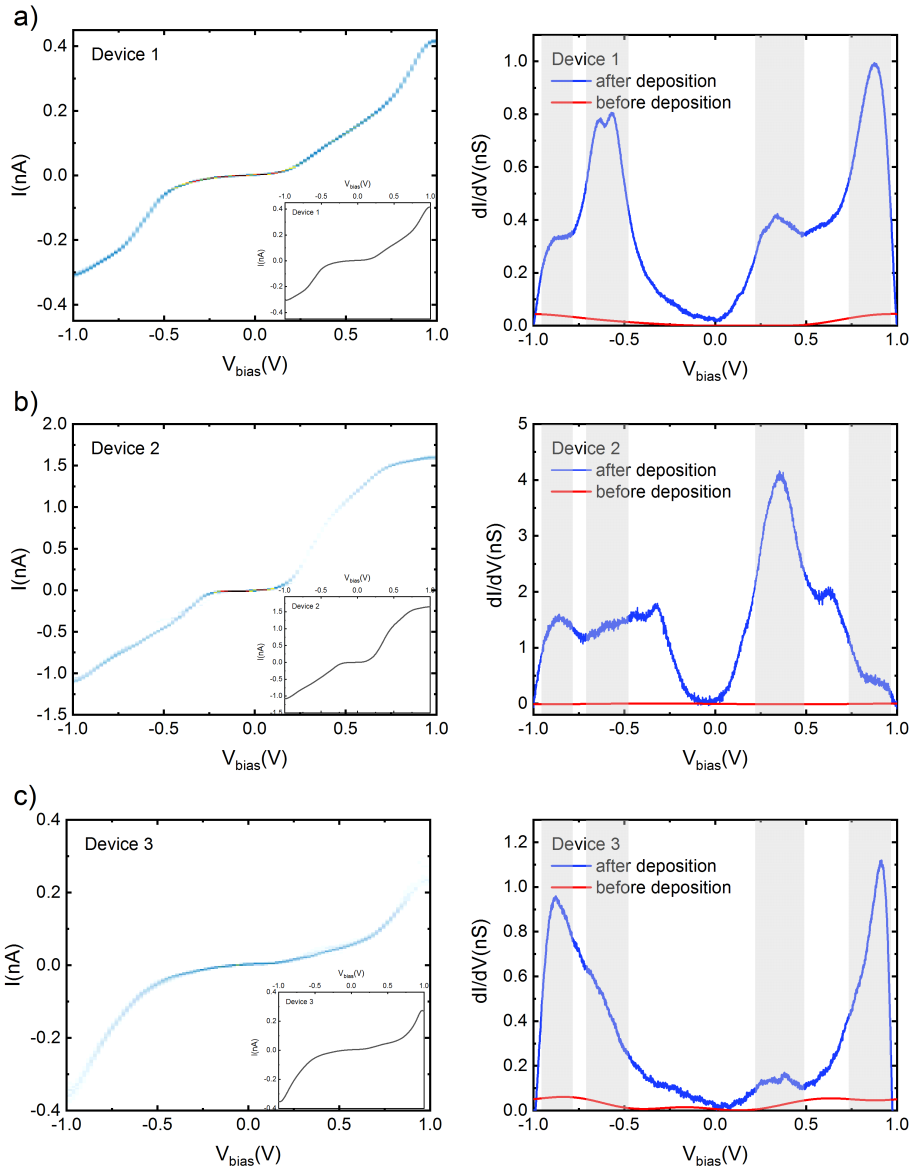


Figure 8.2: Device characterization at 20 K. (Left panels) density plots of IVs recorded on junctions 1, 2, 3 (respectively a, b, c), plotted on logarithmic scale. The inset shows the calculated average IV (Right panel) dI/dV before (red) and after (blue) deposition. The resonances observed after deposition correspond to electronic energy levels of the molecular junction. The gray regions highlight the common resonances.

Figure 8.3 d presents the logarithmic value of the current as a function of temperature for different voltage values. Independently on the applied bias voltage, the currents remain constant for the entire temperature range. Overall, the junction shows electrical stability

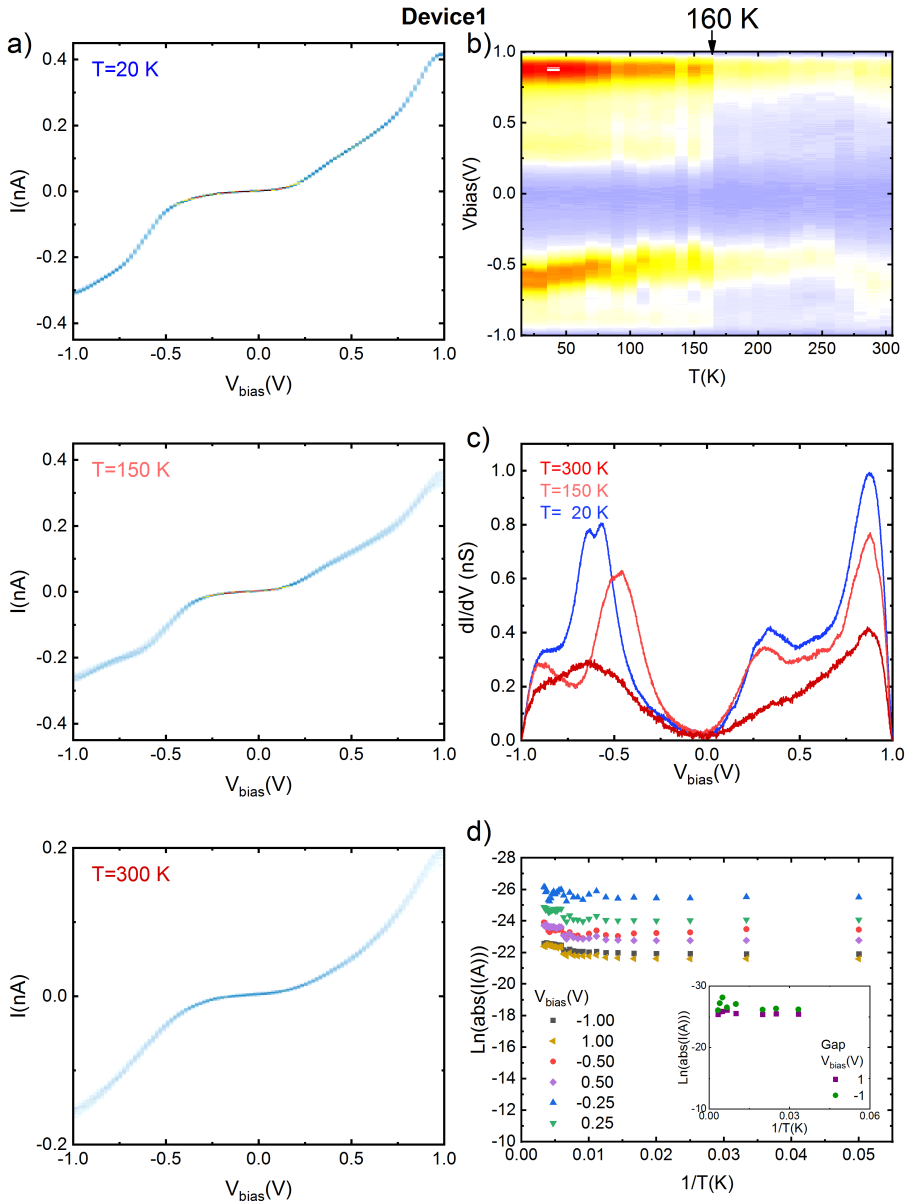


Figure 8.3: Transport measurements through a molecular junction at different temperatures. (a) Density plot of the IVs plotted on logarithmic scale. (b) Graph showing the evolution of the dI/dV as a function of temperature. (c) Differential conductance dI/dV of the device shown in a) plotted for three selected temperatures. (d) Evolution of the logarithmic value of the current as a function of the inverse of the temperature plotted for different bias values. The inset shows the behavior of an empty gap before deposition.

in the range of 20 K to 300 K, with one only IV type observed. To verify that both the

molecular and the graphene gaps are stable with temperature, we performed a temperature characterization of the empty nanogaps before deposition (see appendix for more details). The inset of Fig.8.3 d presents of the evolution of the current of a tunneling nanogap. In agreement with previous studies [8], no significant effect of temperature is observed.

8.4. Discussion

In the appendix of this chapter, we present a preliminary study of the temperature dependence of the transport through the junctions (see appendix F.4). We define two temperature regions: low temperature (between 20K and 160K) and high temperature (between 160K and 300K). We first estimate the activation energies at different bias voltage values using an Arrhenius model. In the low temperature regime, the current is constant over the whole range leading to energies lower than 0.3 meV. Whereas in the high temperature regime, we could observe larger fluctuations of the current around the transition at 160K. However, these fluctuations do not follow an Arrhenius relation describing an incoherent thermally activated hopping [15, 16]. Basically in this regime, the molecular structure is described using multiple sites separated by an energy barrier called the hopping activation energy E_a . It is an incoherent process because when travelling between the different sites, the electron loses its phase. The activation energy of such process is given by the slope of the Arrhenius plot $G = G_0 \exp(-E_a/(k_B T))$. In our case, we could observe that the exponential fit is not so appropriate at higher temperature for small bias values. However, assuming an Arrhenius dependence, we could extract negative activation energies (decreasing current with increasing temperature) lower than 10 meV at high temperature (see appendix F.4). We can conclude that we do not measure a thermally activated transport due to incoherent hopping. The temperature dependence of the transport can be explained by a rearrangement of the molecules inside the gap ($\pi - \pi$ stacking of the molecules) that is possible at higher temperature. The electron transport remains coherent, however due to the change in the local configuration of the molecules, the effective barrier that the electron has to tunnel through is slightly changing. Our collaborators in Lancaster are performing DFT and molecular dynamics calculations to estimate the difference of energy between the different configurations and calculate the corresponding transmissions (preliminary results are shown in appendix F.2).

8.5. Conclusion

To conclude, this work shows the realization of electronically and mechanically stable graphene based molecular devices. The junctions are reproducible throughout several devices and operate up to room temperature. Our approach allows for the future integration of novel molecule based functions into stable and controllable nano-electronic devices.

Contributions This chapter is part of a manuscript under preparation. Maria El Abbassi made the samples and conducted the measurements. Mickael Perrin made the schematic picture. Xunshan Liu, Shi-Xia Liu and Silvio Decurtins provided the molecule. Sara Sangtarash, Hatef Sadeghi and Colin Lambert performed the DFT calculations.

Bibliography

- [1] Sandra Gilles. *Chemical modification of silicon surfaces for the application in soft lithography*. PhD thesis, Forschungszentrum, Zentralbibliothek, 2007.
- [2] Alexey V. Krasnoslobodtsev and Sergei N. Smirnov. Effect of water on silanization of silica by trimethoxysilanes. *Langmuir*, 18(8):3181–3184, 2002.
- [3] Hatef Sadeghi, Sara Sangtarash, and Colin Lambert. Robust molecular anchoring to graphene electrodes. *Nano Letters*, 17(8):4611–4618, 2017.
- [4] Visions for a molecular future. *Nature Nanotechnology*, 8(6):385–389, 2013.
- [5] Sriharsha V Aradhya and Latha Venkataraman. Single-molecule junctions beyond electronic transport. *Nature nanotechnology*, 8(6):399–410, 2013.
- [6] Timothy A Su, Madhav Neupane, Michael L Steigerwald, Latha Venkataraman, and Colin Nuckolls. Chemical principles of single-molecule electronics. *Nature Reviews Materials*, 1:16002, 2016.
- [7] Suzhi Li, Qunyang Li, Robert W Carpick, Peter Gumbsch, Xin Z Liu, Xiangdong Ding, Jun Sun, and Ju Li. The evolving quality of frictional contact with graphene. *Nature*, 539(7630):541–545, 2016.
- [8] Ferry Prins, Amelia Barreiro, Justus W Ruitenbergh, Johannes S Seldenthuis, Núria Aliaga-Alcalde, Lieven MK Vandersypen, and Herre SJ van der Zant. Room-temperature gating of molecular junctions using few-layer graphene nanogap electrodes. *Nano letters*, 11(11):4607–4611, 2011.
- [9] NJ Tao. Electron transport in molecular junctions. *Nature nanotechnology*, 1(3):173–181, 2006.
- [10] Chit Siong Lau, Hatef Sadeghi, Gregory Rogers, Sara Sangtarash, Panagiotis Dallas, Kyriakos Porfyraakis, Jamie Warner, Colin J Lambert, G Andrew D Briggs, and Jan A Mol. Redox-dependent Franck-Condon blockade and avalanche transport in a graphene-fullerene single-molecule transistor. *Nano letters*, 16(1):170–176, 2015.
- [11] Chuancheng Jia, Agostino Migliore, Na Xin, Shaoyun Huang, Jinying Wang, Qi Yang, Shuopei Wang, Hongliang Chen, Duoming Wang, Boyong Feng, Zhirong Liu, Guangyu Zhang, Da-Hui Qu, He Tian, Mark A. Ratner, H. Q. Xu, Abraham Nitzan, and Xuefeng Guo. Covalently bonded single-molecule junctions with stable and reversible photoswitched conductivity. *Science*, 352(6292):1443–1445, 2016.

- [12] Pascal Gehring, Hatef Sadeghi, Sara Sangtarash, Chit Siong Lau, Junjie Liu, Arzhang Ardavan, Jamie H Warner, Colin J Lambert, G Andrew D Briggs, and Jan A Mol. Quantum interference in graphene nanoconstrictions. *Nano letters*, 16(7):4210–4216, 2016.
- [13] Cornelia Nef, László Pósa, Péter Makk, Wangyang Fu, András Halbritter, Christian Schönenberger, and Michel Calame. High-yield fabrication of nm-size gaps in monolayer cvd graphene. *Nanoscale*, 6(13):7249–7254, 2014.
- [14] Maria El Abbassi, László Pósa, Péter Makk, Cornelia Nef, Kishan Thodkar, András Halbritter, and Michel Calame. From electroburning to sublimation: substrate and environmental effects in the electrical breakdown process of monolayer graphene. *Nanoscale*, 9(44):17312–17317, 2017.
- [15] Yoram Selzer, Marco A. Cabassi, Theresa S. Mayer, and David L. Allara. Thermally Activated Conduction in Molecular Junctions *JACS*, 126:4052–4053, 2004.
- [16] Thomas Hines, Ismael Diez-Perez, Joshua Hihath, Hongmei Liu, Zhong-Sheng Wang, Jianwei Zhao, Gang Zhou, Klaus Mullen, and Nongjian Tao. Transition from Tunneling to Hopping in Single Molecular Junctions by Measuring Length and Temperature Dependence *JACS*, 132:11658–11664, 2010.

F. Appendix

F.1. Synthesis and characterization of the target molecule

Compounds 1,1 was synthesized according to the reported procedure. Unless otherwise stated, all chemicals and solvents were purchased from commercial sources and were used without further purification. The target compounds 3 has been characterized by high-resolution Mass spectrum (HRMS) which was recorded with an Auto Spec Q spectrometer in ESI (electrospray ionization) mode.

In a dry 250-mL round-bottomed flask filled with nitrogen, compound 1 (500 mg, 1.57 mmol) and dry DMF (120 mL) were charged and stirred for 20 min. K_2CO_3 (441 mg, 3.20 mmol) was added and stirred for an additional 20 min. The compound 2 (770 mg, 3.20 mmol) was added at a time via syringe under nitrogen at room temperature, and the reaction solution was stirred for 36 h at 130 degrees C. After filtration, the filtrate was evaporated to expel the solvent and an excess amount of compound 2 under vacuum. The product (551 mg, 73 percent calculated from 1H NMR) was kept in a dry and N_2 protected desiccator. The product was used for the following measurements without further purification. HRMS (ESI): m/z calcd for $C_{30}H_{31}NO_3Si$, 481.2073; found: 481.2078.

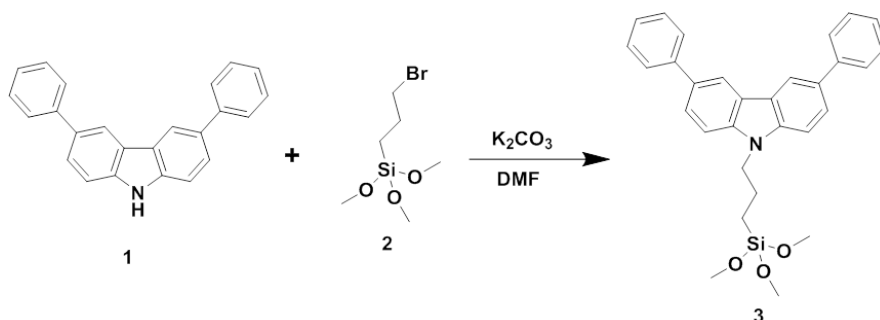


Figure 8.4: Synthesis steps of compound 3.

F.2. Transport through the junctions with different geometries

In order to understand how the new carbazole-benzene molecules are interacting with graphene electrodes, Sara Sangtarash, Hatef Sadeghi and Colin Lambert from Lancaster university have carried out molecular dynamic simulation of a junction consisting of two graphene electrodes, SiO_2 substrate and the molecules in the gap using ADF reaxFF package, similar to the previous chapter. The atoms in the substrate and part of the graphene electrodes are geometrically constrained to study behavior of the molecules in the junction and their interaction with graphene edges and surface in contact points.

They have performed geometry relaxation using density functional theory and obtained mean-field Hamiltonian (see methods chapter 7).

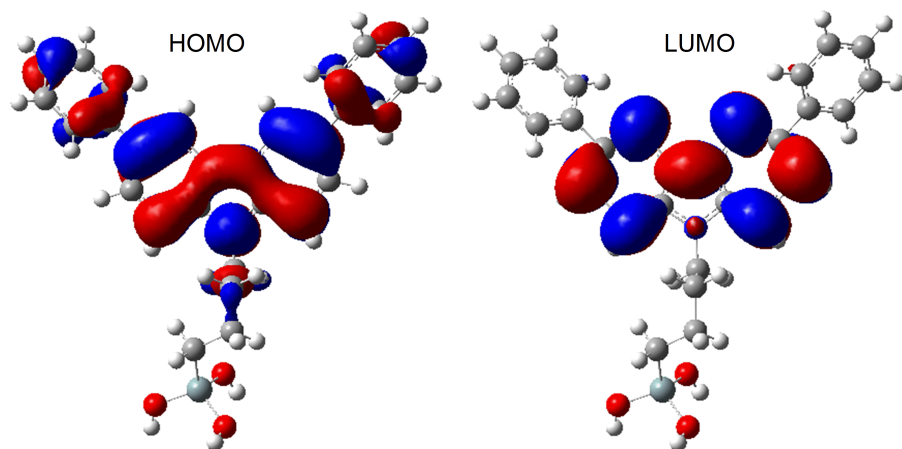


Figure 8.5: Isosurfaces of the wavefunctions of the HOMO and LUMO of the molecule using density functional theory.

Figure 8.5 shows the wavefunction of both frontier orbital, the highest occupied molecular orbital (HOMO) and the lowest unoccupied molecular orbital (LUMO), are mostly localized on the head group. This confirms that the electron transport will be mainly mediated by the head groups.

The mean-field Hamiltonians were combined with the transport code Gollum to calculate the electrical properties of the junction. We now consider junctions with four different arrangements as shown in figure 8.6. The corresponding zero and room temperature conductance graphs are shown in figure 8.7.

Fig. 8.6a shows the molecular structure of a junction where the carbazole-benzene groups interact with each other through $\pi - \pi$ interaction. The different values of conductance varies from a geometry to the other. This demonstrates the crucial effect of the $\pi - \pi$ overlap with the graphene electrodes. Our MD and DFT simulations show that this $\pi - \pi$ overlap is energetically favorable and that the carbazole-benzene molecules has a higher interaction energy than a simple carbazole and have the tendency to aggregate.

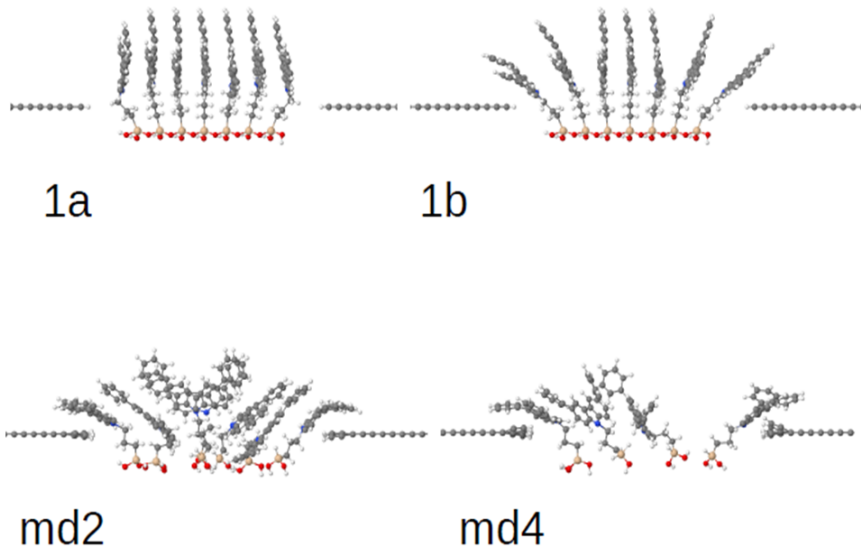


Figure 8.6: Graphene/molecule/graphene junctions: a-d show four example of molecular junctions formed by 7 molecules molecules between graphene electrodes.

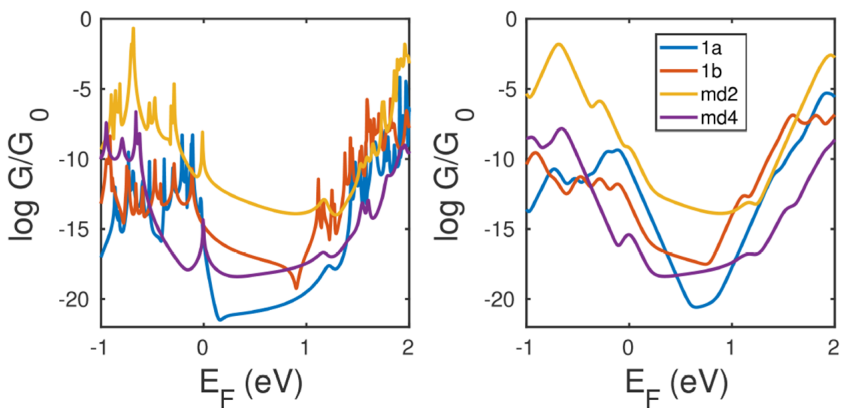


Figure 8.7: Conductance vs. Fermi energies: Conductance for different Fermi energies in the unit of G_0 for the junction in figure S8.6 respectively. Left/right panels correspond resp. to the conductance at zero/room temperature.

E3. Characterisation of an empty gap at different temperatures

After EB, the junctions were cooled down to 20 K. The junctions that showed tunneling current were characterized by recording 100 IV curves at every temperature. Figure.8.4 a), shows the mean IV curve calculated at the different temperatures from 20 to 300 K. All the IV curves showed a tunneling behavior and no significant effect of the temperature was measured. Fig.8.4 b) shows the evolution of the IV curves as a function of the temperature. The currents do not show any dependence on the temperature. Figure.8.4 c), confirms the weak effect of the temperature on the tunneling through the junction. Evolution of the logarithmic value of the current function of the temperature at different bias values is plotted. The evolution of the currents is constant over a the large range of temperature.

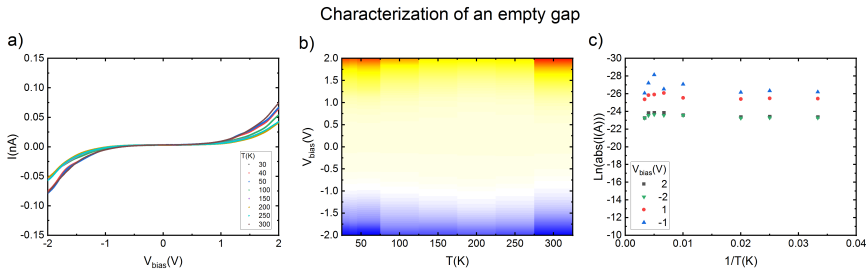


Figure 8.8: Characterization of an empty junction just after EB from 30K to 300K (a) Mean IV curves over 100 measured. (b) Evolution of the IV curves function of the temperature. (c) Evolution of the logarithmic value of the current function of the inverse of temperature at different bias values

E4. Fitting of the energies involved at different temperatures

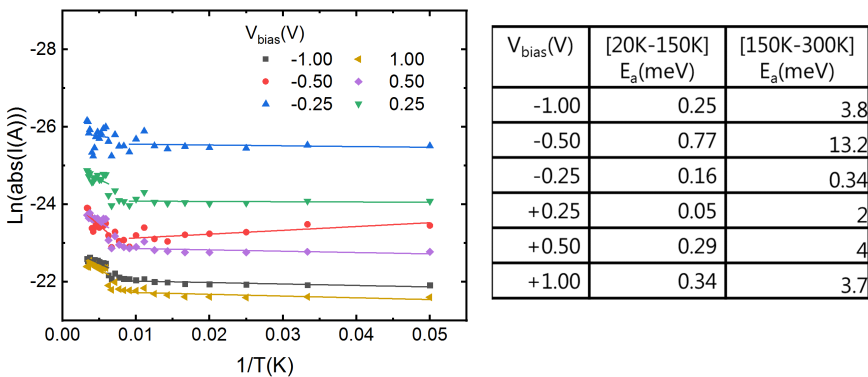


Figure 8.9: Device 1 Arrhenius plots of logarithm of the current versus $1/T$ (K^{-1}) at different bias voltages. The right panel shows the activation energies extracted for two regions: low (20K-150K) and high (150K-300K) temperatures.

Figure.8.9 presents the Arrhenius plot of the currents for fixed bias values. From this plot, activation energies are extracted by approximating the data with linear fits. According to

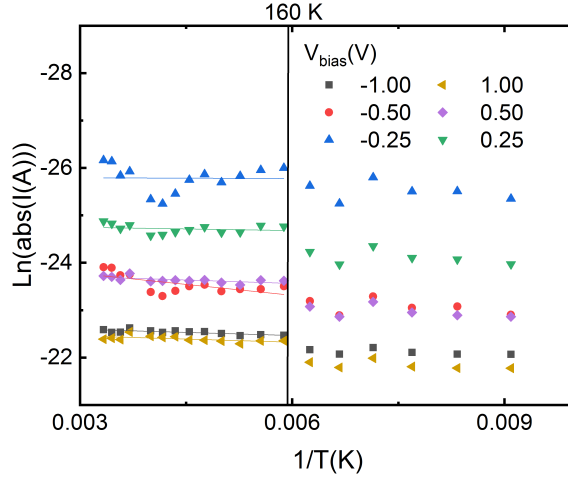


Figure 8.10: Device 1 Arrhenius plots of logarithm of the current versus $1/T$ (K^{-1}) at different bias voltages in the high temperature range (150-300K).

the Arrhenius formula, $\ln(I) = a \times T + b$, which can be rewritten as $I = \exp(a.T) \times \exp(b)$. The slope a of the fit is therefore proportional to the activation energy E_a of the mechanism, $E_a = a * k_b$. As the slopes are slightly higher for higher values of temperature, we have performed the fits for two regions separately, one below 160 K and one above. At 160 K, we can also observe a sudden decrease of current for all the bias voltage values. For both regions and all the bias values, we consistently obtain very small values for the activation energies, typically smaller than 1 to 10 meV. However, these values are just an estimate. From Figure 8.10, we can clearly see that the current in the high temperature regime is almost linear only for the high bias values. The extracted activation energies cannot be attributed to a uncoherent hopping mechanism that would typically exhibit energies higher than 50 meV (corresponding to the barrier between the different sites). The very weak dependence of the transport through the junction versus the temperature confirms that transport is dominated by coherent tunneling.

We have applied a Lorentzian fit to the resonance peak around 0.8V (Figure 8.11) to extract the full width at the half of the maximum (FWHM) of the Lorentzian. We have chosen this resonance peak because it is present for all three temperatures. In general, the width of a peak resonance, depending on the transport regime, depends on the thermal energy ($k_b T$), the intrinsic level broadening, and the coupling of the molecule to the electrodes (Γ). The values obtained from the fit are plotted in the right panel of Figure 8.11. The FWHM remains fairly constant between 20K and 150K and is equal to about 0.3 V. The peak gets broader at 300K where it reaches a value of 0.4V. From these observations, we conclude that the broadening of the peak is not only due to thermal effect.

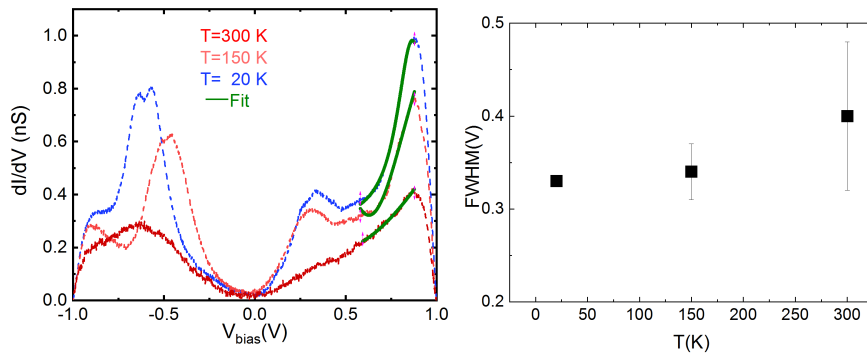


Figure 8.11: Device 1 Lorentzian fit of the differential conductance peak around 0.8V (only left side of the peak). c) Half of the peak width of the Lorentzian fitting at the three different temperatures. The width of the Lorentzian increases with temperature.

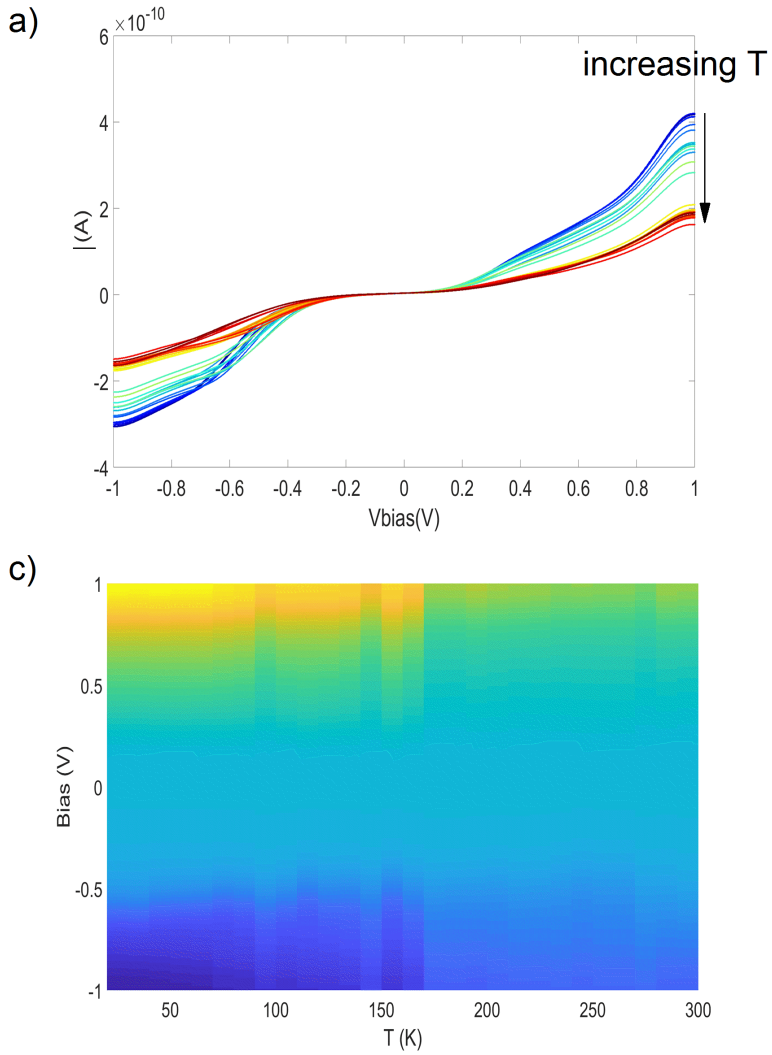
F5. Electronic transport at different temperatures

Figure 8.12: Device 1 a) Mean IV curve function of temperature. The red/blue color corresponds to the highest/lowest temperature. b) Evolution plot of the mean IV curve function of temperature.

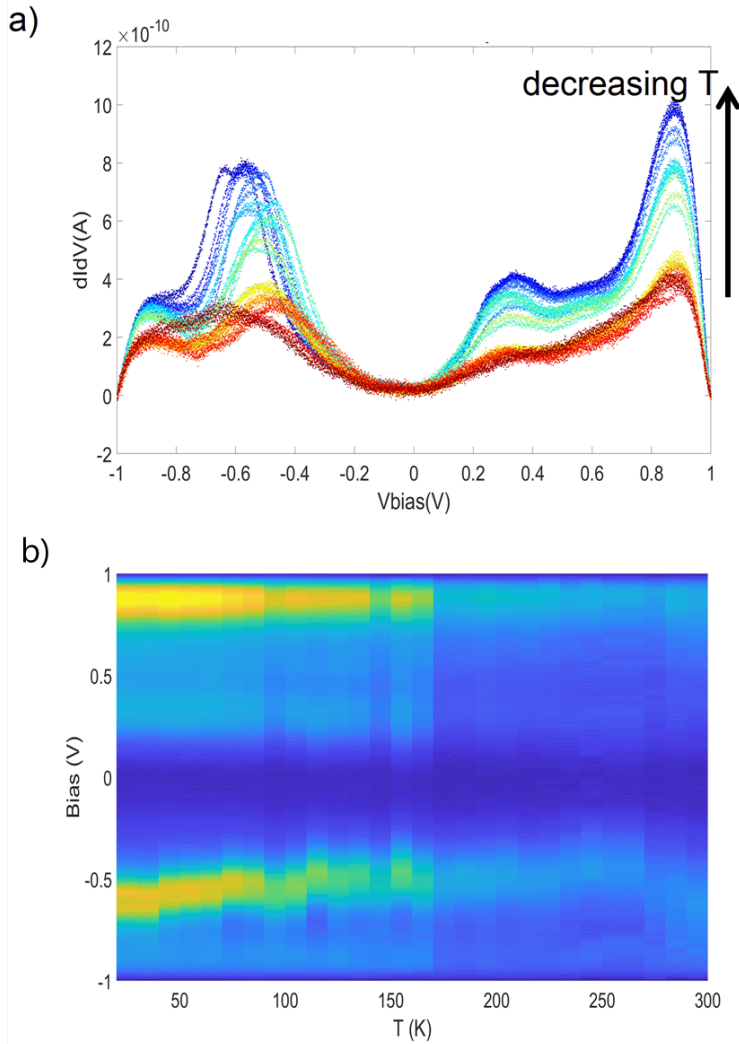


Figure 8.13: Device1 a) Mean dI/dV curve function of temperature. The red/blue color corresponds to the highest/lowest temperature. b) Evolution plot of the mean dI/dV curve function of temperature.

F.6. Fluctuations at different temperature

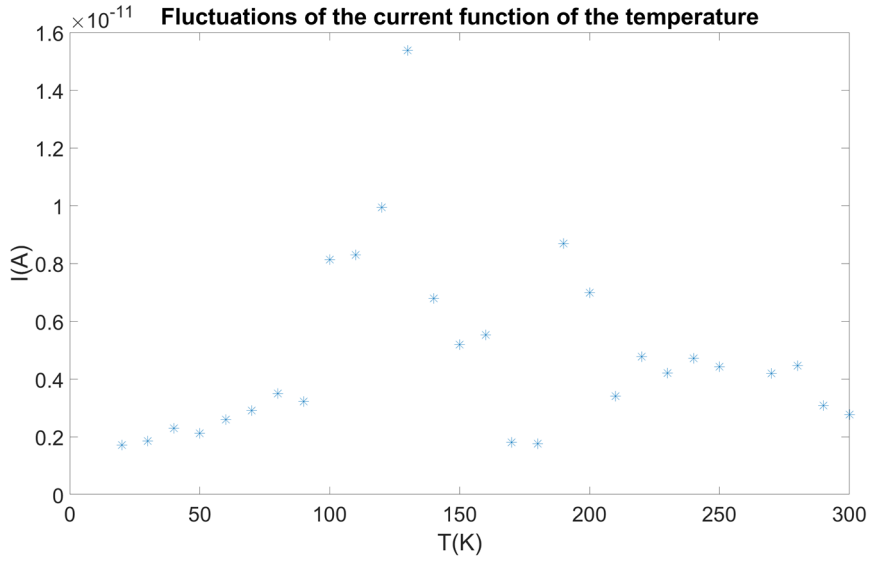


Figure 8.14: device 1 Fluctuations of current function of the temperature.

E.7. Device 1: IV curves at different temperatures

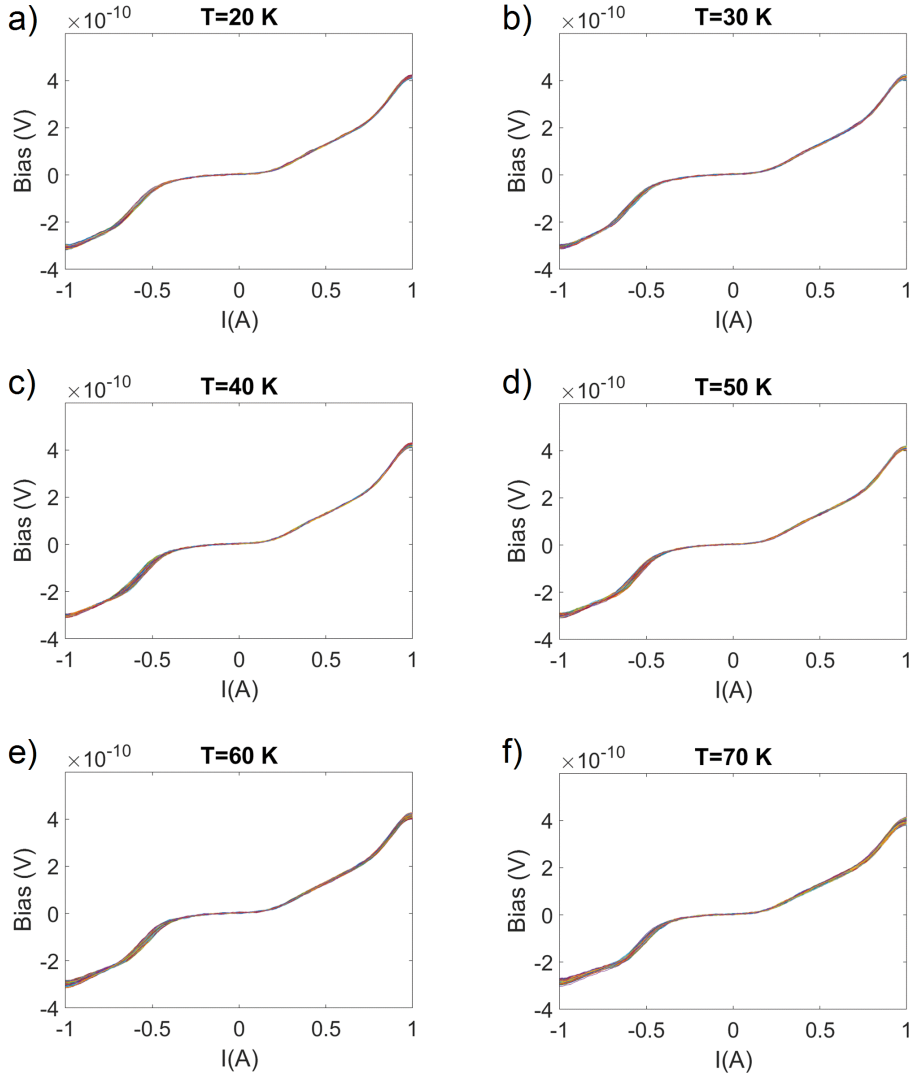


Figure 8.15: Device1 100 IV curves measured from T=20K to 70K.

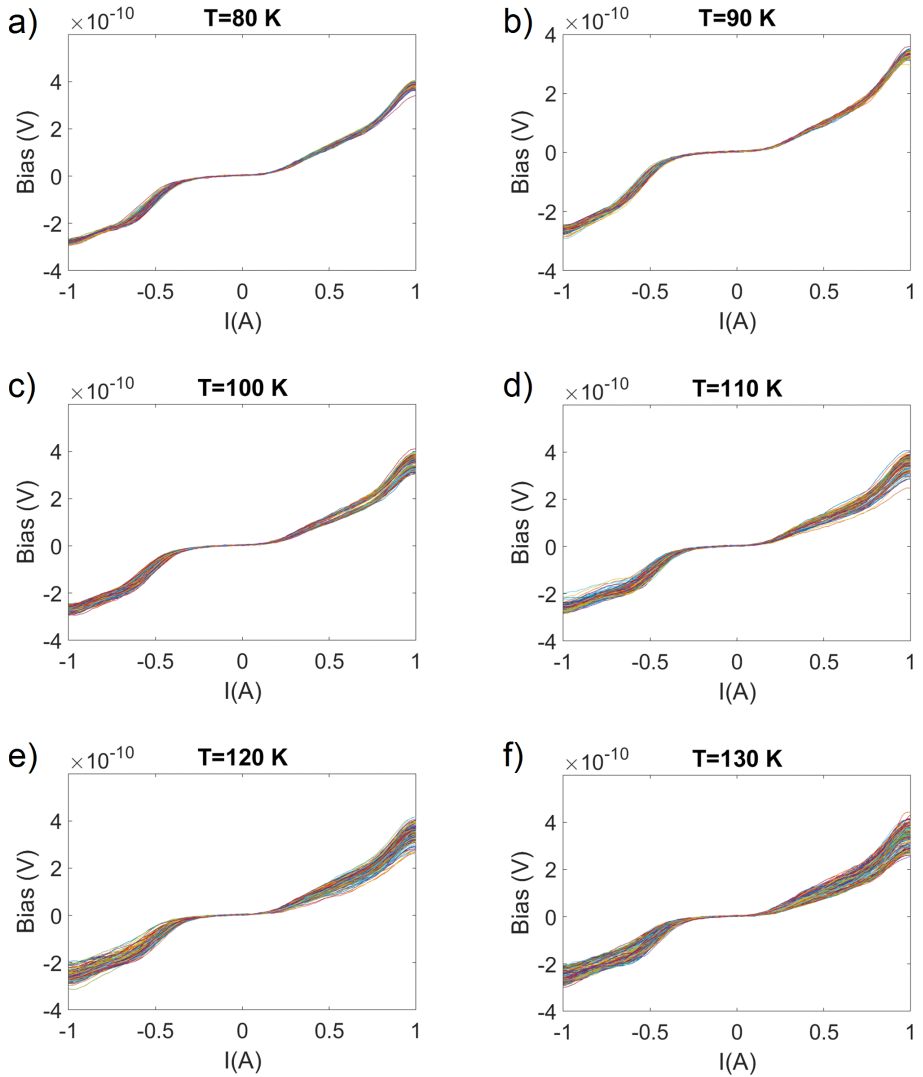


Figure 8.16: Device1 100 IV curves measured from $T=80$ K to 130K.

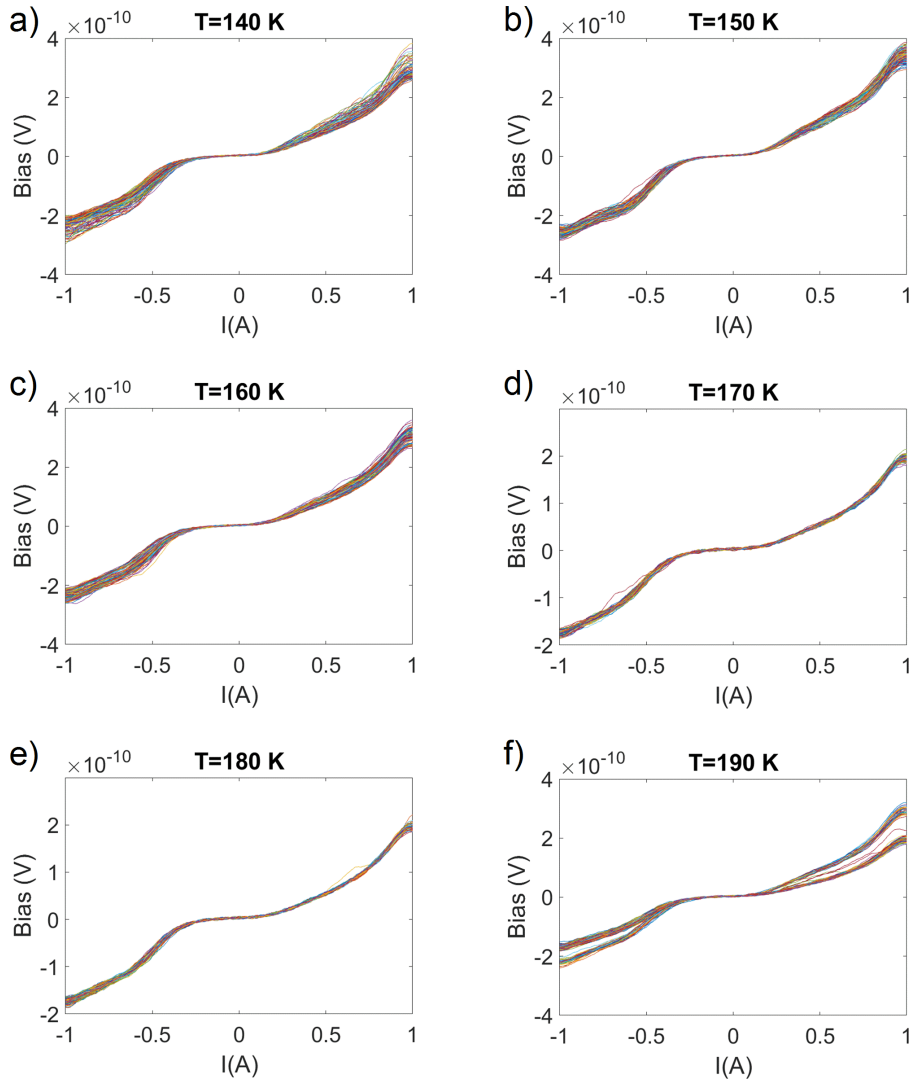


Figure 8.17: Device1 100 IV curves measured from $T=140$ K to 190K.

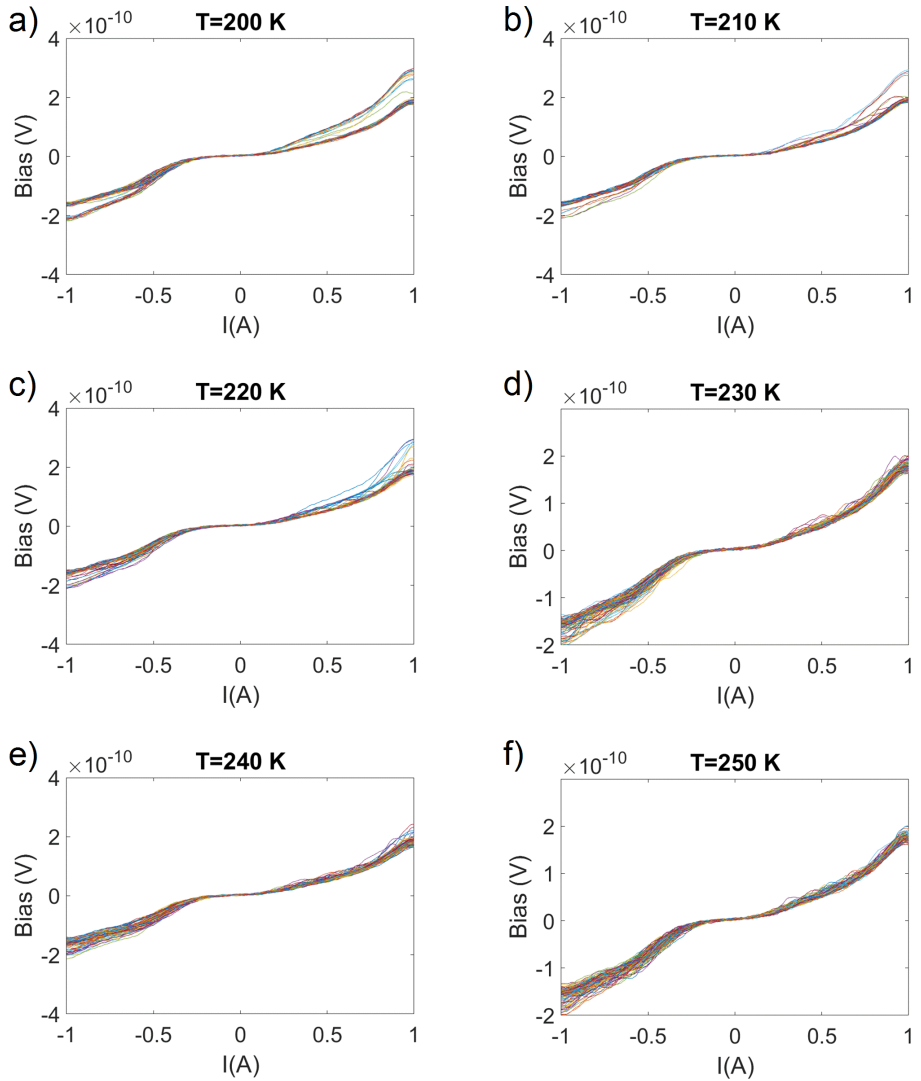


Figure 8.18: Device1 100 IV curves measured from T=200K to 250K.

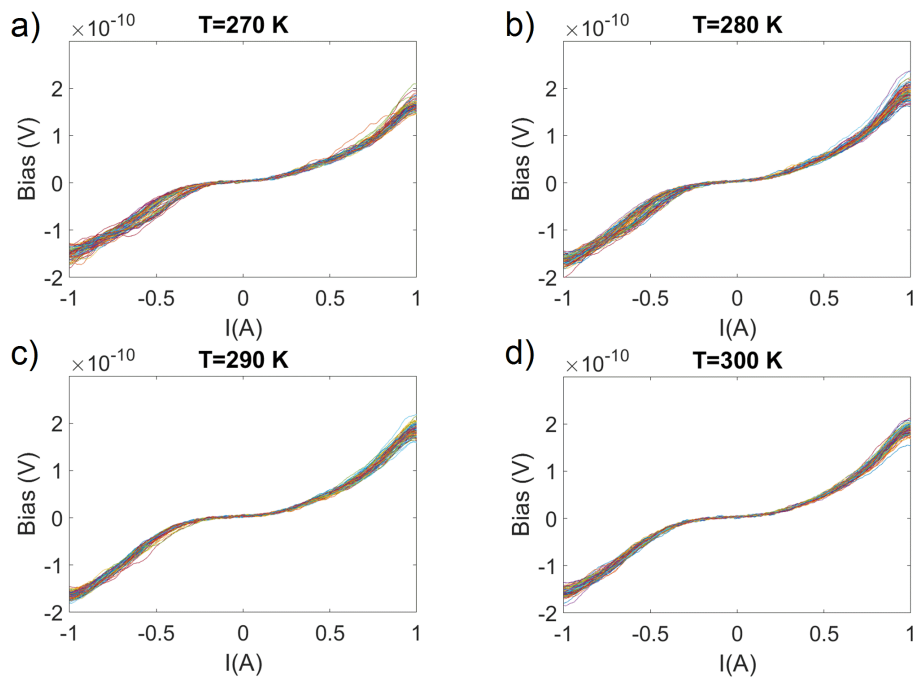


Figure 8.19: Device1 100 IV curves measured from $T=270$ K to 300K.

Graphene Nanoribbons



In this chapter, we report on the first preliminary measurements of Armchair-terminated 5 atoms-wide graphene nanoribbons (AGNR). We are still working on the analysis of these measurements. We use Raman spectroscopy to check the quality and the alignment of the GNRs film after transfer. Electrical characterization of the devices is performed at room temperature and at 13K.

9.1. Introduction

Due to their tunable electronic properties, Graphene Nano-Ribbons (GNR) are very promising building blocks for nanoelectronic applications. In particular, changing the width or the edge termination of a GNR results in different electronic, magnetic and optical properties [1, 2]. The most studied family of GNRs is the one with armchair edges, which is divided into three families, i.e., $N_a = 3p$, $N_a = 3p + 1$, and $N_a = 3p + 2$, where N_a is the number of dimer lines across the ribbon width and p an integer number. Each of these families possess specific bandgaps and level structure [1, 3]. For instance, tight binding calculations have predicted the $N_a = 3p + 2$ family to be metallic, while the two other families are semiconducting [3]. Major advances in bottom-up chemical synthesis allowed for the realization of ultra-narrow ($< 2nm$) graphene ribbons with atomic control [4–6]. Recently, the first high-performance field-effect transistors based on large bandgap 9 and 13 Armchair GNR (AGNR) were reported using metallic contacts, respectively from the $N_a = 3p$ and $N_a = 3p + 1$ family [7]. The $N_a = 3p + 2$ family, on the other hand, has only been investigated using scanning tunneling microscopy (STM) [8], demonstrating that 5-AGNRs show a quasi-metallic behavior and possess the smallest bandgap reported for GNRs so far (≈ 100 meV) in agreement with Density Function Theory (DFT) predictions. However, due to the short length of these ribbons, integration into devices remains challenging.

In this work, we use our sub-5nm graphene gaps (see Chapter 3 and 4) to contact 5 AGNRs. At room temperature, the devices show a metal-like behavior with a linear low-bias conductance. The device yield is about 100%. At lower temperature, single electron tunneling and coulomb blockade phenomena are observed with addition energies lower than 200 meV.

9.2. Synthesis and Transfer of the GNRs

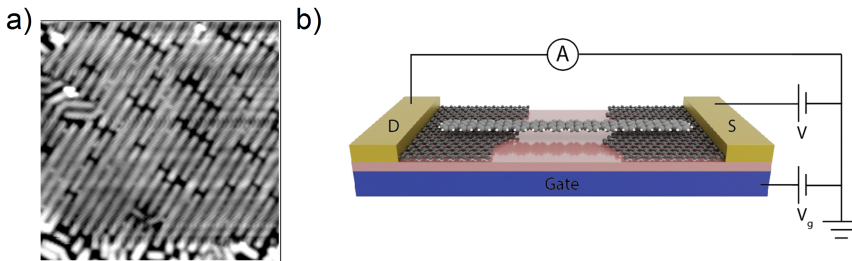


Figure 9.1: Junction Geometry (a) High resolution STM image of synthesized 5AGNR on Au ($V_s = -1.5V, I_t = 0.06nA$) (b) Schematic of the 5AGNR bridging a graphene nanogap.

Chemical vapor deposition (CVD)-grown graphene is transferred onto a Si substrate with 285 nm of thermally grown SiO_2 . The graphene films are patterned into 400 nm wide stripes using reactive ion etching combined with an e-beam lithography defined PMMA etch mask. In a subsequent e-beam lithography step, metallic contacts (5nm Cr / 45 nm Au) are patterned and deposited using e-beam evaporation. Finally, nanogaps are formed in the

graphene stripes using the EB technique [9, 10], (see Chapter 3).

The bottom-up synthesis of aligned 5-AGNRs was carried out in ultra-high vacuum via sequential on-surface chemical reactions. In a first step, the precursor molecule dibromopyrene was sublimated at 160°C onto an Au(788) surface kept at room temperature. A slow annealing process ($0.2^{\circ}\text{C}/\text{s}$) up to 225°C allowed the monomers to polymerize followed by cyclode-hydrogenation. The later causes the polymer phase to planarize and form the ribbons. The high quality and degree of alignment of 5-AGNRs was verified by high-resolution scanning tunneling microscopy (STM), Figure 9.1.a). Growing aligned ribbons allow us to have GNRs oriented along the source-drain direction and therefore increase the possibility of bridging GNRs between the electrodes. In order to integrate GNRs into the graphene junctions an electrochemical delamination transfer process (or bubble transfer) was employed. This transfer method preserves both the structural quality and uniaxial alignment of the ribbons [2]. As a first step to carry out the electrochemical delamination of GNRs from the Au (788) surface, poly(methylmethacrylate) (PMMA) was spin-coated on the Au surface to be used as a support layer for the GNRs during the transfer. An aqueous solution of NaOH (1M) was employed as electrolyte in the electrochemistry process and a DC-voltage was applied between the PMMA/GNR/Au cathode and a glassy carbon electrode used as anode. During this process, water undergoes reduction resulting in hydrogen bubbles emerging at the GNR/Au interface. The H_2 bubbles provide enough force to detach the GNR film from the Au surface, starting from the edges and followed by the permeation of the electrolyte solution into the interface as the edges delaminate. The GNR/PMMA film is then transferred onto the graphene device using a wet-transfer technique. After transfer, the sample is heated to 150°C for 15 minutes and the PMMA is dissolved in acetone. A schematic of the device where a ribbon is bridging the graphene nanogap is presented in Figure 9.1.b).

9.3. Raman characterisation

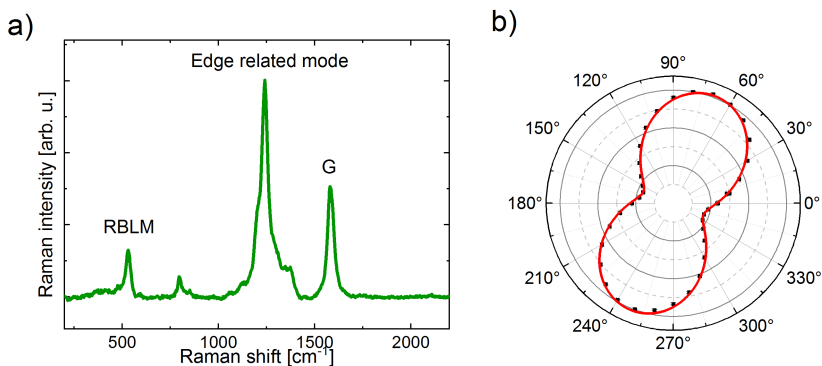


Figure 9.2: Raman characterization after transfer (a) Raman spectra of as-transferred 5AGNR. The characteristic radial breathing like mode (RBLM, 532 cm^{-1}), an edge related mode ($\approx 1240\text{ cm}^{-1}$) and the G-mode ($\approx 1600\text{ cm}^{-1}$) are clearly visible. (b) The Raman intensity of the G-mode as a function of the polarization of the excitation laser. The data are following a $\cos^2(\theta)$ dependence (red).

Polarized Raman spectroscopy is performed after transfer to verify the quality and the

degree of orientation of the GNRs. Figure 9.2.a) presents a Raman spectra of a as-transferred 5GNR film. The characteristic radial breathing like mode (RBLM, 532 cm^{-1}), an edge related mode ($\approx 1240\text{ cm}^{-1}$) and the G-mode ($\approx 1600\text{ cm}^{-1}$) are clearly visible [11]. This confirms that the film quality is preserved after transfer. To check the alignment of the GNRs, we have performed polarization dependent Raman measurements. Figure 9.2.b) shows the dependence of the G mode Raman intensity on the angle of polarization of the exciting laser on a transferred nanoribbon film. We observe a strong polarization anisotropy with the maximum Raman intensity measured along an axis forming an angle of 60° with the y axis. This agrees with the expected ribbon axis as determined by the orientation of terraces on the Au(788) growth substrate, proving that the ribbons maintain their alignment after transfer.

9.4. Room temperature measurements

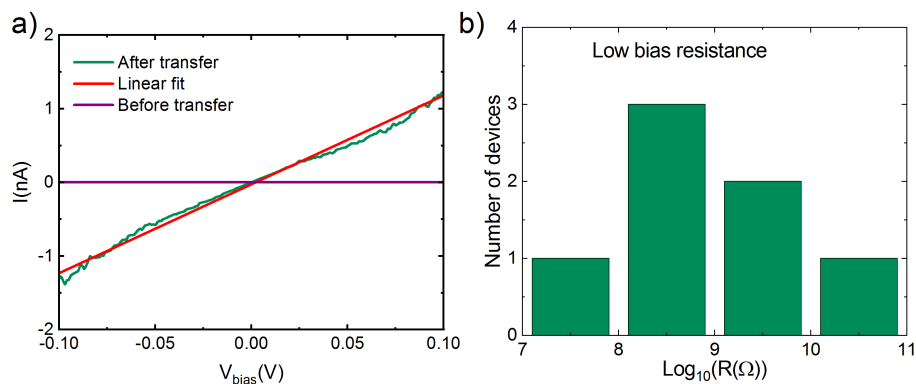


Figure 9.3: Electrical characterization at room temperature (a) Typical IV curve measured before and after transfer of the ribbons (are shown in purple and green respectively). The red line corresponds to a linear fit of the IV curve. (b) Histograms of the low bias resistance measured for all the devices.

After the GNR transfer, electrical characterization was first performed at room temperature. Figure 9.3.a presents typical IV curves measured before and after transfer. While before transfer no current is measured in the $[-0.1, 0.1]\text{V}$ low bias voltage range, a linear IV curve with currents in the nA regime is measured after transfer. This behavior was observed for all 7 devices investigated at room temperature. A linear fit (red line) was performed to extract the corresponding linear conductance. Figure 9.3.b) presents the histogram of the fitted low-bias resistance values. A large distribution of resistances is measured (from 10 to 10000 $\text{M}\Omega$) with a maximum around 100 $\text{M}\Omega$. The observed device-to-device variations can be attributed to differences in the number of ribbons bridging the gap and/or the overlap between the ribbon and the graphene electrodes.

9.5. Low temperature measurements

To perform spectroscopy of the energy levels of the GNRs, devices were cooled to 13 K, of which Fig. 9.4 presents two examples. We have measured the dependence of the charge

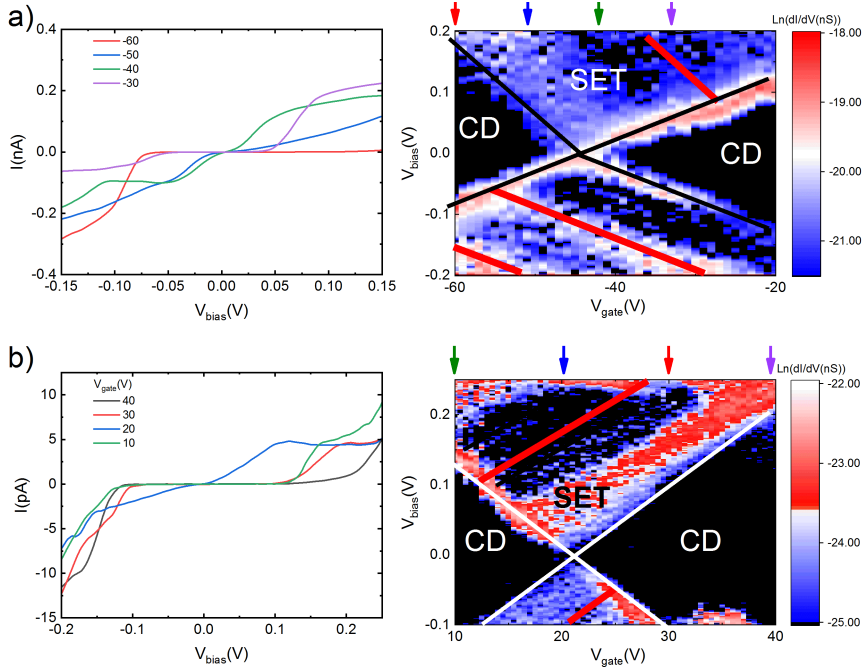


Figure 9.4: Electrical characterization of two different devices at 13K (a) IV curves at different gate values. (b) Differential conductance maps (stability diagrams) of 5GNR bridging two graphene electrodes. CD corresponds to the Coulomb diamond and SET to the single-electron tunneling. White lines indicated the Coulomb diamonds edges. Excitations highlighted by red lines are attributed to vibrational and/or electronic modes.

transport on the bias and gate voltage. The left panel present IV curves obtained at different gate voltages. Both devices exhibit a suppression of the conductance near zero bias voltage and a step-like increase in current for higher bias voltages, the position and height of which is tunable with gate voltage (V_g). The right panel displays the evolution of the differential conductance dI/dV with gate, plotted as a so-called stability diagram. In this graph, we can observe different regions with different transport properties corresponding to a single electron transistor behavior (SET). In the following, we will use the formalism developed in the reference [12]. In a resonant tunneling picture, the GNR is equivalent to a island with a capacity C_{dot} that is coupled to the graphene via tunnel barriers. In the black region around 0 bias voltage, no current is passing through the devices. It is called the blocking region. At low enough temperatures and small bias voltage, the energy required to add an extra electron onto the island exceeds the thermal energy and the current through the island is blocked. The blocking region corresponds to a diamond shape area and it is called a Coulomb diamond (CD in the Fig. 9.4). Half of the height of the diamond corresponds to the addition energy required to add an electron to the single electron transistor. Table.9.1, lists the different additions energies measured for all the devices. We could measure two main sizes of diamonds with energies about 50-80meV and 100-200 meV. In the case of a molecule, this energy is related to the quantum confinement and the Coulomb charging energy. Depending on the relative level alignment and the position of the Fermi energy,

the addition energies that we have measured can correspond to the GNR HOMO-LUMO bandgap.

From the stability diagram, we can also extract smaller excitations due to vibrational and electronic excitations in the sequential-tunneling regime. The sequential tunneling regime corresponds to the region where the dI/dV is zero but the current is not (SET region in Fig. 9.4). This happens when the level of the dot is aligned with the Fermi energy of one of the electrode. Inside these regions, we can observe the presence of peaks in the dI/dV that are parallel to the Coulomb diamonds (CD) edges. In the right panels of Figure 9.4, these excitations are highlighted with red lines. It corresponds to electronically or vibrationally excited states of the ribbons that create a transport channel. The energy of these excitations can be extracted from the graph by measuring the intersection between the excitations lines and the edge of the CD. For all the devices, we measured excitation energies between 40 and 70 meV. The width of these excitations lines depend on the thermal energy $k_b T$ and the coupling of the ribbon to the graphene leads Γ . Some of the resonances are asymmetric, which may be attributed to the coupling to the source or drain electrodes being asymmetric as a result of the overlap between the ribbon and the two leads.

From the measurements, we can conclude that the 5GNR acts as a weakly coupled island to the graphene leads. However, the injection of electrons charges from the reservoir is not fully clear so far and may occur at the edge of the ribbon or over the whole region where the ribbon overlap with the graphene leads. Using a simple capacitive model may help to estimate the effective size of the dot and thus the coupling area. We are currently working on this.

Estimating the size of dot will also help to compare the addition energies extracted from the different junctions to the HOMO-LUMO gap of a 5-AGNR. DFT calculations have predicted that the HOMO-LUMO gap of a 5-AGNR depends significantly on the ribbons length [8]. These predictions have been confirmed experimentally using the STM technique [8]. By estimating the size of our dot, we should be able to compare the extracted addition energies to the HOMO-LUMO bandgap of the 5-AGNRs. Recent work by Jan Overbeck is aiming to characterize the length of the GNRs using length-dependent Raman modes.

The interaction with the graphene electrode can also lead to states that interfere with the SET properties. Gehring et al. [13], have proven that graphene leads may add excitational level in the sequential tunneling regime. Quantum interference within the graphene leads gives rise to an energy-dependent transmission and fluctuations in the sequential tunnel-rates. However the pattern of such excitations is different from the one resulting from the island. The excitations lines from the leads are not parallel to the edge of the CD. In our case, all the excitations are parallel to the edge of the CD, confirming that the extracted excitation energies are a signature of the molecule. These excitations can correspond to electronic or vibrational modes. We are trying to estimate the energy of the vibrational modes using Raman spectroscopy.

9.6. Conclusion

To conclude, we have investigated the transport through a graphene-5GNR-graphene junction. At room temperature, we observed linear IV curves. This indicates that the bandgap of the 5GNR is very small, in good agreement with DFT calculations and STM measurements. At

Table 9.1: Measured addition and excitation energies at 13K.

Device	E_{add1} (meV)	E_{add2} (meV)	E_{ex} (meV)
1	50-83	100	40-70
2	70	140	70
3	55	240	80
4	50	220	50-60
5	35-80	140	40
6	60	220-310	40
7	50	100-150	40
8	50	130	40
9	40	130-180	70

13K, we observed single electron transistor behavior, which addition energies of about 100 meV, in good agreement with the predicted bandgap of a 5GNR [8]. Moreover, we observed excited states with energies around 40-50 meV. Those measurements are preliminary results and the analysis is still in progress.

Contributions This chapter is part of a manuscript under preparation. Oliver Braun made the sample. Gabriela Borin Barin the synthesis of the GNRs. Maria El Abbassi conducted the measurements. Mickael Perrin made the schematic picture. Jan Overbeck performed the Raman measurements.

Bibliography

- [1] Li Yang, Cheol-Hwan Park, Young-Woo Son, Marvin L. Cohen, and Steven G. Louie, Quasiparticle Energies and Band Gaps in Graphene Nanoribbons newblock *Physical Review Letters*, 99:186801, 2007
- [2] B.V. Senkovskiy, M. Pfeiffer, S.K. Alavi, A. Bliesener, J. Zhu, S. Michel, A.V. Fedorov, R. German, D. Hertel, D. Haberer Making Graphene Nanoribbons Photoluminescent *Nano Letters*, 17 (7): 4029–4037,2013
- [3] Young-Woo Son, Marvin L. Cohen, and Steven G. Louie Energy Gaps in Graphene Nanoribbons *Physical Review Letters*, 97: 216803,2006.
- [4] Yen-Chia Chen, Dimas G. de Oteyza, Zahra Pedramrazi, Chen Chen, Felix R. Fischer, and Michael F. Crommie. Tuning the Band Gap of Graphene Nanoribbons Synthesized from Molecular Precursors *ACS Nano*,7 (7): 6123–6128, 2013.
- [5] Jinming Cai, Pascal Ruffieux, Rached Jaafar, Marco Bieri, Thomas Braun, Stephan Blankenburg, Matthias Muoth, Ari P. Seitsonen, Moussa Saleh, Xinliang Feng, Klaus Mullen and Roman Fasel Atomically precise bottom-up fabrication of graphene nanoribbons *Nature*, 466: 470–473,2010.
- [6] Pascal Ruffieux, Jinming Cai, Nicholas C. Plumb, Luc Patthey, Deborah Prezzi, Andrea Ferretti, Elisa Molinari, Xinliang Feng, Klaus Müllen, Carlo A. Pignedoli, and Roman Fasel. Electronic Structure of Atomically Precise Graphene Nanoribbons *ACS Nano*, 6 (8):6930–6935, 2012.
- [7] Juan Pablo Llinas, Andrew Fairbrother, Gabriela Borin Barin, Wu Shi, Kyunghoon Lee, Shuang Wu, Byung Yong Choi, Rohit Braganza, Jordan Lear, Nicholas Kau, Wonwoo Choi, Chen Chen, Zahra Pedramrazi, Tim Dumsflaff, Akimitsu Narita, Xinliang Feng, Klaus Mullen, Felix Fischer, Alex Zettl, Pascal Ruffieux, Eli Yablonovitch, Michael Crommie, Roman Fasel and Jeffrey Bokor Short-channel field-effect transistors with 9-atom and 13-atom wide graphene nanoribbons *Nature Communications* 8: 633, 2017.
- [8] Amina Kimouche, Mikko M. Ervasti, Robert Drost, Simo Halonen, Ari Harju, Pekka M. Joensuu, Jani Sainio and Peter Liljeroth. Ultra-narrow metallic armchair graphene nanoribbons *Nature Communications* 6: 10177, 2015.
- [9] Cornelia Nef, László Pósa, Péter Makk, Wangyang Fu, András Halbritter, Christian Schönenberger, and Michel Calame. High-yield fabrication of nm-size gaps in monolayer cvd graphene. *Nanoscale*, 6(13):7249–7254, 2014.

- [10] Maria El Abbassi, László Pósa, Péter Makk, Cornelia Nef, Kishan Thodkar, András Halbritter, and Michel Calame. From electroburning to sublimation: substrate and environmental effects in the electrical breakdown process of monolayer graphene. *Nanoscale*, 9(44):17312–17317, 2017.
- [11] Zongping Chen, Hai I. Wang, Nerea Bilbao, Joan Teyssandier, Thorsten Prechtel, Nicola Cavani, Alexander Tries, Roberto Biagi, Valentina De Renzi, Xinliang Feng, Mathias Kläui, Steven De Feyter§, Mischa Bonn, Akimitsu Narita, and Klaus Müllen. Lateral Fusion of Chemical Vapor Deposited N = 5 Armchair Graphene Nanoribbons *JACS*, 139(28):9483–9486, 2017.
- [12] J. M. Thijssen, and H. S. J. Van der Zant. Charge transport and singleelectron effects in nanoscale systems *Physica status solidi b*, 245(8):1455–1470, 2008.
- [13] Pascal Gehring, Jakub K. Sowa, Jonathan Cremers, Qingqing Wu, Hatef Sadeghi , Yuewen Sheng , Jamie H. Warner , Colin J. Lambert , G. Andrew D. Briggs, and Jan A. Mol. Distinguishing Lead and Molecule States in Graphene-Based Single-Electron Transistors *ACS Nano*, 11(6):5325-5331, 2017

Conclusion

This dissertation describes our recent efforts on the electrical characterization of graphene-based molecular junctions. The properties of the junctions depend on both the graphene nanogap characteristics and the molecular structure. In this thesis, we study the different steps of making graphene-based molecular junctions.

In the first part of the thesis, we describe the fabrication and characterization steps to prepare the electrode material. We use the chemical vapor deposition technique to produce high quality large-area graphene. Several steps of e-beam are required to make devices that are systematically characterized using Raman and electrical techniques to check the quality and the cleanliness of the electrode material. The nanogaps are formed by electrical breakdown of graphene. We show that depending on the density of oxygen molecules available, we oxidize or sublime the graphene. We demonstrate that the sublimation regime (performed in vacuum) leads to higher yield of gap formation.

The second part of the thesis explains the details of the characterization of the nanogaps. This step is crucial before the molecular deposition can occur. Leftover of carbon atoms or partially destroyed silicon oxide may exhibit electrical features similar to the signature of a molecule. A full characterization of the nanogaps is therefore essential to select the *clean* gaps.

In the last part, we present the different possibilities of anchoring molecules to the graphene leads. We show that $\pi-\pi$ stacking might be the right approach to attach molecules to the graphene leads. However, a weak interaction with the electrodes is not enough to mechanically stabilize the junctions at room temperature. We show that combining a covalent binding to the substrate, using silanization, and a π overlap to the electrodes is very promising. Based on this approach, we demonstrated the realization of a mechanical and electronical stable junction from 20K to 300K. Finally, we performed measurements on graphene nanoribbons. Three ribbons with different atomic widths (5, 7 and 9 atoms wide) were explored. They showed very different electrical behavior: a semi-metallic behavior for the 5GNRs and a semi-conducting electrical characteristic for the 7 and 9 GNRs. The high electrical tunability of the properties of the GNRs makes them very interesting nano-compounds that have to be further investigated in a perspective of a device application.

Graphene-based molecular junctions are very promising platforms to study nano-objects like molecules or ribbons. Nevertheless, one has to be extremely careful with the characterization of these junctions. Contaminations from the several fabrication steps can interfere with the signatures of the measured molecules. Moreover, several questions remain open like the effect of the chemical and crystallographic termination of the nanogap-edge, the influence of defects at the edge of the graphene leads. To gain more understanding of these devices, complementary techniques, like thermopower measurements and Raman spectroscopy for example, should be used to understand in more details electron and phonon transport.

Acknowledgement

Now comes the part that took me almost a year to write!

First, I would like to thank Colin Lambert, Dominique Villaume et Tim Albrecht for being part of my thesis committee. It was a great pleasure to discuss the content of my thesis with you and I am looking forward to future collaborations.

Michel! Je tiens à vous remercier pour tout. Merci de m'avoir enseigné la rigueur et la précision. Vous êtes une source d'inspiration! Je n'oublierais jamais nos meetings durant lesquels vous aviez tellement d'idées bien évidemment 'very challenging' mais tout aussi nouvelles et révolutionnaires! J'espère que vous partagerez cela avec les générations à venir! Quelques rares personnes durant notre parcours arrivent à changer le cheminement de celui-ci et dans mon cas je pense que vous avez contribué à tracer une voie nouvelle. Ces 4 années n'ont pas été faciles! J'ai fait partie des étudiants qui ont du vivre en plein milieu de leur thèse le déménagement à l'EMPA. Je ne pourrais pas dire que ça a été facile, étant donné que j'étais aussi parmi les plus réticents à ce changement. Cela dit avec du recul, je vous remercie d'avoir pu rester ferme et en même temps nous avoir tous impliqués pleinement dans cette transition qui s'est finalement très bien passée. Nos chemins se croiseront bien évidemment dans le "quiet" futur. Donc à bientôt!

Super Mika, le grand frère. Merci d'avoir fait de cette thèse ce qu'elle est aujourd'hui. En plus d'être le collègue avec qui on a eu beaucoup de discussions sur la physique, les clusters, les molécules.. tu es le pote qui partage l'amour de Soprano et du fromage! Encore merci pour tout le savoir et la bonne humeur que tu peux transmettre autour de toi! Merci de m'avoir soutenue et boustée jusqu'au bout! Tu es un scientifique mais aussi une personne exceptionnelle et je te souhaite tout le meilleur du monde pour ton futur! J'espère que nos collaborations à propos de nos amies les molécules se poursuivront bien longtemps. And thank you to the angel that shares your life (Asja) for her good humor and very nice raclettes at your place! All the best to your future family!

Barbara, the angel of the department. Many thanks for being what you are. Without you, this thesis would not have been possible. Your presence and support were crucial! I will never forget the angel of Basel! Many thanks again! Danke weil mal...

Christian Schoenenberger, thank you for your support! You are an impressive scientist with an incredible knowledge of the field! You were the person that made me like experimental physics. People with your knowledge and management skills are very rare and I am very happy that I could spend a few months in your lab.

Anton thanks for being the friend, the brother, the one who listens, helps, and supports! I am really happy that I could enter your world! You are an impressive and very kind person! Thank you for your support, our math discussions, the latte machiatos and the list is long... I am pretty sure you will be successful in whatever you will do and that we will keep in touch.

Axelounette, mon confident avec qui je partage l'amour de râler! Nos chemins se sont séparés trop rapidement, mais je suis reconnaissante au destin d'avoir rencontré un ami français scientifique! Une personne avec un coeur en or et qui râle peut être autant que moi. Merci énormément d'avoir été l'ami très proche de ma thèse. Nos longues discussions me manquent énormément! Beaucoup de bonheur dans ta nouvelle vie loin de labos !

Jan and Luisa, my colleague and my friend! Jan, mon grand Jan! Merci d'avoir écouté, discuté et en même temps ammené de la bonne humeur et de la rigueur à ce groupe. Une personne passionnée et brillante qui a beaucoup ammenée au groupe! Many thanks to you Jan for your scientific rigor, for your good humor and spirit! Un fin gourmet with whom every single experience of life becomes very scientific and philosophical! And Luisa, you are an amazing person! I am so glad I met you and could see you from time to time when you were visiting us in Basel. I discovered a big heart, a very helpful person that made many of my days full of joy and craziness! Thanks again guys! And looking forward to seeing soon in

...

Oli, mon petit Oli. Merci d'avoir été le petit frère avec qui la science a été beaucoup plus Suisse. Tu es un bon gars avec beaucoup de valeurs et de rigueur. Je te souhaite tout le succès du monde pour ta thèse et ta vie personnelle.

Valentin, mon petit Belge. Partager ces quelques de mois de labo avec toi ont été formidables. Bon vent pour ta nouvelle vie dans le pays des frites.

Roomies, many thanks to my roomies for sharing offices and many many tea breaks. Ralph, Matthias, Kishan, Lena, Yves, Masoud, Sahana! The PhD life would not have been so fun without you guys! Matthias and Ralph, my two Swiss boys! I wish you all the best with your kids and wives! It was a great pleasure to have both of you around and profit from your knowledge! Le beau Matthias many thanks again for reading this PhD. Kishan, our graphene man! Your passion for science cooking is impressive! All the best for your future that I am pretty sure will be very successful! Peter Makk, many thanks for teaching me the basics of experimental physics and your help and support with the papers! You are a great scientist! All the best in Budapest. WangYang! You sent me an email about this position! Many thanks for your support, kindness and guidance! You are one of the most amazing postdocs I met! All the best with your new position in China.

Coolies: Gulbostan, Raphaele, Simon, Clevin, Lujun, Christian, Vishal, Cesar, MingJung, Andreas, Peter Rickhaus, Andreas. It was a pleasure to share the group excursions and lunch breaks with you! People from EMPA, Lorenzo, Roman, Arno, and everybody... You were the best hosts at EMPA. I sincerely enjoyed joining your group events!

I think that this experience will not have been the same without the Molesco adventure. So thank you for all the Molesco people for the fruitful discussions and pleasant meetings! During this project, I could also discover a new lab. Thank you Herre for accepting me in your lab for few months secondment and now for a bit longer as a postdoc. Max, the interactions with you were always passionate and interesting! Thanks for sharing with me your experience with molecules! Alexandra and Vicky, two wonderful women! You are such an amazing and strong person. Davide thanks for coming to Basel for my defense and all the fun moments at the conferences!

A big thanks to Hatef and Sara, the two theoreticians of this thesis. Many thanks for your DFT calculations, the nice discussions and hosting us so well in Lancaster! Many thanks again for everybody! And looking forward to our future collaborations.

Aurore, une de mes plus grandes découvertes à l'ENS Paris. Une personne en or et une

scientifique exceptionnelle. Beaucoup de succes pour ton future!

Je tiens aussi a remercier des personnes qui m'ont énormement soutenu dans des moments critiques de ma vie et qui m'ont fait confiance. Un grand merci donc à Jean Francois Allemand de l'ENS Paris d'avoir été plus qu'un professeur, merci à Johann et Maria Bartel et á mon grand Panda. Merci à mes amis Aleta, Aurore, Houda Sami et Rayan, Jetsa, Celine, Moha, Selma et famille, et toutes les personnes qui ont partagé ma vie ces dernieres années.

Et pour finir, j'aimerai remercier ma famille. Merci à vous tous! Tout d'abord, je tiens a dédier cette thèse a deux personnes qui nous ont quittées trop tôt et qui je pense aurait été fier de voir leur fille finir cette thèse. Hbibì et Hbibti, twehechnakom bezaaaf o baraktom tkone m3ana. Puis vient Titifti, tu es la lumière qui me guide dans tout mes choix. Merci d'être ce que tu es, une personne incroyable. Grand chef, merci de nous avoir communiqué ta passion et ta bonté. Mimih, je sais que nos relations ne sont pas les meilleurs du monde mais je suis fière de toi petit fr ère de ce que tu deviens. Nouina, Mani, Adjia, Sara, Adafim, Sara, Hamouda et SiBaba, sans vous je ne suis rien! Merci à toute ma famille!

Et un grand merci à toute personne qui a compté dans ma vie et que j'ai oubliée de mentionner.

Publication list

Journal articles

1. W.Fu, **M. El abbassi**, T. Hasler, M. Jung, M. Steinacher, M. Calame, C. Schonenberger, G. Puebla-Hellmann, S. Hellmuller, T. Ihn, and A. Wallraff, *Electrolyte gate dependent high-frequency measurement of graphene FETs for sensing Applications*, App.Phys.Lett 104, 013102 (2014).
2. K. Thodkar, **M. El abbassi**, F. Luond, F. Overney, C. Schonenberger, B. Jeanneret, and M. Calame, *Comparative study of single and multi domain CVD graphene using large-area Raman mapping and electrical transport characterization*, PSS- RRL, 10(11), 807-811 (2016).
3. **M. El abbassi**, L. Posa, P Makk, C. Nef, K. Thodkar, A. Halbritter, and M. Calame, *From Electroburning to Sublimation: Substrate and Environmental effects in the Electrical Breakdown Process of Monolayer Graphene*, Nanoscale,9, 17312-17317 (2017).
4. L. Posa, **M. El abbassi**, P Makk, B. Santa, C. Nef, M. Csontos, M. Calame, and A. Halbritter, *Multiple physical timescale and dead time rule in few-nm sized graphene-SiOx-graphene memristors*, Nano letters 17 (11), 6783–6789 (2017).
5. M. V. Rastei, A. D. Craciun, **M. El abbassi**, M. Diebold, P Cotte, O. Ersen, H. Bulou, and J. L. Gallani, *Anisotropic Failure of sp²-Hybrid Bonds in Graphene Sheets*, submitted.
6. **M. El abbassi**, S. Sangtarash, M. Perrin, H. Sadeghi, H. V. D. Zant, S. Yitzchaik, and M. Calame, *Silanization as a statistically robust approach for anchoring molecules between graphene electrodes*, submitted.
7. VM. García-Suárez, A. García-Fuente, D. Carrascal, M. Koole, E. Burzuri, H. S. J. van der Zant, M. El Abbassi **M. El abbassi**, M. Calame, and J. Ferrer, *Spin signatures in the electrical response of graphene nanogaps*, to be submitted.
8. **M. El abbassi**, X. Liu, S. Sangtarash, M. Perrin, H. Sadeghi, S. X. Liu, C. Lambert, S. Decurtins, and M. Calame, *Reproducible mechanically and electronically stability graphene molecular junctions from 20K to 300K*, to be submitted.
9. **M. El abbassi**, M. Perrin, G. Borin-Barin, J. Overbeck, O. Braun, P Ruffieux, R. Fasel, and M. Calame, *Implementation of atomically aligned 5-Armchair graphene nanoribbons into electronic devices*, to be submitted.

Oral contributions

1. **May 2015:** *Graphene nanogaps for molecular electronics*, 3rd Molesco Workshop and school on quantum transport Simulation, Oviedo, Spain.
2. **January 2016:** *Graphene based molecular junctions* Molesco MidTerm Review and Workshop, Delft, Netherlands.
3. **April 2016:** *Graphene Nanogaps* IBM Zurich, Switzerland.
4. **September 2016:** *Contacting nano-objects with graphene nanogaps at room temperature* Joint Molesco-Iswitch meeting, Freiburg, Germany.
5. **January 2017:** *Detailed study of EB process to produce graphene nanogaps* Molesco Meeting, Granada, Spain.
6. **September 2017:** *Electrical Breakdown of monolayer graphene: Substrate and Environment effects* ECME 2017, Dresden, Germany, September 2017.
7. **September 2017:** *Detailed characterization of graphene based molecular devices* Molesco meeting, Muggendorf, Germany, September 2017.

Poster contributions

1. **February 2015:** *CVD graphene as a versatile material for molecular electronics and sensing*, Molesco meeting, Engelberg, Switzerland.
2. **Engelberg, Switzerland.** : *Controlling the fabrication of graphene nanoelectrodes*, Molesco meeting, Regensburg, Germany.
3. **June 2016:** *Electrical Quantum Metrology to Thermoelectricity: Vast possibilities with CVD graphene*, Swiss Nanoconvention, Basel, Switzerland.
4. **August 2016:** *Graphene molecular junctions*, ELecmol, Paris, France.

Others

- Antelope at university Fellow 2015.